FORMATION, DYNAMICS, AND DECAY OF QUANTIZED VORTICES IN BOSE-EINSTEIN CONDENSATES: ELEMENTS OF QUANTUM TURBULENCE

by

Tyler William Neely

A Dissertation Submitted to the Faculty of the

COLLEGE OF OPTICAL SCIENCES

In Partial Fulfillment of the Requirements
For the Degree of

DOCTOR OF PHILOSOPHY

In the Graduate College

THE UNIVERSITY OF ARIZONA

2010

THE UNIVERSITY OF ARIZONA
GRADUATE COLLEGE

As members of the Dissertation Committee, we certify that we have read the dissertation prepared by Tyler William Neely
entitled Formation, Dynamics, and Decay of Quantized Vortices in Bose-Einstein Condensates: Elements of Quantum Turbulence
and recommend that it be accepted as fulfilling the dissertation requirement for the Degree of Doctor of Philosophy.

Brian P. Anderson — Date: 27 April 2010

Poul Jessen — Date: 27 April 2010

Ewan Wright — Date: 27 April 2010

Final approval and acceptance of this dissertation is contingent upon the candidate's submission of the final copies of the dissertation to the Graduate College.
I hereby certify that I have read this dissertation prepared under my direction and recommend that it be accepted as fulfilling the dissertation requirement.

Dissertation Director: Brian P. Anderson — Date: 27 April 2010

STATEMENT BY AUTHOR

This dissertation has been submitted in partial fulfillment of requirements for an advanced degree at the University of Arizona and is deposited in the University Library to be made available to borrowers under rules of the Library.

SIGNED: Tyler William Neely

ACKNOWLEDGEMENTS

Thanks is first due to my advisor, Brian Anderson, without whom the experiments described within this dissertation, nor the completion of the written document itself, would have been possible. His near constant availability for questions and patience for basic physics discussions have been invaluable in my career as a graduate student. His support and understanding through the many hurdles of graduate school have been greatly appreciated, and his dedication to teaching and to the success of each one of his students, past and present, is likewise admirable.

I could not have completed the experiments in this dissertation without the efforts of the graduate students who came before me, with primary credit going to David Scherer and Chad Weiler. Their perseverance through years of challenges related to the building up of the lab have resulted in a truly remarkable science machine, with amazing reliability. I especially enjoyed working with Chad Weiler, who made months of taking data in the lab not only scientifically interesting, but also entertaining. It has been a pleasure to work with Carlo Samson, with whom the experimental future of the lab rests in qualified hands. As the group has grown to include Kali Wilson and Zach Newman, there is a deepening synthesis of theoretical and experimental knowledge that will be of great benefit to the group; I'm excited to hear about the interesting research it will produce.

Thanks is due to our theory collaborators, Matthew Davis, Ashton Bradley, and Kody Law, whose expertise has contributed to our insights into the experiments, and who have also contributed to and strengthened our joint publications. I would also like to thank several professors within the College of Optical Sciences: Poul Jessen, whose thorough approach to quantum mechanics was appreciated by me for its mathematical rigorousness; Ewan Wright, whose ways of thinking about physics problems often provided me a way out of my own mental box; and Jason Jones, whose help with the next step beyond graduate school has been appreciated.

I would like to thank my parents and siblings, who have always supported me throughout my academic and artistic pursuits. Credit is especially due to my father, the original Dr. Neely, whose dedication to his "hobby" of astronomy got me interested in science and physics in the first place.

Thanks to Samantha Lemons for her love and understanding throughout the difficult process of finishing graduate school.

Finally, thanks is also due to the many musicians I've been able to interact with here in Tucson, especially to Eric Aspnes, Stefano Young, Josh Gordon, and Darryl Roles, who have helped to provide me an artistic outlet and crucial balance to my scientific pursuits.

DEDICATION

To my Dad: for bringing me along to all those telescopes and sparking my interest in science.

TABLE OF CONTENTS

TABLE OF CONTENTS – *Continued*

TABLE OF CONTENTS – *Continued*

LIST OF FIGURES

LIST OF FIGURES – *Continued*

LIST OF TABLES

ABSTRACT

Turbulence in classical fluids has been the subject of scientific study for centuries, yet there is still no complete general theory of classical turbulence connecting microscopic physics to macroscopic fluid flows, and this remains one of the open problems in physics. In contrast, the phenomenon of quantum turbulence in superfluids has well-defined theoretical descriptions, based on first principles and microscopic physics, and represents a realm of physics that can connect the classical and quantum worlds. Studies of quantum turbulence may thus be viewed as a path for progress on the long-standing problem of turbulence.

A dilute-gas Bose-Einstein condensate (BEC) is, in most cases, a superfluid that supports quantized vortices, the primary structural elements of quantum turbulence. BECs are particularly convenient systems for the study of vortices, as standard techniques allow the microscopic structure and dynamics of the vortices to be investigated. Vortices in BECs can be created and manipulated using a variety of techniques, hence BECs are potentially powerful systems for the microscopic study of quantum turbulence.

This dissertation focuses on quantized vortices in BECs, specifically experimental and numerical studies of their formation, dynamics, and decay, in an effort to understand the microscopic nature of vortices as elements of quantum turbulence. Four main experiments were performed, and are described in the main chapters of this dissertation, after introductions to vortices, experimental methods, and turbulence are presented. These experiments were aimed at understanding various aspects of how vortices are created and behave in a superfluid system. They involved vortex dipole nucleation in the breakdown of superfluidity, persistent current generation from a turbulent state in the presence of energy dissipation, decay of angular momentum of a BEC due to trapping potential impurities, and exploration

of the spontaneous formation of vortices during the BEC phase transition. These experiments represent progress towards enhanced understanding of the formation, dynamics, and decay of vortices in BECs and thus may be foundational to more general studies of quantum turbulence in superfluids.

CHAPTER 1

INTRODUCTION

The first experimental realizations of dilute-gas Bose-Einstein condensation in 1995 [1, 2, 3] represented the completion of a goal nearly 70 years old. A broad and active field of research studying and working with Bose-Einstein condensates (BECs) has now opened up, particularly distinguished by the exquisite control over experimental parameters that may be used to microscopically manipulate these macroscopic quantum systems. Fundamental investigations of quantum phase transitions, tests of superfluidity, studies of coherence, quantum atom-optics, and nonlinear atom-optics, for example, have come out of BEC research; some overviews of this rich field may be found in [4, 5, 6, 7]. Among the phenomenology associated with BECs, aspects of superfluidity are of primary interest in this dissertation. In particular, a property of superfluidity that may be explored in BECs is the expected ability of a BEC to support quantum (superfluid) turbulence, characterized by disordered superfluid flow, a disordered arrangement of vortices, and signature bulk statistical properties (see Section 3.3). Accounts of work towards understanding key elements of superfluid turbulence at a microscopic level, specifically focusing on the generation, dynamics and decay of quantized vortices, make up the bulk of the material described in this dissertation. Although bulk properties of quantum turbulence were not investigated quantitatively in the four main experiments that are here described, these studies may prove foundational for additional work pursuing and understanding experimental realizations of quantum turbulence in BECs.

1.1 Outline of this dissertation

In order to provide a guide to the contents of this dissertation, a brief discussion of the primary content of each of the subsequent chapters is first given. After this, an

introduction to vortices in BECs is given, and the remainder of this introductory chapter contains a summary of previous BEC vortex experiments, in order to provide a brief overview of relevant vortex work that has led to the ability to study quantum turbulence in BECs.

Chapter 2 outlines some basic aspects of the experimental apparatus used to create, manipulate, and study BECs and vortices in our lab. Included are several modifications to the previous experimental apparatus, which was described in the two previous PhD dissertations from the group [8, 9]. These modifications were instrumental in conducting the experiments described in this dissertation, including the addition of optical fields used to modify the trapping potential that holds the BEC, and techniques used to transfer atoms into a trap consisting of a spherical quadrupole magnetic field and an optical trapping beam. While only used for one experiment, this combined spherical quadrupole magnetic field and optical beam trap may prove very useful in future work.

Chapter 3 outlines some of the basic concepts in classical and quantum turbulence, and gives reasons why BECs represent a particularly convenient system for the study of quantum turbulence at a microscopic level. Although the experiments described within this dissertation were not direct investigations of quantum turbulence[1], prototype experiments that exhibit some characteristic properties of quantum turbulence are described at the end of Chapter 3; these prototype experiments served as motivation for some of the other studies described in the following chapters of this dissertation.

Chapter 4 describes an experiment in which a building block of quantum turbulence, a vortex dipole (a pair of oppositely charged vortex cores), was controllably generated and the vortex dipole formation, dynamics, and decay were studied. In an extension of these techniques, Chapter 5 describes an experiment in which vortex dipole generation was utilized to generate quantum turbulence. Along with ther-

[1]It can be appropriately argued that the dynamics of the BEC phase transition, described in Chapter 7, involve superfluid turbulence. This relationship will be more fully described in Chapter 7.

mal damping, the turbulent initial state was used to establish persistent superflows (persistent currents) in a toroidal trap geometry.

Chapter 6 describes investigations of the loss of angular momentum from a rotating BEC due to the addition of asymmetry to the trapping potential. Asymmetries in the trapping potential, as an imposed experimental parameter or natural feature of the system, may generally result in systematic limitations of vortex lifetimes and vortex dynamics, and are consequently important in understanding the behavior of turbulence in the system.

Chapter 7 explores the spontaneous formation of vortices resulting from a non-equilibrium quench through the BEC phase transition. The dynamics of the phase transition can be described in terms of the evolution of an initially turbulent state into quasi-equilibrium through thermal damping; the non-equilibrium state is characterized by the presence of quantized vortices, and in this experiment, vortices can be used as signatures of phase transition dynamics.

Finally, concluding remarks are given in Chapter 8.

1.2 Vortices in BEC

A system that exhibits superfluidity possesses properties markedly different than those found in classical fluid systems. Primary among these is a complete lack of viscosity for the superfluid portion of the system; fluid flows are not dissipated as there is no resistance to flow for low-enough fluid velocities, and thus a flow may "persist" indefinitely. A superfluid may even be succinctly characterized as a system that exhibits persistence of flow, and that supports quantized vortices. For relevant reviews of superfluidity in helium, see Refs. [10, 11, 12, 13]. Macroscopic phase coherence is at the origin of quantized vorticity, and it is most easily understood by utilizing a macroscopic wavefunction description for the quantum fluid:

$$\psi(\mathbf{r},t) = \sqrt{n(\mathbf{r},t)}e^{i\phi(\mathbf{r},t)}, \tag{1.1}$$

where $n(\mathbf{r},t)$ the density of the superfluid, and $\phi(\mathbf{r},t)$ is the phase profile[2] [4]. While this description breaks down for strongly interacting systems and some BEC experiments, it is appropriate for the experiments described here. Consequent of this description and the probability current of a quantum system [14], the superfluid flow velocity $\mathbf{v}(\mathbf{r})$, at the position $\mathbf{r}$ within the fluid, may be written as:

$$\mathbf{v}(\mathbf{r}) = \frac{\hbar}{m}\nabla\phi(\mathbf{r}), \tag{1.2}$$

where m is the mass of an atom in the fluid. In other words, superfluid flow velocity is intimately related to the phase profile of the quantum system.

Dynamics of dilute superfluid systems, and Bose-Einstein condensates in particular, are often well described by the nonlinear Schrödinger equation known as the time-dependent Gross-Pitaevskii equation (GPE) [4]:

$$i\hbar\frac{\partial\psi(\mathbf{r},t)}{\partial t} = -\frac{\hbar^2}{2m}\nabla^2\psi(\mathbf{r},t) + V(\mathbf{r},t)\psi(\mathbf{r},t) + g|\psi(\mathbf{r},t)|^2\psi(\mathbf{r},t). \tag{1.3}$$

In this equation, $g = 4\pi\hbar^2 a/m$ characterizes the strength of non-linear dynamics dependent on the s-wave scattering length a, and $V(\mathbf{r},t)$ is the external potential used to trap and manipulate the BEC. The nonlinear term originates in particle-particle interactions and is a good approximation for dilute systems or systems with weak interactions between particles. This equation is strictly appropriate in the zero-temperature limit.

Since the wavefunction must be single-valued for self-consistency, the phase may only change by multiples of 2π about any closed loop, referred to as the Onsager-Feynman condition [15]. Circulation, or fluid flow about a given point in the superfluid system, is thus quantized, and a phase-winding of 2π defines a *singly-quantized vortex*. At the center of the phase loop, the phase is undefined. However, when examining the fluid flow about this center point, $\nabla\phi(\mathbf{r})$ and thus $\mathbf{v}(\mathbf{r})$ diverge as

[2]This aspect of phase coherence and the appropriateness of a macroscopic wavefunction turns out to be most relevant for a dilute gas BEC, although less so for a bulk superfluid with strong interatomic interactions. Theoretical details on the relevance and attainment of a macroscopic wavefunction will not be discussed here, see Refs. [4, 5, 7] for further discussion.

the center point is approached. Since the system contains finite energy, fluid flow is not supported at the discontinuity. Fluid is thus absent at the center of the phase loop, and in fact the fluid density $n(\mathbf{r}, t)$ decreases continuously from its bulk value to zero at the discontinuity. This density zero in the fluid defines a line through the thin core of the quantized vortex, which has a radius on the order of the healing length for the fluid, given by:

$$\xi = [8\pi a n(\mathbf{r}, t)]^{-1/2}. \tag{1.4}$$

The healing length is the characteristic shortest distance over which the density can drop from its bulk value to zero, limited by the energy of the system.

The quantization of circulation present in a superfluid is markedly different from a classical fluid, where any value of circulation can be manifest. Additionally, the vortex will not spontaneously decay, as the quantum phase profile requirements and the inviscid nature of the superfluid prevent its sudden disappearance. Instead, vortices must be removed (or added) to the system by other means, described later in this dissertation.

Example images of vortices in a BEC are shown in Fig. 1.1. Although the circulation about a vortex core is quantized, the net angular momentum of the fluid system can take on a range of values, depending on the location of the vortex within the BEC. Gradually moving a vortex in from the edge of the BEC to the center, for example, the angular momentum per particle smoothly increases from 0 to $\hbar$ [16]. With multiple vortices of the same direction of circulation in the BEC, the stable equilibrium configuration is a hexagonal lattice. With N vortices arranged in a lattice, the angular momentum per particle is equal to $N\hbar/2$ [11, 17, 18].

1.3 Experimental vortex studies in BEC: a bibliographic reference

The study of quantized vortices represents an active and extensive section of BEC research since vortices were first created and observed in 1999 [19]. The observation of quantized vortices was essential in providing evidence for the superfluid nature of

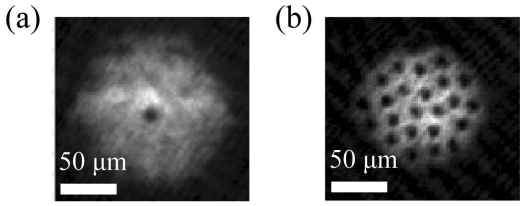

Figure 1.1: (a) Image showing the presence of a vortex core approximately at the center of a BEC, represented by the dark spot in the middle of the image, for a BEC formed in a flattened trap (see Section 2.6). Lighter shades in the image indicate higher column densities integrated along the line of sight (experimental techniques are discussed in Chapter 2). Additional fringes and density variations are artifacts from the imaging process. With a single vortex aligned at the center of a BEC, each atom in the BEC carries $\hbar$ of angular momentum. (b) Image showing the presence of multiple vortices in a BEC formed in a TOP trap (see Section 2.3). With multiple vortices in the BEC, the stable configuration is a hexagonal lattice. This image contains $\sim$ 24 vortices, in an arrangement approaching a lattice, implying that there is $\sim 12\hbar$ of angular momentum per atom about the line-of-sight axis.

dilute atomic gas BECs. As a fundamental collective excitation of the BEC system, quantized vortices are connected to a variety of physical processes in BECs [16]. It is impractical to review here all the work that has been done with vortices in BECs since 1999. Further, good reviews already exist; see for example Refs. [6, 16, 20]. However, as an aid to researchers in the field and in an effort to place the research described in this dissertation within the body of vortex work in BECs, what follows is an attempt to compile a complete list of *all* published experiments studying vortex creation, dynamics, decay, and observation in degenerate gases, both with Bose-Einstein condensates and degenerate Fermi gases. The titles for the papers are given, and reading these gives a quick sense of the areas of emphasis and main achievements in BEC vortex research over the past 11 years. All included citations have been found by searching through ISI records and many lists of references in published papers. It is nevertheless likely that there are some papers that have been inadvertently left out. Only articles that contain experimental results published prior to early 2010 are listed (chronologically), and papers that are strictly theoretical or numerical are not included. Review papers and eprints are also not included.

1.3.1 Vortex experiments, arranged chronologically

1999

- [19] M. R. Matthews, B. P. Anderson, P. C. Haljan, D. S. Hall, C. E. Wieman, and E. A. Cornell. Vortices in a Bose-Einstein condensate. *Phys. Rev. Lett.*, 83(13):2498, Sep 1999

2000

- [21] K. W. Madison, F. Chevy, W. Wohlleben, and J. Dalibard. Vortex formation in a stirred Bose-Einstein condensate. *Phys. Rev. Lett.*, 84(5):806, Jan 2000

- [22] K. W. Madison, F. Chevy, W. Wohlleben, and J. Dalibard. Vortices in a stirred Bose-Einstein condensate. *J. Mod. Opt.*, 47(14-15):2715, Nov 2000

- [23] F. Chevy, K. W. Madison, and J. Dalibard. Measurement of the angular momentum of a rotating Bose-Einstein condensate. *Phys. Rev. Lett.*, 85(11):2223, Sep 2000

- [24] B. P. Anderson, P. C. Haljan, C. E. Wieman, and E. A. Cornell. Vortex precession in Bose-Einstein condensates: Observations with filled and empty cores. *Phys. Rev. Lett.*, 85(14):2857, Oct 2000

2001

- [25] J. R. Abo-Shaeer, C. Raman, J. M. Vogels, and W. Ketterle. Observation of vortex lattices in Bose-Einstein condensates. *Science*, 292(5516):476, Apr 2001

- [26] B. P. Anderson, P. C. Haljan, C. A. Regal, D. L. Feder, L. A. Collins, C. W. Clark, and E. A. Cornell. Watching dark solitons decay into vortex rings in a Bose-Einstein condensate. *Phys. Rev. Lett.*, 86(14):2926, Apr 2001

- [27] P. C. Haljan, B. P. Anderson, I. Coddington, and E. A. Cornell. Use of surface-wave spectroscopy to characterize tilt modes of a vortex in a Bose-Einstein condensate. *Phys. Rev. Lett.*, 86(14):2922, Apr 2001

- [28] K. W. Madison, F. Chevy, V. Bretin, and J. Dalibard. Stationary states of a rotating Bose-Einstein condensate: Routes to vortex nucleation. *Phys. Rev. Lett.*, 86(20):4443, May 2001

- [29] Z. Dutton, M. Budde, C. Slowe, and L. V. Hau. Observation of quantum shock waves created with ultra-compressed slow light pulses in a Bose-Einstein condensate. *Science*, 293(5530):663, Jul 2001

- [30] F. Chevy, K. W. Madison, V. Bretin, and J. Dalibard. Interferometric detection of a single vortex in a dilute Bose-Einstein condensate. *Phys. Rev. A*, 64(3):031601, Aug 2001

- [31] S. Inouye, S. Gupta, T. Rosenband, A. P. Chikkatur, A. Görlitz, T. L. Gustavson, A. E. Leanhardt, D. E. Pritchard, and W. Ketterle. Observation of vortex phase singularities in Bose-Einstein condensates. *Phys. Rev. Lett.*, 87(8):080402, Aug 2001

- [32] P. C. Haljan, I. Coddington, P. Engels, and E. A. Cornell. Driving Bose-Einstein-condensate vorticity with a rotating normal cloud. *Phys. Rev. Lett.*, 87(21):210403, Nov 2001

- [33] C. Raman, J. R. Abo-Shaeer, J. M. Vogels, K. Xu, and W. Ketterle. Vortex nucleation in a stirred Bose-Einstein condensate. *Phys. Rev. Lett.*, 87(21):210402, Nov 2001

- [34] E. Hodby, G. Hechenblaikner, S. A. Hopkins, O. M. Maragò, and C. J. Foot. Vortex nucleation in Bose-Einstein condensates in an oblate, purely magnetic potential. *Phys. Rev. Lett.*, 88(1):010405, Dec 2001

2002

- [35] J. R. Abo-Shaeer, C. Raman, and W. Ketterle. Formation and decay of vortex lattices in Bose-Einstein condensates at finite temperatures. *Phys. Rev. Lett.*, 88(7):070409, Feb 2002

- [36] P. Rosenbusch, D. S. Petrov, S. Sinha, F. Chevy, V. Bretin, Y. Castin, G. Shlyapnikov, and J. Dalibard. Critical rotation of a harmonically trapped Bose gas. *Phys. Rev. Lett.*, 88(25):250403, Jun 2002

- [37] P. Engels, I. Coddington, P. C. Haljan, and E. A. Cornell. Nonequilibrium effects of anisotropic compression applied to vortex lattices in Bose-Einstein condensates. *Phys. Rev. Lett.*, 89(10):100403, Aug 2002

- [38] A. E. Leanhardt, A. Görlitz, A. P. Chikkatur, D. Kielpinski, Y. Shin, D. E. Pritchard, and W. Ketterle. Imprinting vortices in a Bose-Einstein condensate using topological phases. *Phys. Rev. Lett.*, 89(19):190403, Oct 2002

- [39] P. Rosenbusch, V. Bretin, and J. Dalibard. Dynamics of a single vortex line in a Bose-Einstein condensate. *Phys. Rev. Lett.*, 89(20):200403, Oct 2002

2003

- [40] V. Bretin, P. Rosenbusch, F. Chevy, G. V. Shlyapnikov, and J. Dalibard. Quadrupole oscillation of a single-vortex Bose-Einstein condensate: Evidence for Kelvin modes. *Phys. Rev. Lett.*, 90(10):100403, Mar 2003

- [41] V. Bretin, P. Rosenbusch, and J. Dalibard. Dynamics of a single vortex line in a Bose-Einstein condensate. *Journal of Optics B: Quantum and Semiclassical Optics*, 5(2):S23, Apr 2003

- [42] A. E. Leanhardt, Y. Shin, D. Kielpinski, D. E. Pritchard, and W. Ketterle. Coreless vortex formation in a spinor Bose-Einstein condensate. *Phys. Rev. Lett.*, 90(14):140403, Apr 2003

- [43] P. Engels, I. Coddington, P. C. Haljan, V. Schweikhard, and E. A. Cornell. Observation of long-lived vortex aggregates in rapidly rotating Bose-Einstein condensates. *Phys. Rev. Lett.*, 90(17):170405, May 2003

- [44] P. Engels, I. Coddington, P. C. Haljan, and E. A. Cornell. Using anisotropic compression to melt a vortex lattice in a Bose-Einstein condensate. *Physica B: Cond. Mat.*, 329(1):7, May 2003

- [45] E. Hodby, S. A. Hopkins, G. Hechenblaikner, N. L. Smith, and C. J. Foot. Experimental observation of a superfluid gyroscope in a dilute Bose-Einstein condensate. *Phys. Rev. Lett.*, 91(9):090403, Aug 2003

- [46] I. Coddington, P. Engels, V. Schweikhard, and E. A. Cornell. Observation of Tkachenko oscillations in rapidly rotating Bose-Einstein condensates. *Phys. Rev. Lett.*, 91(10):100402, Sep 2003

2004

- [47] P. Engels, I. Coddington, V. Schweikhard, and E. A. Cornell. Vortex lattice dynamics in a dilute gas BEC. *J. Low Temp. Phys*, 134:683, Jan 2004

- [48] V. Schweikhard, I. Coddington, P. Engels, V. P. Mogendorff, and E. A. Cornell. Rapidly rotating Bose-Einstein condensates in and near the lowest Landau level. *Phys. Rev. Lett.*, 92(4):040404, Jan 2004

- [49] V. Bretin, S. Stock, Y. Seurin, and J. Dalibard. Fast rotation of a Bose-Einstein condensate. *Phys. Rev. Lett.*, 92(5):050403, Feb 2004

- [50] S. Stock, V. Bretin, F. Chevy, and J. Dalibard. Shape oscillation of a rotating Bose-Einstein condensate. *Europhys. Lett.*, 65(5):594, Mar 2004

- [51] P. Rosenbusch, V. Bretin, F. Chevy, G. V. Shlyapnikov, and J. Dalibard. Evidence for Kelvin modes in a single vortex Bose-Einstein condensate. *Laser Phys.*, 14(4):545, 2004

- [52] N. L. Smith, W. H. Heathcote, J. M. Krueger, and C. J. Foot. Experimental observation of the tilting mode of an array of vortices in a dilute Bose-Einstein condensate. *Phys. Rev. Lett.*, 93(8):080406, Aug 2004

- [53] Y. Shin, M. Saba, M. Vengalattore, T. A. Pasquini, C. Sanner, A. E. Leanhardt, M. Prentiss, D. E. Pritchard, and W. Ketterle. Dynamical instability of a doubly quantized vortex in a Bose-Einstein condensate. *Phys. Rev. Lett.*, 93(16):160406, Oct 2004

- [54] V. Schweikhard, I. Coddington, P. Engels, S. Tung, and E. A. Cornell. Vortex-lattice dynamics in rotating spinor Bose-Einstein condensates. *Phys. Rev. Lett.*, 93(21):210403, Nov 2004

- [55] I. Coddington, P. C. Haljan, P. Engels, V. Schweikhard, S. Tung, and E. A. Cornell. Experimental studies of equilibrium vortex properties in a Bose-condensed gas. *Phys. Rev. A*, 70(6):063607, Dec 2004

2005

- [56] N. S. Ginsberg, J. Brand, and L. V. Hau. Observation of hybrid soliton vortex-ring structures in Bose-Einstein condensates. *Phys. Rev. Lett.*, 94(4):040403, Jan 2005

- [57] S. Stock, B. Battelier, V. Bretin, Z. Hadzibabic, and J. Dalibard. Bose-Einstein condensates in fast rotation. *Laser Phys. Lett.*, 2(6):275, Jan 2005

- [58] T. P. Simula, P. Engels, I. Coddington, V. Schweikhard, E. A. Cornell, and R. J. Ballagh. Observations on sound propagation in rapidly rotating Bose-Einstein condensates. *Phys. Rev. Lett.*, 94(8):080404, Mar 2005

- [59] M. W. Zwierlein, J. R. Abo-Shaeer, A. Schirotzek, C. H. Schunck, and W. Ketterle. Vortices and superfluidity in a strongly interacting Fermi gas. *Nature*, 435(7045):1047, Jun 2005

- [60] S . Stock, Z. Hadzibabic, B. Battelier, M. Cheneau, and J. Dalibard. Observation of phase defects in quasi-two-dimensional Bose-Einstein condensates. *Phys. Rev. Lett.*, 95(19):190403, Nov 2005

2006

- [61] M. W. Zwierlein, A. Schirotzek, C. H. Schunck, and W. Ketterle. Fermionic superfluidity with imbalanced spin populations. *Science*, 311(5760):492, Jan 2006

- [62] M. Kumakura, T. Hirotani, M. Okano, T. Yabuzaki, and Y. Takahashi. Topological creation of a multiply charged quantized vortex in the Rb Bose-Einstein condensate. *Laser Phys.*, 16(2):371, Feb 2006

- [63] S. R. Muniz, D. S. Naik, and C. Raman. Bragg spectroscopy of vortex lattices in Bose-Einstein condensates. *Phys. Rev. A*, 73(4):041605, Apr 2006

- [64] Z. Hadzibabic, P. Kruger, M. Cheneau, B. Battelier, and J. Dalibard. Berezinskii-Kosterlitz-Thouless crossover in a trapped atomic gas. *Nature*, 441(7097):1118, Jun 2006

- [65] M. Kumakura, T. Hirotani, M. Okano, Y. Takahashi, and T. Yabuzaki. Topological formation of a multiply charged vortex in the Rb Bose-Einstein condensate: Effectiveness of the gravity compensation. *Phys. Rev. A*, 73(6):063605, Jun 2006

- [66] L. E. Sadler, J. M. Higbie, S. R. Leslie, M. Vengalattore, and D. M. Stamper-Kurn. Spontaneous symmetry breaking in a quenched ferromagnetic spinor Bose-Einstein condensate. *Nature*, 443(7109):312, Sep 2006

- [67] M. F. Andersen, C. Ryu, P. Cladé, V. Natarajan, A. Vaziri, K. Helmerson, and W. D. Phillips. Quantized rotation of atoms from photons with orbital angular momentum. *Phys. Rev. Lett.*, 97(17):170406, Oct 2006

- [68] S. Tung, V. Schweikhard, and E. A. Cornell. Observation of vortex pinning in Bose-Einstein condensates. *Phys. Rev. Lett.*, 97(24):240402, Dec 2006

2007

- [69] C. H. Schunck, M. W. Zwierlein, A. Schirotzek, and W. Ketterle. Superfluid expansion of a rotating Fermi gas. *Phys. Rev. Lett.*, 98(5):050404, Feb 2007

- [70] S. R. Muniz, D. S. Naik, M. Bhattacharya, and C. Raman. Dynamics of rotating Bose-Einstein condensates probed by Bragg scattering. *Mathematics and Computers in Simulation*, 74(4-5):397, Mar 2007

- [71] D. R. Scherer, C. N. Weiler, T. W. Neely, and B. P. Anderson. Vortex formation by merging of multiple trapped Bose-Einstein condensates. *Phys. Rev. Lett.*, 98(11):110402, Mar 2007

- [72] K. Helmerson, M. F. Andersen, C. Ryu, P. Cladé, V. Natarajan, A. Vaziri, and W.D. Phillips. Generating persistent currents states of atoms using orbital angular momentum of photons. *Nuclear Physics A*, 790(1-4):705c, Jun 2007

- [73] V. Schweikhard, S. Tung, and E. A. Cornell. Vortex proliferation in the Berezinskii-Kosterlitz-Thouless regime on a two-dimensional lattice of Bose-Einstein condensates. *Phys. Rev. Lett.*, 99(3):030401, Jul 2007

- [74] T. Isoshima, M. Okano, H. Yasuda, K. Kasa, J. A. M. Huhtamäki, M. Kumakura, and Y. Takahashi. Spontaneous splitting of a quadruply charged vortex. *Phys. Rev. Lett.*, 99(20):200403, Nov 2007

- [75] C. Ryu, M. F. Andersen, P. Cladé, V. Natarajan, K. Helmerson, and W. D. Phillips. Observation of persistent flow of a Bose-Einstein condensate in a toroidal trap. *Phys. Rev. Lett.*, 99(26):260401, Dec 2007

2008

- [76] Z. Hadzibabic, P. Kruger, M. Cheneau, S. P. Rath, and J. Dalibard. The trapped two-dimensional Bose gas: from Bose-Einstein condensation to Berezinskii-Kosterlitz-Thouless physics. *New Journal of Physics*, 10(4):045006, Apr 2008

- [77] K. C. Wright, L. S. Leslie, and N. P. Bigelow. Optical control of the internal and external angular momentum of a Bose-Einstein condensate. *Phys. Rev. A*, 77(4):041601, Apr 2008

- [78] D. McKay, M. White, M. Pasienski, and B. DeMarco. Phase-slip-induced dissipation in an atomic Bose-Hubbard system. *Nature*, 453(7191):76, May 2008

- [79] C. N. Weiler, T. W. Neely, D. R. Scherer, A. S. Bradley, M. J. Davis, and B. P. Anderson. Spontaneous vortices in the formation of Bose-Einstein condensates. *Nature*, 455(7215):948, Oct 2008

2009

- [80] K. C. Wright, L. S. Leslie, A. Hansen, and N. P. Bigelow. Sculpting the vortex state of a spinor BEC. *Phys. Rev. Lett.*, 102(3):030405, Jan 2009

- [81] E. A. L. Henn, J. A. Seman, E. R. F. Ramos, M. Caracanhas, P. Castilho, E. P. Olímpio, G. Roati, D. V. Magalhães, K. M. F. Magalhães, and V. S. Bagnato. Observation of vortex formation in an oscillating trapped Bose-Einstein condensate. *Phys. Rev. A*, 79(4):043618, Apr 2009

- [82] E. A. L. Henn, J. A. Seman, G. Roati, K. M. F. Magalhães, and V. S. Bagnato. Emergence of turbulence in an oscillating Bose-Einstein condensate. *Phys. Rev. Lett.*, 103(4):045301, Jul 2009

- [83] Y.-J. Lin, R. L. Compton, K. Jimenez-Garcia, J. V. Porto, and I. B. Spielman. Synthetic magnetic fields for ultracold neutral atoms. *Nature*, 462(7273):628, Dec 2009

- [84] K. Helmerson, M. F. Andersen, P. Cladé, V. Natarajan, W. D. Phillips, A. Ramanathan, C. Ryu, and A. Vaziri. Vortices and persistent currents: Rotating a Bose-Einstein condensate using photons with orbital angular momentum. *Topologica*, 2(1):002, 2009

2010

- [85] E. Henn, J. Seman, G. Roati, K. Magalhães, and V. Bagnato. Generation of vortices and observation of quantum turbulence in an oscillating Bose-Einstein condensate. *J. Low Temp. Phys.*, 158(3):435, Feb 2010

- [86] R. A. Williams, S. Al-Assam, and C. J. Foot. Observation of vortex nucleation in a rotating two-dimensional lattice of Bose-Einstein condensates. *Phys. Rev. Lett.*, 104(5):050404, Feb 2010

- [87] T. W. Neely, E. C. Samson, A. S. Bradley, M. J. Davis, and B. P. Anderson. Observation of vortex dipoles in an oblate Bose-Einstein condensate. *Phys. Rev. Lett.*, 104(16):160401, Apr 2010

1.3.2 Brief summary of BEC vortex experiments

Although a review of these experiments will not be given here, we can briefly summarize the areas of emphasis of these experiments. First, the bulk of these experiments are related to creating and studying rotating condensates: experiments where the BEC is rotating in a well-defined direction about a well-defined axis. This case encompasses rotation techniques base on quantum engineering [19, 24, 27, 38, 42, 53, 62, 65, 67, 72, 74, 75, 84], trap deformation and rotation, leading to a rotating BEC [18, 21, 22, 23, 28, 30, 33, 34, 35, 36, 39, 40, 41, 45, 49, 50, 51, 52, 57, 59, 61, 63, 69, 70], thermal cloud rotation followed by condensation [32, 37, 43, 44, 46, 47, 48, 54, 55, 58, 68], and BEC rotation from a rotating superimposed optical lattice [86]. We might also place the experiments of Ref. [83] into this category; although the BEC was not rotating in the lab frame of reference, the vortices created were of uniform and well-defined orientation.

Next, we can identify a small subset of experiments in which vortex arrangements did not define a rotating state, but were nevertheless reproducibly created. This category includes quantum engineering methods with spinor condensates [77, 80] and vortex dipole nucleation [87] (see Chapter 4).

Finally, a third category includes experiments where vortex numbers, orientations, and arrangements were not controlled. This category includes experiments studying physics related to the superfluid Berezinskii-Kosterlitz-Thouless (BKT) transition [60, 64, 73, 76], spontaneous formation of spinor vortices in a quenched ferromagnetic phase transition [66], spontaneous formation of vortices in the BEC phase transition [79], vortex and vortex ring formation via dynamical instabilities [26, 29, 56], vortex formation by interference [71], (see also [73, 86]), vortex formation accompanying phase-slip induced dissipation [78], vortex formation due to moving obstacles within the BEC [31], and vortex formation due to oscillating traps [81, 82, 85].

Of all of these, only a few mention turbulence or quantum turbulence [21, 23, 31, 33, 54, 59, 79, 81, 82, 85]. Furthermore, only two recent papers have been specifically oriented towards studying properties of quantum turbulence [82, 85].

We thus end this chapter by noting that with nearly 70 papers on BEC vortex experiments throughout the last decade, quantum turbulence studies in BECs are just now underway. Due to the difficult nature of such experiments (mentioned in Chapter 3), our approach to the problem encompasses learning about how vortices interact such that turbulent states may be better understood. This subject is discussed at the end of Chapter 3.

CHAPTER 2

EXPERIMENTAL SETUP

2.1 Introduction

This chapter summarizes the apparatus and methods used to create our ^{87}Rb BECs. The apparatus was primarily built by two former graduate students in the lab, David Scherer and Chad Weiler[1]. Extensive descriptions of the experimental apparatus may be found in the PhD thesis of David Scherer [8]; a brief review is presented here, with emphasis on modifications to the apparatus that were utilized in the experiments described in this dissertation.

First, the laser cooling process, transfer of atoms, and evaporative cooling in a magnetic trap are described. Next, techniques used for modifying the trapping potential through the addition of optical fields are discussed. Imaging methods and analysis techniques used to understand the content of the images are described, and the chapter concludes with a discussion of a modification to the magnetic trap that removes any rotating component, resulting in a BEC in a "DC" magnetic spherical quadrupole and optical combined trap.

2.2 Laser cooling and the magneto-optical trap

A two-stage laser cooling process is utilized in the experiment. The apparatus consists of a two-chamber ultra-high vacuum system, with a single magneto-optical trap (MOT). The apparatus achieves a pressure of $\sim 10^{-10}$ Torr in the glass cell used for initial cooling, and pressures as low as $\sim 10^{-12}$ Torr in the "science" cell where the BECs are created. The system is supplied with low-pressure ^{87}Rb gas from a

[1]Former students Elaine Ulrich and M. David Henry also made significant contributions to the construction of the apparatus.

set of SAES ^{87}Rb dispensers located at the back end of the MOT cell. A picture showing the vacuum system with the two glass cells visible is shown in Fig. 2.1(a). The MOT cell is located in the middle-right of the picture, and the science cell can be seen on the left.

The first stage of the experimental sequence involves laser cooling of the ^{87}Rb atoms in the MOT cell. This is accomplished by splitting $\sim$ 500 mW of near-resonant 780-nm laser light into six beams, which are directed at the MOT cell from all sides and gently diverge as they propagate, resulting in $\sim$ 2 in. diameter beams at the MOT cell center. The light is red-detuned from the resonant wavelength for the $|5\ ^2S_{1/2}, F = 2\rangle \rightarrow |5\ ^2P_{3/2}, F' = 3\rangle$ transition in ^{87}Rb by 4.5Γ, where Γ is the natural linewidth of the ^{87}Rb transition, equal to an angular frequency of $2\pi \times 5.9$ MHz. In Doppler cooling, atoms moving towards a beam will see the light Doppler-shifted into resonance and scatter light preferentially for the counter-propagating beam(s), losing kinetic energy. Since beam pairs originate from three orthogonal directions, the average velocity of the atoms is greatly reduced. With the addition of an 8 G/cm axial spherical quadrupole magnetic field and a repump beam tuned near to the $|F = 1\rangle \rightarrow |F' = 2\rangle$ transition, with $\sim$ 30 mW of total beam power split into four beams and directed from two orthogonal directions, a MOT containing $\sim 3 \times 10^9$ atoms at tens of μK is formed. Extensive details of our MOT setup may be found in Ref. [8], and more detailed descriptions of the laser cooling process may be found in several review articles and books [88, 89, 90]. Details of the first MOT may also be found in Ref. [91].

2.3 Magnetic transfer to a time-averaged orbiting potential magnetic trap

Once the MOT has been created, the next sequence in the experiment magnetically transfers the atom cloud to the science cell. The atoms undergo an initial compressed MOT (CMOT) [92] stage lasting 60 ms, increasing the density through spatial compression; this is accomplished through sudden increased detuning of the cooling beams to $\sim -10\Gamma$, a reduction in the repump beam light intensity to $\sim$ 10%

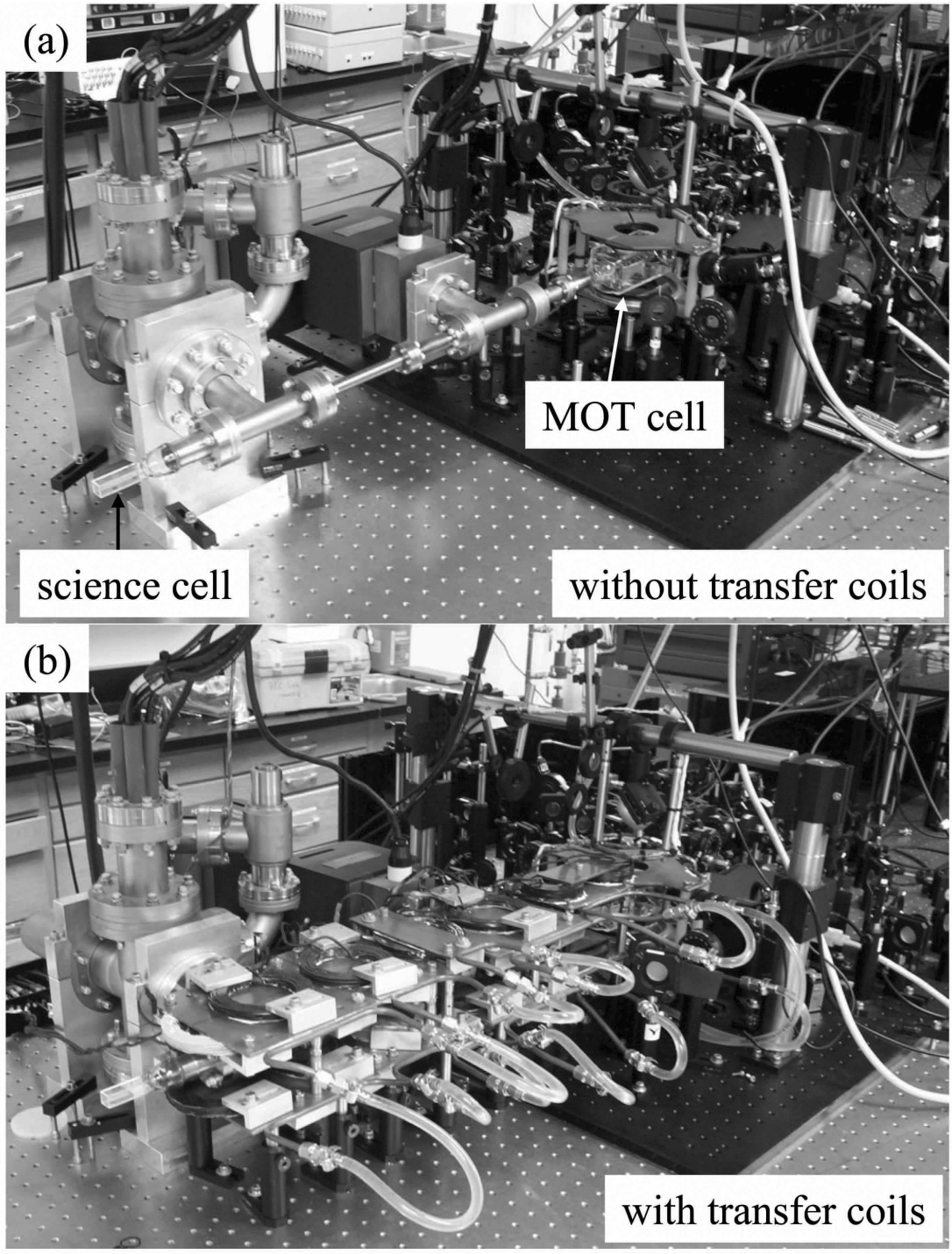

Figure 2.1: (a) Picture of the vacuum system with the magnetic transfer coils removed. The MOT cell is located in the right of the picture, and the science (BEC) cell is located in the left foreground. (b) Vacuum system with the magnetic transfer coils attached. Figure taken from Ref. [8].

of its initial value, and a ramp-off of the quadrupole field to 0 G. As a result of this sequence, the atoms are optically pumped to the $|F = 1\rangle$ ground state. The atoms are then loaded in a spherical quadrupole magnetic field with an axial gradient of 160 G/cm, which traps atoms projected into the $|F = 1, m_F = -1\rangle$ state. An optical molasses cooling stage is not used.

The atom cloud is then transferred to the science cell by ramping on and off the magnetic coil pairs partially visible in Fig. 2.1(b). This sequence adiabatically moves the atoms to the science cell in ~ 4 seconds over a distance of ~ 80 cm. Details of the control electronics, coils geometries, and current waveforms may be found in Ref. [8].

Upon arriving at the science cell, the atoms equilibrate in the $B'_z = 160$ G/cm field for one second before the field is snapped to a value of $B'_z = 266$ G/cm, where B'_z denotes the axial magnetic field gradient, $|dB/dz|$, along the coil axis. An additional bias magnetic field with a strength of $B_0 = 43$ G, is then added; this field points in the horizontal plane and the direction of the field rotates in the plane with an angular frequency of $\omega_{rot} = 2\pi \times 4$ kHz. The gradients due to this field are negligible. The bias-field acts to push the zero point of the quadrupole field in a circular orbit, and since the low kinetic energy of the atoms ensure that they are are only sensitive to the time average of the rotating bias magnetic field, the resulting time-averaged trap is harmonic, with radial and axial trapping frequencies of $(\omega_r, \omega_z) \simeq 2\pi \times (40, 80)$ Hz, respectively. This trap configuration is known as a time-averaged orbiting potential (TOP) trap, and detailed descriptions of TOP traps may be found in the JILA PhD thesis of Jason Ensher [93].

2.4 Evaporative cooling

With the atoms held magnetically in the harmonic potential, the bias-field strength B_0 is ramped to 5 G and simultaneous radio-frequency (RF) induced evaporation further cools the cloud over ~ 60 s. B'_z is simultaneously ramped from 160 G/cm to a value of 52 G/cm, and the center-of-mass position of the cloud in this weak

trap sags due to gravity[2] by 0.56 mm. This "sagged TOP trap" configuration has trapping frequencies considerably weaker than those of the initial TOP trap, with measured trap frequencies of $(\omega_r, \omega_z) \simeq 2\pi \times (7.8, 15.3)$ Hz. A final stage of RF-induced cooling in the weak trap results in a BEC with $N_c \approx 1 \times 10^6$ atoms with a critical temperature of $T_c \sim 42$ nK.

2.5 Imaging techniques and expansion

Images of the atom clouds represent the primary data collected in BEC experiments. Two methods of imaging are used in our experiment: near-resonant absorption imaging and off-resonant phase-contrast imaging.

Near-resonant absorption imaging utilizes laser light tuned closely to the $|F = 2\rangle \rightarrow |F' = 3\rangle$ transition. The light is collimated and directed through the science cell. Since the trapped atoms are in the $|F = 1, m_F = -1\rangle$ ground state, a dark state relative to the imaging light, a ~ 50-μs pulse of additional laser light is used to optically pump the atoms to the $|5\ ^2S_{1/2}, F = 2\rangle$ level. Immediately after this pulse of light, tuned to the $|F = 1\rangle \rightarrow |F' = 2\rangle$ transition, a 20-μs pulse of light tuned near the $|F = 2\rangle \rightarrow |F' = 3\rangle$ transition with an intensity on the order of 1.6 mW/cm^2 is directed at the atoms; light is resonantly scattered out of the collimated imaging beam, and the resulting shadow of the cloud, due to absorption through the integrated optical depth, is imaged onto a near-infrared sensitive CCD camera. The imaging system utilizes two imaging axes, horizontal (along y) and vertical (along the trap's axial direction, z). A diagram of the imaging system is given in Fig. 2.2(a), showing the two imaging axes. The magnification of each system is 5X.

Phase-contrast imaging is accomplished through the use of detuned light, typically 900 MHz red-detuned from the $|F = 1\rangle \rightarrow |F' = 2\rangle$ transition. The light passes

[2]Following the methods of Ref. [93], a sag of 0.73 mm is calculated when using the magnetic field values defined above, different from the measured value of 0.56 mm. We attribute this difference to a calibration error in the magnetic fields. However, the BEC trap frequencies quoted in this dissertation were directly measured, and actual magnetic field values are generally unimportant to the physics examined and discussed here.

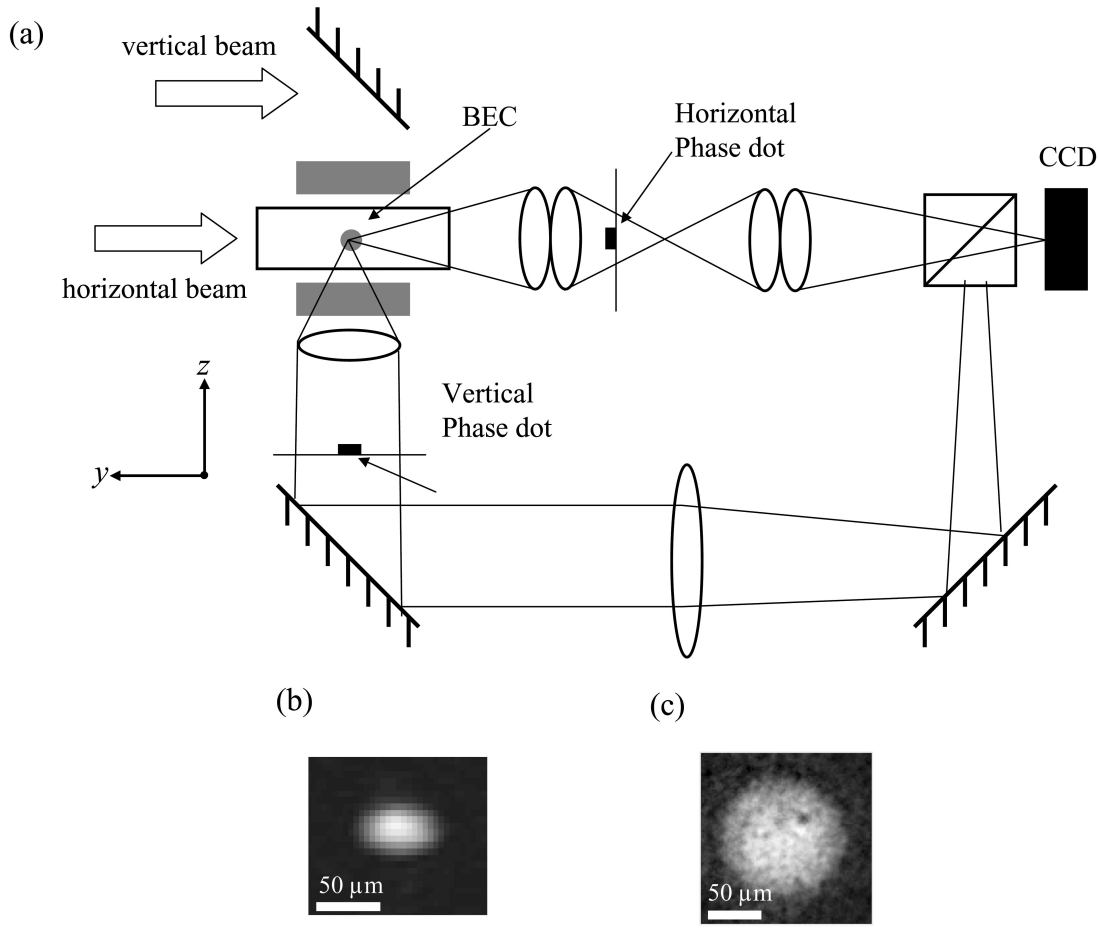

Figure 2.2: (a) Layout of the vertical and horizontal imaging systems, taken from Ref. [8]. Both axes may be used for phase contrast and absorption imaging, although in practice the horizontal system was primarily used for phase-contrast, and the vertical system used for absorption (phase dot removed). (b) Horizontal in-situ phase-contrast image of a BEC. (c) Vertical absorption image in expansion, showing the presence of a vortex in the upper right of the cloud.

through a 100 μm x 100 μm phase dot located at an intermediate focus, shown in Fig. 2.2(a). The phase dot induces a $3\pi/2$ phase shift in the imaging light. Since the light scattered from the BEC is collimated in this intermediate plane, it is negligibly effected by the phase dot, and the resulting constructive interference at the image plane at the CCD produces a bright image of the cloud on a gray background. The phase dot is removed for absorption imaging.

Because the size of a vortex core in our system is ~ 0.3 μm, below the effective 3.4 μm imaging resolution [8], observations of vortices in the atom clouds cannot be done *in-situ*. In order to resolve the vortex cores, expansion of the BEC is implemented using standard methods: the bias-field B_0 is snapped off and an additional magnetic field is added to B'_z. This addition of the spherical quadrupole magnetic field and the extra field produces a total axial gradient of $\sim$ 32 G/cm which levitates the atoms against gravity by canceling the force of gravity with an oppositely directed magnetic force. This configuration also institutes a weak anti-trapping potential in the horizontal direction. The result is near-ballistic expansion of the atom cloud, and $\sim$ 50 ms of expansion of the cloud and vortex cores is sufficient to render vortices resolvable by the imaging system. Example images are seen in Fig. 2.2(b,c), with horizontal *in-situ* phase-contrast and vertical absorption in expansion images shown.

The weak TOP trap represents the basic magnetic trap configuration for our experiment, and was used as a starting point for each of the experiments described in this dissertation. The next few sections describe further modifications to this trapping scheme, allowing for different trapping frequencies and trap frequency ratios (trap geometries), critical temperatures, formation rates, and final atom numbers.

2.6 Combined magnetic and optical potentials

The conservative potential induced by a far-off-resonant intense light field is given by the following relation:

$$U_{beam} = \frac{\hbar\Gamma}{8}\frac{I_{beam}/I_{sat}}{\Delta/\Gamma}, \tag{2.1}$$

where I_{sat} is the saturation intensity of a ^{87}Rb atom, and Δ is the detuning of the optical field from the resonant wavelength of ∼780 nm for ^{87}Rb. Provided the energies of the atoms are low enough, they can be trapped and manipulated by an optical potential derived from a standard laser beam.

2.6.1 Optical potential implementation

A primary modification of the trap involves modification of the axial (vertical) trapping frequency of the weak TOP trap by overlapping a cylindrically focused, red-detuned laser beam at the cloud position. This beam creates an attractive potential in the axial (vertical) direction, greatly increasing the trap strength (trap frequency) in that direction. In order to create this trapping potential, light from an SPI Photonics 1090-nm 10-W fiber laser is used. Fig. 2.3(a) shows a simplified schematic of the optical system. The output light from the fiber laser has a random polarization and is sent first through a shutter and then through a polarizing beam-splitting cube, resulting in a vertically polarized beam with 5 W of total power; the other output from the cube is not used and is dumped onto a beam block. The vertically polarized light is sent through an 80 MHz acousto-optic modulator (AOM), and the +1 order from the AOM is picked off and collimated to a Gaussian beam radius of 2 mm. By modulating the power of the RF signal being sent to the AOM, the intensity of the light in the collimated beam is controlled. After free space propagation towards the science cell along the x axis, the light is sent through a cylindrical lens of focal length 100 mm. The lens focuses the beam in the vertical (z) direction only, resulting in a sheet of light at the BEC position, with a focused beam waist of $w_{0,z} \sim 23\mu$m in the z direction and a collimated beam radius of $w_{0,y} \sim 2$ mm in the y direction. The light is monitored by a quadrant photodiode on the opposite side of the science cell, as seen in Fig. 2.3(a). The photodiode serves a joint purpose, as the sum of the four quadrants indicates the total intensity of the light incident on the photodiode, and the difference between adjacent quadrants provides beam alignment information. The photodiode is thus used for both intensity and position stabilization, described below.

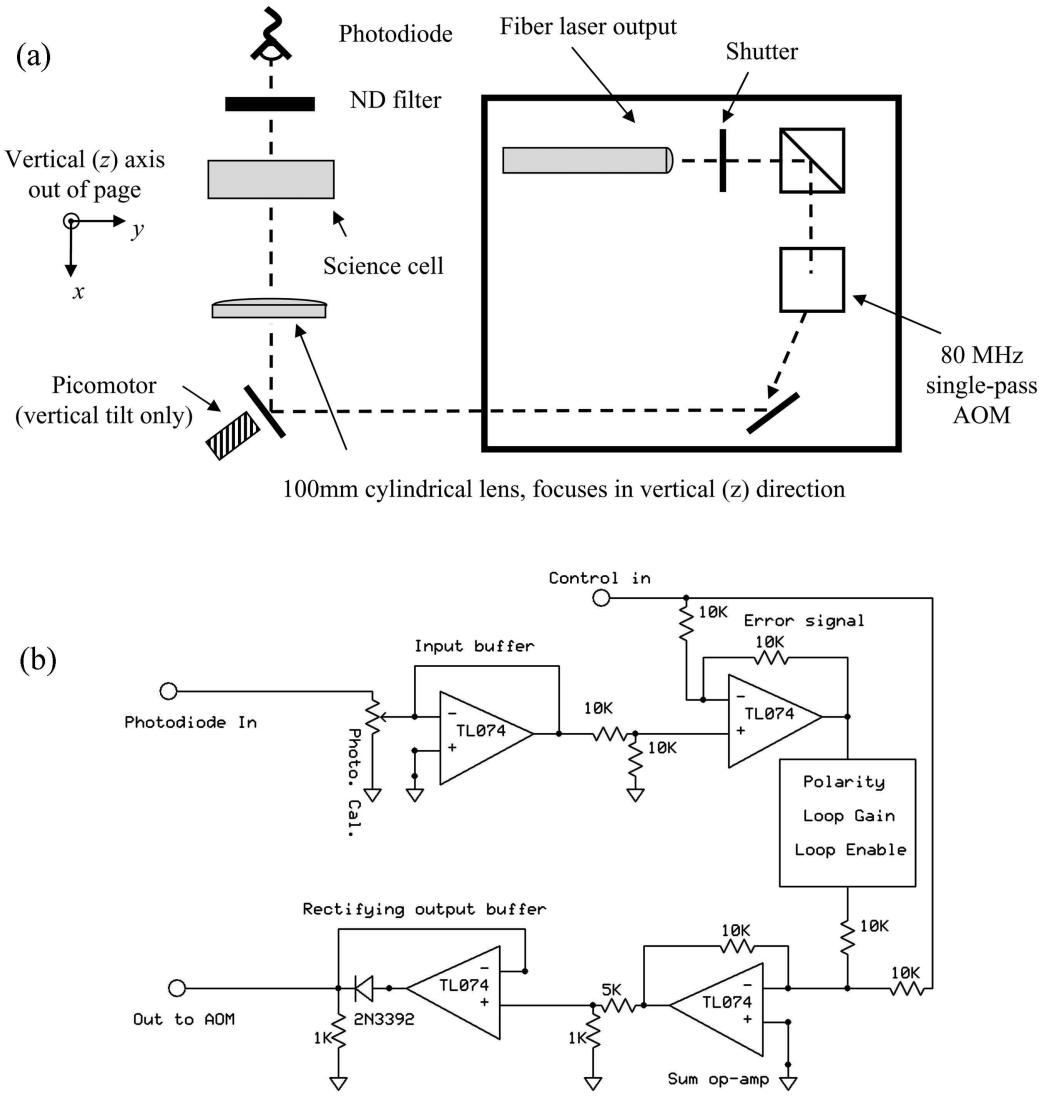

Figure 2.3: (a) Simplified diagram of the optical system for imaging 1090-nm red-detuned light to the science cell, allowing for combined magnetic and optical trapping. The cylindrical lens produces a sheet of light at its focus, primarily modifying the vertical trapping frequency ω_z. The 80 MHz AOM allows the intensity of the beam to be controlled and stabilized. (b) Simplified intensity-lock circuit diagram. See text for explanation.

Utilizing the sum signal from the photodiode, an active proportional-feedback system was implemented. One of the laser lock boxes available in the lab was modified in order to produce the required circuit. Fig. 2.3(b) diagrams the relevant circuit used to implement active feedback. The circuit utilizes two inputs from the experiment and generates an output that drives the AOM. The "control in" voltage is generated by the experiment control computer, which allows the intensity of the beam to be controlled by the overall experiment timing and control program. The "photodiode in" input receives the sum signal from the photodiode located at the end of the optical path; the voltage level of this signal can be adjusted with the potentiometer shown on the circuit diagram. With the shutter open, AOM enabled, and the control input at a voltage typically on the order of 0 V - 2 V, light initially shines on the photodiode. This signal is subtracted from the control, generating an error voltage, which is added to the control in the "sum op-amp." If the error voltage is non-zero, the output will drive the AOM amplitude (thus changing the photodiode signal through increase or decrease of the optical intensity), until the calibrated photodiode signal and control signal match. To simplify the diagram, some of the electronics have been left off; these components are represented by the box labeled "Polarity," which changes the sign of the error voltage; "Loop gain," which amplifies the error voltage; and "Loop enable," which enables or disables the feedback loop. The overall light level incident on the photodiode may be controlled by increasing or decreasing the strength of the neutral density filter shown in Fig. 2.3(a). In total, the circuit allows for an arbitrary intensity at the photodiode to be calibrated to an arbitrary control voltage from the computer. The intensity of the beam is thus tied to the control voltage, allowing a smooth ramp-on or off of the 1090-nm beam intensity.

By subtracting the photodiode signal from the top and bottom quadrants, and the right and left quadrants respectively, the position of the beam is monitored. The vertical position is controlled through a New Focus Picomotor^{TM} piezo-electric actuator, located on the vertical tilt axis of the final mirror mount, allowing precise control over the focused light sheet's vertical position. Active feedback of the beam

position was implemented, but position stability is good enough that the active feedback system was unnecessary. Instead, minor adjustments of the beam position are made at the beginning of a day of data runs, and the vertical beam position remains stable within ± 7 μm throughout the day.

2.6.2 BEC formation in the combined magnetic and optical trap

The atoms are loaded into the combined magnetic and optical trap just before the final stage of evaporation. In this sequence, the cloud is first held in a weak TOP trap[3], with $B'_z = 44$ G/cm and $B_0 = 3.41$ G. By ramping the 1090-nm beam on to ~ 1 W of power over 4 seconds, with the beam precisely aligned at the center-of-mass position of the cloud, efficient loading is possible. Although a linear ramp of the beam intensity is generated by the control computer, the ramp is sent through a $\tau = 280$-ms time-constant RC filter, rounding out the corners of the ramp, which was found to increase the trap-loading efficiency. Care has to be taken to eliminate extraneous vibrations; in particular a cooling fan used to reduce the temperature of the TOP coils has to be disabled for this part of the sequence, as coupled vibrations heat the cloud. The resulting trap depth U_{beam} is several μK when converted into temperature units, which when compared with critical temperatures of BEC formation on the order of ~ 50 nK indicates a strong trapping potential for atoms in the BEC.

Once the cloud is loaded into the combined trap, a forced evaporative cooling RF ramp, similar to that used in the bare magnetic trap, is utilized to form a BEC. The trap frequencies of the combined trap were directly measured through two methods. To measure the vertical trap frequency, a BEC was formed in the combined trap, and the bias-field strength B_0 was modulated harmonically, identical to methods described later in Section 3.4. By looking for catastrophic heating and loss of the BEC as a function of frequency, the vertical trap frequency was determined to be

[3]A final value of $B_0 = 3.41$ G was sometimes used instead of $B_0 = 5$ G, as described earlier. With $B'_z = 44$ G/cm, the sagged TOP trap position was approximately the same as for $B_0 = 5$ G, $B'_z = 52$ G/cm.

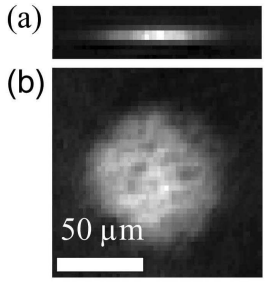

Figure 2.4: (a) *In-situ* horizontal phase-contrast image showing a BEC formed in the combined magnetic and optical potential. Apparent defects visible in the image are artifacts of the imaging process. (b) Vertical absorption image , also *in-situ*.

$\omega_z \approx 2\pi \times 90$ Hz. The radial trap frequencies were measured to be $\omega_x \approx \omega_y = 2\pi \times 8$ Hz by using a magnetic impulse, provided by a single coil, to kick the cloud in a horizontal direction and measure the resulting oscillation period. These measurements imply a weak addition to the radial potential, resulting from the beam, of ~ 1.7 Hz; the radial restoring force generated by the beam is thus $\sim 5\%$ of the force generated by the harmonic magnetic trap, implying that the beam primarily effects only the vertical confinement of the atom cloud. *In-situ* vertical absorption[4] and horizontal phase-contrast images in this R_r:R_z = 11:1 aspect ratio trap are shown in Fig. 2.4(a,b), where R_r and R_z are the radial and axial Thomas-Fermi radii of a BEC in this trap. BECs formed in this trap typically contain $2(0.5) \times 10^6$ atoms[5] at $T \sim 52$ nK ($T/T_c \sim 0.6$). Despite the compressed aspect ratio, the BEC chemical potential is $\mu_0 \sim 8\ \hbar\omega_z$, placing our BECs well within the three-dimensional regime [5, 94, 95].

In several experiments described in this dissertation, an axially propagating blue-detuned repulsive barrier, generated with the use of 660-nm laser light, was also utilized. This beam was mainly used to create a moveable barrier within the trap,

[4]In the context of absorption images, the term *in-situ* implies the magnetic fields are snapped off immediately prior to the pulse of imaging light, hence, although no longer confined to a magnetic trapping potential, the atoms expand minimally before imaging.

[5]Throughout this dissertation, parenthetical notation for uncertainties is used. The value in parentheses (equivalent to $\pm$) is the uncertainty on the same scale as the quoted or mean values. For example, $2(0.5) \times 10^6$ is equivalent to $2 \times 10^6 \pm 0.5 \times 10^6$.

or when aligned at the center of the cloud, a toroidal trap geometry was created. A diagram of the typical optical system used to create this barrier is seen in Fig. 2.5. The focused blue-detuned beam size utilized was chosen specific to the particular experiment being conducted, and was implemented either along with or independent of the red-detuned beam.

2.6.3 Expansion from the combined trap

The highly anisotropic aspect ratio of the combined trap implies a highly asymmetric ballistic expansion as the resulting velocity profile of the cloud is proportional to the harmonic oscillator frequency [1]. By simply snapping the trap to the expansion field, as described previously, and simultaneously snapping off the 1090-nm beam, the aspect ratio of the cloud reverses during expansion; this limits the radial cross-section of the cloud. This expansion proved non-ideal for resolving vortex cores oriented along z. Instead, the magnetic field is snapped to the expansion field, as previously described, but the 1090-nm beam is left on for $\sim 10 - 15$ ms, expanding the cloud in the radial plane. Subsequently, the 1090-nm field is snapped off and the cloud expands for an additional ~ 40 ms. The final expanded cloud aspect ratio is $\sim$ 2:1 (horizontal:vertical).

2.6.4 Transfer to a DC magnetic and optical combined trap

Another useful trap configuration involves the combination of the spherical quadrupole trap and the optical potential, *without* the rotating bias-field. This creates what we refer to as a "DC" trap. The primary motivation for transfer into a DC trap was the removal of any rotating field; this was of interest in experiments involving the *spontaneous* formation of vortices, as described later in Section 7.5.3. However, transfer from the TOP trap to a DC trap presented a series of technical problems that needed to be solved.

A quadrupole trap is plagued by the phenomena of spin-flip Majorana losses [96], where atoms crossing near the B=0 point of the magnetic field lose spin quantization

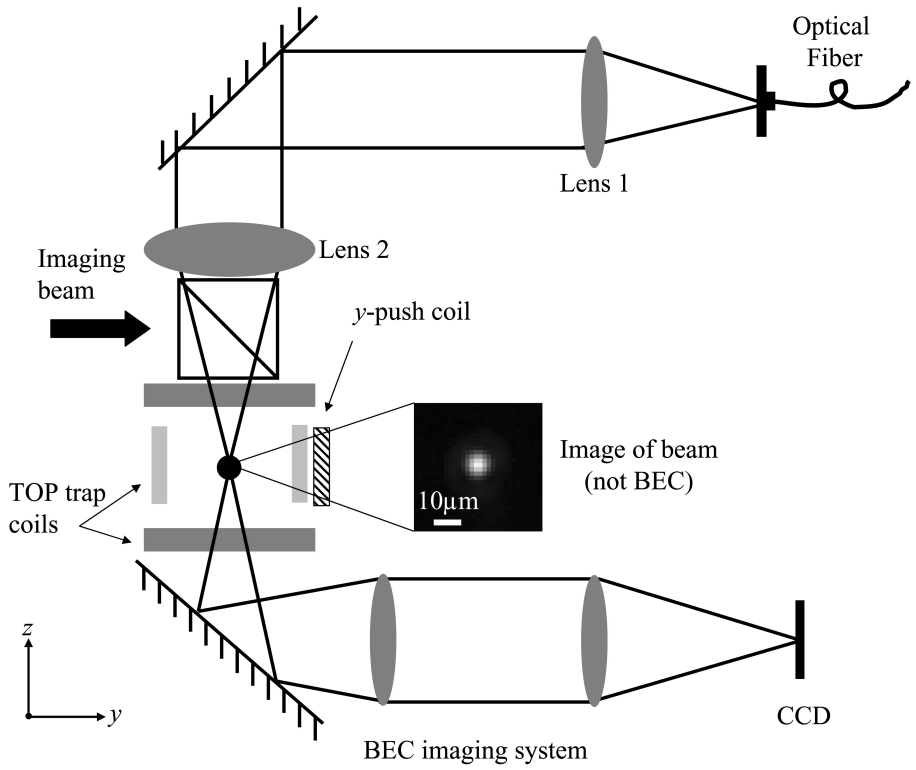

Figure 2.5: Diagram of the optical system used to focus the 660-nm blue-detuned beam onto the BEC location. An image of the resulting focused spot of the beam is shown, with a typical spot size utilized in the experiments of this dissertation. The axially-propagating beam creates a repulsive barrier which may penetrate the BEC, depending on the strength of the barrier. The push coil shown on the figure allowed a magnetic bias field to be created along the y direction, shifting the center of the harmonic trap. There is also a corresponding push coil in the x direction (not shown). These coils allowed the harmonic trap to be shifted in two dimensions.

and are lost from the trap with high probability. This loss mechanism prevents implementation of the entire evaporative sequence in a quadrupole trap, hence the use of TOP traps to form BECs in many experiments. Since the bottom of the weak TOP trap sags, due to gravity [93], from the quadrupole magnetic origin by 0.56 mm in our experiment, the atoms will not experience Majorana losses in a pure quadrupole field as long as they can be confined at the center-of-mass position of the sagged TOP trap. In other words, if they can be kept away from the $B = 0$ point, they will not be lost due to spin flips. However, simply removing the rotating bias field by ramping it to 0 G does not work; the effective gradient due to gravity is ~ 31.6 G/cm, so in a $B'_z = 52$ G/cm field, the atoms will experience a gradient that accelerates them back towards the magnetic origin. In order to keep the atoms at the sagged trap position of the TOP trap, the cloud must remain stationary as the bias field B_0 is ramped to 0 and B'_z is simultaneously ramped to 31.6 G/cm, in order to exactly cancel the effect of gravity. This requirement is complicated by the non-linear relationship between the sagged position and the two magnetic fields, B'_z and B_0. As explained in Ref. [93], the equilibrium trap position in the TOP trap (i.e. the "sag") is given by:

$$\vec{r}_{min} = -\frac{B_0}{B'_z}\frac{\eta}{\sqrt{1-\eta^2}}\hat{z}, \tag{2.2}$$

where B'_z is the quadrupole field gradient, and $\eta = \frac{mg}{\mu B'_z}$, with $\frac{mg}{\mu} \approx 31.6$ G/cm for our atoms. To achieve a constant center-of-mass position r_{min}, the exact expression for the bias field B_0, as a function of B'_z, is given by

$$B_0(B'_z) = r_{min}B'_z\frac{\sqrt{1-\eta^2}}{\eta}, \tag{2.3}$$

where the (-) has been absorbed in the constant r_{min}. This function is plotted in Fig. 2.6(a) for a constant sag of $r_{min} = 0.56$ mm. However, the analytical expression may be approximated by the following function:

$$B_{0,approx}(B'_z) \approx C_1(B'_z - B'_g) + C_2\sqrt{(B'_z - B'_g)}, \tag{2.4}$$

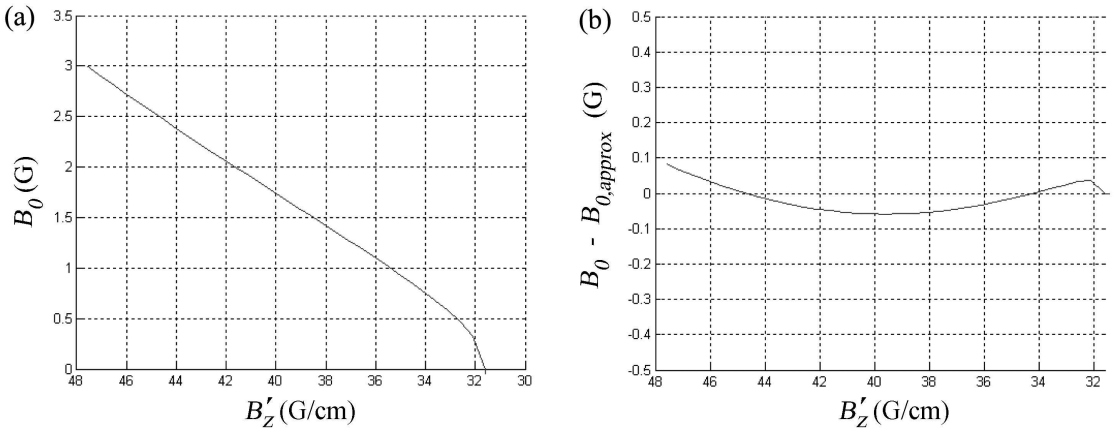

Figure 2.6: (a) Analytical expression of B_0 as a function of B'_z for a constant sag of $r_{min} = 0.56$ mm. (b) Residuals resulting from subtracting equation Eq. 2.4 from the analytical expression; $C_1 = 0.1$ cm and $C_2 = 0.33\ \sqrt{\mathrm{G} \cdot \mathrm{cm}}$. This implies that the approximate expression is good to ~ 0.1 G over the range of values of B'_z.

where $B'_g = 31.6$ G/cm. The residuals generated by subtracting the approximate fit function, with $C_1 = 0.1$ cm and $C_2 = 0.33\sqrt{\mathrm{G}\ \cdot \mathrm{cm}}$, from the analytical expression for B_0 are plotted in Fig. 2.6(b). By ramping the gradient B'_z to 31.6 G/cm and ensuring the bias field B_0 follows this functional form, the residuals indicate there is minimal vertical force applied to the atoms during the transfer sequence; the equilibrium trap position shifts by $\sim \pm 0.02$ mm over the range of B'_z. Since the atoms are confined by the optical potential in the axial direction (the direction of any residual force), implementation of this function allows for transfer to the DC trap.

In order to implement this technique in the experiment, control over a voltage V_{out} controlling the amplitude B_0 of the bias field was transferred to a circuit which implements the following function:

$$V_{out} = A[\alpha(V_1 - V_2) + \sqrt{\alpha(V_1 - V_2)}], \tag{2.5}$$

where the constants A, α, and V_2 are adjustable parameters. A diagram of this circuit is shown in Fig. 2.7. V_1 is the voltage that corresponds to B'_z. B'_z is set by the control computer, and voltage V_1 originates from a Hall-effect probe that

measures the current flowing through the quadrupole coils. V_2 is the voltage from the Hall probe that corresponds to the current in the quadrupole coils used to produce B'_g

Using this circuit, the desired transfer to a $B'_z = 31.6$ G/cm field gradient was accomplished by enabling the circuit and gradually reducing B'_z using the control computer. This sequence was initiated in the trap with $B'_z = 44$ G/cm and $B_0 = 3.41$ G, and the field B'_z was ramped over several seconds. In order to calibrate the circuit, the procedure was initially done without the 1090-nm beam enabled, and the constants A and α were adjusted until the cloud exhibited minimal vertical movement during the ramp. Although there are two adjustable parameters, the calibration procedure mainly involves the adjustment of A; since the circuit must match a $B_0 = 3.41$ G field for $B'_z = 44$ G/cm, the calibration for α may be found by compensating for adjustments in A to satisfy this requirement.

Once A and α were adjusted to keep the cloud approximately stationary, transfer of a thermal cloud starting from the combined magnetic and optical trap was implemented, and condensation was achieved in the DC trap, with a final evaporative cooling RF value of ~ 1.68 MHz. The calculated horizontal trap frequency in this trap is $\omega_r \simeq 2\pi \times 12$ Hz, with the vertical trap frequency (primarily determined by the 1090-nm beam) remaining essentially unchanged from the initial combined trap. Expansion of BECs from this trap allowed vortices to be observed in absorption, and example images, including horizontal phase-contrast and vertical absorption in expansion, are shown in Fig. 2.8(a,b).

2.7 Summary of trap configurations

Table 2.1 summarizes the various trap configurations used in the experiments described throughout this dissertation. The configurations include the bare TOP trap, the TOP with the vertically confining 1090-nm beam, and the DC trap, utilizing the 1090-nm beam and the quadrupole potential.

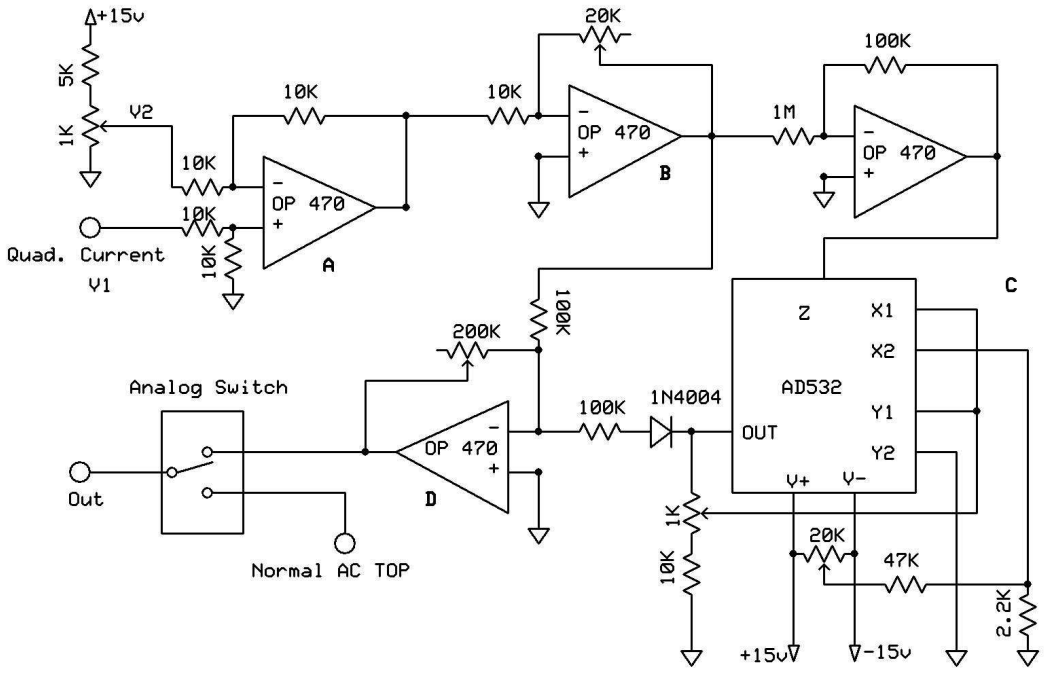

Figure 2.7: Diagram of circuit used to calculate the appropriate bias-field B_0 to approximately maintain a constant sagged TOP trap position. The section labeled **A** computes $(V_1 - V_2)$, with V_2 adjustable using the 1 kΩ potentiometer. Section **B** provides adjustable gain, using the 20 kΩ potentiometer, giving $-\alpha(V_1 - V_2)$. The AD532 chip and op-amp, labeled **C**, is used to calculate $-\alpha\sqrt{(V_1 - V_2)}$. The final stage **D**, an adding op-amp with adjustable gain, using the 200 kΩ potentiometer, gives the desired output: $V_{out} = A[\alpha(V_1 - V_2) + \sqrt{\alpha(V_1 - V_2)}]$.

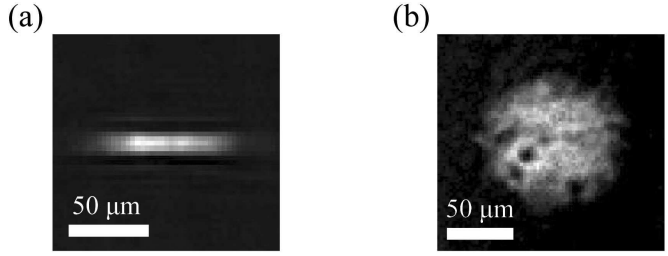

Figure 2.8: (a) *In-situ* horizontal phase-contrast image of a BEC formed in the DC trap. (b) Expanded absorption image of a BEC formed in the DC trap, showing the presence of vortex cores.

Table 2.1: Typical trap configurations used in this dissertation

Trap type	B'_z (G/cm)	B_0 (G)	1090-nm?	$\omega_r/2\pi$ (Hz)	$\omega_z/2\pi$ (Hz)
TOP	52	5	no	7.8	15.2
TOP + 1090-nm	44	3.41	yes	8	90
Quad. + 1090-nm	31.6	0	yes	12	90

CHAPTER 3

CLASSICAL AND QUANTUM TURBULENCE

3.1 Introduction

Turbulent systems are of everyday familiarity: from the eddies in a mountain stream as it flows over a rock, to the airflow at the trailing edge of a moving vehicle, or the convective currents that move heat around a room, one is surrounded by turbulent fluid flows. The study of these systems has a rich history, engaging scientific minds for centuries, dating back to Leonardo Da Vinci [97, 98, 99]. Upon examining his notebooks [100], one finds the following text accompanying a beautifully detailed drawing of flows and eddies:

"Observe the motion of the surface of the water which resembles that of hair, and has two motions, of which one goes on with the flow of the surface, the other forms the lines of the eddies; thus the water forms eddying whirlpools one part of which are due to the impetus of the principal current and the other to the incidental motion and return flow."

Study of turbulent systems is not only interesting from a basic science perspective, but is a field of importance to applied sciences and engineering, where precise modeling of turbulent systems is sought, and may lead to more efficient designs [101]. However, fundamental challenges exist in the effort to produce a fully developed theory of turbulence, as turbulent phenomena possess non-linear dynamics that evade simple description from first principles.

In the study of classical turbulence, theoretical and experimental work has instead centered on descriptions of the phenomenological and statistical properties of turbulent systems [98, 99]. This chapter first reviews some of these basic properties of turbulent classical systems, serving to preface a discussion of turbulence in

quantum systems. Vortex-based models of turbulence are introduced, having special importance in descriptions of quantum turbulence [13, 102, 103] and providing the basis for a microscopic theory of turbulent dynamics in superfluids.

However, not all aspects of such a vortex-based theory are directly testable at a microscopic level in superfluid helium systems, where quantum turbulence has been most studied. Furthermore, some aspects of such theories do not quantitatively match experimental conditions in superfluid helium. Progress in understanding all aspects of vortex creation, dynamics, and dissipation mechanisms in superfluids may therefore further provide a path towards a better understanding of quantum turbulence and, perhaps, classical turbulence. In particular, BECs may be advantageous systems for the study of quantum turbulence beyond what has been accomplished in other superfluid systems. This is due to three factors: experimental methods that permit unprecedented control over vortex creation and manipulation; observation techniques that can track single and multiple vortex dynamics; and quantitatively accurate numerical simulations and theoretical methods based on microscopic models of atom interactions in potential wells and at finite temperatures.

Towards the end of this chapter, experimental investigations conducted in the lab are discussed, where the excitation of a BEC through several methods led to highly excited states that qualitatively appear similar to what might be expected from quantum turbulence. Although these initial results were not immediately pursued, these experiments prompted many of the subsequent investigations contained within this dissertation, which describe efforts to study the formation, dynamics, and decay of quantized vortices in BECs.

3.2 Properties of classical turbulence

The transition to turbulence for a viscous classical fluid occurs with the increase of a quantity known as the Reynolds number:

$$R = \frac{Lu}{\nu}, \tag{3.1}$$

where L is a characteristic length scale, u a characteristic velocity, and ν the fluid's kinematic viscosity. When calculating the Reynolds number in fluid dynamics problems such as the flow around an object, or through a pipe, the characteristic length L is equal to the measured distance to the contact edge of the object, or for flow through a pipe it is equal to the pipe diameter. Fixing the viscosity, but increasing R through increase of the velocity u, relative to the fixed object or pipe wall, a smooth laminar flow of the fluid begins to break up into more complicated fluid flows containing arrangements of non-quantized vortices and eddies. Eventually the system exhibits highly disordered flows, and the average velocity of the flow, relative to the object, is limited. Examining the flow around a cylindrical barrier, for example, as the Reynolds number is increased, the transition region to turbulence generally occurs around $R = 40 - 75$. Up to this point, a pair of mirror-image eddies have formed in the wake of the cylinder. This symmetry of the flow is broken as these Reynolds numbers are surpassed, and with increasing Reynolds numbers approaching $R \sim$200, the resulting disordered flow is in general chaotic in the wake of the cylinder (at least within the *inertial range*, explained below), exhibiting sensitivity to initial conditions and other signatures of chaos. For very high Reynolds numbers ($R \geq 1000$), the turbulence is described as *well developed* [99].

Some basic theoretical concepts in classical turbulence are now summarized. The fundamental equation of classical fluid dynamics is known as the Navier-Stokes equation (NSE):

$$\frac{D\mathbf{u}}{Dt} = -\nabla p + \frac{1}{R}\nabla^2\mathbf{u} + \mathbf{F}, \tag{3.2}$$

where the operator D/Dt is given by $D/Dt = \frac{\partial}{\partial t} + \mathbf{u} \cdot \boldsymbol{\nabla}$ [104]. Here, $\mathbf{u}(\mathbf{r}, t)$ is the velocity of the fluid at position $\mathbf{r}$, ∇p the pressure force, and $\mathbf{F}$ the sum of any external forces. Application of this nonlinear equation, along with boundary conditions proper to the problem at hand, is likely capable of modeling the entirety of the fluid flow, including all of its of turbulent aspects [99]. By taking the curl of this equation one arrives at the equation for an important quantity known as the *vorticity* $\boldsymbol{\xi}$, defined as $\boldsymbol{\xi} = \boldsymbol{\nabla} \times \mathbf{u}$:

$$\frac{d\boldsymbol{\xi}}{dt} = (\boldsymbol{\xi} \cdot \nabla)\mathbf{u} + \frac{\nabla^2 \boldsymbol{\xi}}{R}. \tag{3.3}$$

The vorticity field describes the rotational aspects of the fluid flow. A vortex surface is defined as a surface tangent to $\boldsymbol{\xi}$ at each of its points, and vortex lines, or filaments, are defined as the intersection between two of these tangent surfaces. Conversely, a vortex core, or tube, is a closed loop of surface which is *nowhere* tangent to $\boldsymbol{\xi}$, and the circulation about a vortex tube is given by $\Gamma = \int_\Sigma \boldsymbol{\xi} \cdot d\boldsymbol{\Sigma}$, with $d\boldsymbol{\Sigma}$ the cross-sectional tube area. In contrast to the quantum case described in Section 1.2, the circulation in the classical case can take on any value. Also, one can instead calculate the velocity field starting with the vorticity field, in analogy to electromagnetics and a current carrying wire, by using the Biot-Savart law about a vortex filament [104]. These vortices form the basis of the vortex filament model, where one models the turbulent flow by utilizing vortex filaments as building blocks. This model attempts to provide a microscopic explanation for the statistical properties of turbulence, described below, but classical vortices exhibit some problematic characteristics, and there is also some controversy as to the importance of vortex filaments at high Reynolds numbers [99]. Namely, the vortices are unstable and may continually disappear and reappear, the circulation about a vortex is viscously dissipated and not conserved, and the vortex may take on any value of circulation from a continuum [98]. However, for quantum systems, the theory of vortex filaments is convenient and well-developed, forming the basis of theories of quantum turbulence, and will be described in Section 3.3.

Incorporating the vorticity into a general description of the fluid, one can decompose the velocity vector $\mathbf{u}(\mathbf{r}, t)$ between adjacent points $\mathbf{r}$ and $\mathbf{r} + \mathbf{h}$ as follows:

$$\mathbf{u}(\mathbf{r} + \mathbf{h}) = \mathbf{u}(\mathbf{r}) + \frac{1}{2}\boldsymbol{\xi} \times \mathbf{h} + \frac{1}{2}(\nabla\mathbf{u} + (\nabla\mathbf{u})^T) \cdot \mathbf{h}, \tag{3.4}$$

where the last term on the right hand side, $\frac{1}{2}(\nabla\mathbf{u}+(\nabla\mathbf{u})^T)\cdot\mathbf{h}$, represents deformation of the fluid, and $\nabla\mathbf{u}$ is a matrix of partial derivatives, $(\boldsymbol{\nabla}\mathbf{u})_{ij} = \delta_i u_j$, and $\nabla\mathbf{u}^T$ its transpose. Thus, in general, we may think of the fluid velocity being characterized

by the three parameters of rigid translation, rigid rotation (parameterized by the vorticity), and deformation.

3.2.1 Kolmogorov spectrum

A significant component of the phenomenological description of classical turbulence is the *Kolmogorov spectrum* [105]. This energy spectrum is an important analytical result in the study of turbulence and is significant for many turbulent systems. Conceptually, the model takes the following approach: given the complicated microscopic dynamics of turbulence, one may instead parameterize the system by looking at macroscopic statistical properties of the fluid. One may think of turbulent flow as being comprised of various eddies of different length scales or sizes in the fluid. We may assign the wave-number k_0 to the scale L at which excitations are being injected into the system, where $k_0 = 1/L$. For example, in the case of the flow about a cylinder described above, the relevant length scale is again approximately the diameter of the cylinder. In a viscous fluid with dissipation, there is also a minimum length scale η, corresponding to a maximum wave-number k_{max}, where viscous dissipation becomes significant, given by $\eta = \frac{\nu^3}{\epsilon^{1/4}}$. Here, ν is the viscosity and ϵ is the rate of energy dissipation, $\epsilon = \frac{d}{dt}\int E(k)dk$ (the time derivative of the total energy, where $E(k)$ is the energy per unit mass contained at wavenumber k, in units of length^3/time^2. The range $[\eta, ..., L]$ is known as the *inertial range*. The resulting relation for $E(k)$ is

$$E(k) = C\epsilon^{2/3}k^{-5/3}, \tag{3.5}$$

where C is the dimensionless Kolmogorov constant of order unity [104]. A log-log plot of energy versus wavenumber k shows a constant slope of -5/3.

This expression represents the quasi-steady-state energy spectrum of a turbulent fluid at the end of what is known as a *Richardson cascade*. Drawing pictorial analogy, for convenient visualization, again to the turbulence seen in the wake of a cylinder in a fast moving stream, one sees the initial formation of large vortices

immediately after the cylinder. These gradually decay into smaller eddies, a process terminating with viscous dissipation at the length scale η at the end of the inertial range. The process spreads energy across higher wavenumbers, giving the Kolmogorov spectrum $E(k)$. Multiple systems have provided evidence for the reality of this energy spectrum and, as a broad phenomenological characteristic of turbulent systems, evidence of this energy spectrum is sufficient for determining whether a system exhibits turbulence. However, the microscopic cascade dynamics and the specifics of the Richardson cascade remain controversial [98].

Given these descriptions, one might ask why the problem of classical turbulence remains open. Despite the expected power of the NSE, most of our knowledge of turbulence has come from laboratory and numerical experiments. The NSE *is* solvable for a class of problems at low Reynolds numbers. However, a complete set of solutions to the NSE is necessary for full understanding of classical turbulence, and the task of finding this set is complicated by several difficulties. The NSE is nonlinear, which in itself is not necessarily a fatal blow, but the equation is also not integrable, implying that convergent solutions do not exist for all Reynolds numbers, and in particular for large Reynolds numbers. Further, the NSE is also non-local, coupling small length scales, characterized by the vorticity field, to large length scales, characterized by the velocity field, and vice-a-versa. This non-local aspect presents difficulties for practical models of turbulence, as fluctuations at small, unresolved length scales have a significant effect on the phenomena at resolved length scales [106]. Is it possible to connect the NSE to microscopic models of the turbulent flow, based on vortices? Such a microscopic model is well developed for quantum turbulence, described in the following sections, and may represent part of a path to more complete understanding of classical turbulence [98].

3.3 Quantum turbulence

Feynman was the first to suggest that quantum turbulence in a superfluid might be characterized by a *vortex tangle* [11], consisting of many quantized vortices of

either sign of circulation and orientation, and dynamically characterized by vortex core reconnections and vortex dynamics. Numerical work by Schwarz, simulating the vortex filament model, supported this vortex-tangle picture of quantum turbulence [107, 108]. This picture does not necessarily have an analog in classical turbulence, given the elusive nature of vortices in classical turbulence compared with the stable and well-defined nature of quantum vortices, as described in Section 1.2. However, it has been suggested that the correspondingly well-defined aspects of quantum turbulence may present a path to better understanding of turbulence across classical systems as well. In particular, it is expected that quantum turbulence is likely very similar to classical turbulence on scales large compared with the spacing between individual vortex lines [109]. Additionally, quantum turbulence is theoretically expected to exhibit the Kolmogorov energy spectrum [110], and such conclusions have been supported experimentally in superfluid ^{4}He [111, 112].

Utilizing the vortex filament model described above, in this application more appropriate than in the classical case, the buildup of the Kolmogorov spectrum can be understood through vortex reconnections and vortex dynamics. With a large number of vortices in a superfluid system, and a significant normal component, friction between the two fluid components dissipates energy and drives dynamics. Vortex filaments that pass close enough to each other may cross and connect, with associated sound (phonon) radiation corresponding to each event; sound emission represents another dissipative process in addition to normal-component friction. This Richardson-type cascade is analogous to the classical case, as reconnections distribute energy across smaller length scales. At zero temperature there is no frictional dissipation. However, a particular excitation of vortices known as Kelvin waves [12, 40, 51], which deform a vortex line into a helix in a three-dimensional fluid, are also associated with the radiation of phonons. Phonon radiation is most efficient for large Kelvin-wavenumbers, and Kelvin waves exhibit non-linear interactions which can transfer energy from small wavenumbers to larger wavenumbers. With phonon emission at these large wavenumbers, a route for energy dissipation is established [113]. This quantum Kelvin-wave cascade continues to distribute en-

ergy at smaller length scales at the lower limit of the inertial range [98]. However, Kelvin-wave cascades have yet to be directly observed experimentally.

3.3.1 Generation of quantum turbulence

In superfluid ^{4}He, the first quantum turbulence experiments were realized in fluid counterflow, where the normal and superfluid components flow in opposite directions. Further experiments at the University of Oregon in superfluid ^{4}He [114] realized turbulent superfluid flow in the wake of a grid. Turbulence may also be generated through vibrating structures within the superfluid, including microspheres [115], wires [116], and vibrating grids [117]. Interestingly, the critical velocities for the creation of turbulence in superfluid ^{4}He are quite low, $\sim 5\%$ of the Landau critical velocity[1] expected. This extreme reduction in critical velocity is attributed to vortices remaining from the superfluid transition[2] which are connected to a boundary layer in the fluid; typically, the vortex forms a bridge between the vibrating wire and the container wall. These remnant vortices act to seed the resulting quantum turbulence, and have been the subject of several recent experimental and theoretical investigations [118, 119]. Connections to BEC physics are open for interpretation and speculation, as the absence of boundary layers in a trapped BEC complicate the connection.

The relationship between quantum turbulence in superfluid helium and classical turbulence in a viscous fluid now appears to be established. By supplementing these studies with further quantitative investigations of quantum turbulence in other superfluid systems, such as BECs, an overall better understanding of turbulence in all systems may thus be approached.

3.3.2 Microscopic, mesoscopic, and macroscopic

In this dissertation, the word microscopic is often used to discuss a level of understanding of vortices. Here, what is meant by this term is briefly clarified. Generally,

[1] An experiment investigating the critical velocity in BEC is described in Chapter 4.

[2] See, for example, Chapter 7 for experiments in spontaneous vortex formation in BEC.

models of superfluid vortices fall into three categories: microscopic, mesoscopic, and macroscopic [13]. Microscopic models resolve the vortex core structure, and all aspects of the dynamics are important and monitored. The dynamics modeled by the GPE equation, especially relevant in BEC experiments, where the GPE is strictly appropriate in the zero-temperature limit, resolve the vortex core structure and represent a microscopic model. BECs thus present a convenient system for resolving the microscopic details of vortices, as numerical models have particular relevance when combined with experiments. In mesoscopic models, the vortex core position is important but the microscopic structure is not. The Schwarz equation is an example of a mesoscopic model and is utilized to analyze fluid flow dynamics[3]. The fluid flow about a point vortex is modeled, influencing other point vortices in the system and feeling their respective influence, limited by the boundary conditions of the system. Macroscopic models are concerned with bulk properties, where individual vortices are invisible; the Kolmogorov model is an example.

3.3.3 Turbulence in BECs

Despite the difficulty in studying bulk fluid properties due to small system size and density inhomogeneities, BECs provide some additional advantages over superfluid helium when studying quantized vortices. In contrast to superfluid helium, the vortex core size in a BEC is large enough to image the vortex through optical methods, though only after expansion of the BEC (at least, in experiments to date), or in muli-component BECs [19]. The trapping potentials utilized in BEC work are also highly customizable. These parameters suggest BECs may be convenient systems for studies of quantum turbulence.

The term "turbulence" has been utilized in describing several different experiments in BECs. Experiments that generate disordered arrangements of vortex cores, generated through periodic stirring, have been theoretically predicted to exhibit a turbulent Kolmogorov spectrum [103, 120], and have been experimentally

[3]For a two-dimensional application of the Schwarz equation to map vortex dynamics, see Section 4.3.1.

investigated by several groups [21, 23, 54, 59]. Each of these experiments exhibit a turbulent stage or regime where disordered arrangements of like-charge vortices, approximately aligned with the stirring axis, were observed. The final relaxed state in these cases is a vortex lattice, and these stirring methods have been widely implemented in BECs as a technique for creating vortex lattices[4] and achieving rapid rotations of BECs [34]. Additionally, observations were made of bent and tilted vortex cores generated through periodic stirring. These vortex arrangements were described as a vortex tangle, although limited numbers of vortices were observed [33].

Turbulent vortex tangles have also been utilized as a model for describing the quasi-coherence of a BEC during non-equilibrium relaxation through the BEC phase-transition [121] and the resulting final states have been experimentally investigated in BECs[5] [79].

"Turbulent flow" was established in Ref. [31] by moving a repulsive laser beam across a BEC[6]; vortex-antivortex[7] pairs were uncontrollably nucleated by this process. Interferometric methods were used to indirectly observe the vortices generated.

Turbulent states are also accessible through other excitation methods of a ground-state BEC, and a technique utilizing rotations about two different axes has been theoretically described [103], and experimentally implemented [81, 82, 85]. The resulting clouds show evidence of vortices, although direct measurements demonstrating the Kolmogorov spectrum remain elusive. Referring to Ref. [82], a definition of quantum turbulence is offered:

"*...Quantum turbulence is characterized by the appearance of quantized vortices distributed in a tangled way, not forming regular lattices.*"

This definition relates what is meant in this dissertation when describing the state of a BEC as "turbulent," however, without confirmation of the Kolmogorov spectrum

[4]See Chapter 6 for the description of an experiment utilizing this method of stirring.

[5]See also Chapter 7.

[6]See also Chapter 4.

[7]The term "antivortex," used throughout this dissertation, refers to a vortex with the opposite direction of fluid flow.

or other macroscopic properties of the system, the definition should be viewed as qualitative.

3.4 Prototype experiments

Section 2.6 details the production of condensates in our laboratory in an oblate, radially symmetric ∼11:1 aspect ratio trap. By implementing surface-mode excitations as in [34], vortices were seen emerging at a wide variety of rotation frequencies above and below the radial trap frequency ω_r. In efforts to explore the vortex creation process, the rotating elliptical modulations of the trapping potential (the "stirring" process) were replaced with a pure harmonic modulation of the radial trapping frequency ω_r. In other words, the trap remained symmetric, no rotations occurred, and only the strength of the trap varied in time. This experiment was performed as follows: after creating a BEC, the amplitude of the of the TOP trap's magnetic bias field B_0 was modulated at 9 Hz (compared with a radial trapping frequency of $\omega_r = 2\pi \times 8$ Hz) with a modulation amplitude of $\sim 5\%$ of B_0 for a variable time t_{mod}, with the RF field held at its final value for evaporation. The modulation of the bias field B_0 induces a corresponding modulation in the radial trapping frequency (Ref. [93] details the relationship between B_0 and ω_r), while the vertical trap frequency is generally fixed by the red-detuned light sheet. After the excitation sequence, the BEC was expanded and imaged axially along the radial symmetry axis with near resonant light.

With increasing modulation time t_{mod}, vortices began to appear in the cloud. A sequence of images is shown in Fig. 3.1(a), with each image representing a different run of the experiment. With increased modulation time t_{mod}, vortices, indicated by density dips in the atom cloud image, began to emerge from the cloud edges. Since there is no net angular momentum added to the system, momentum conservation leads one to expect the vortices nucleated in the system are of either sign of circulation about the trap axis. The anisotropic 11:1 aspect ratio trap also implies that vortices will be aligned axially, thus exhibiting good visibility along the imag-

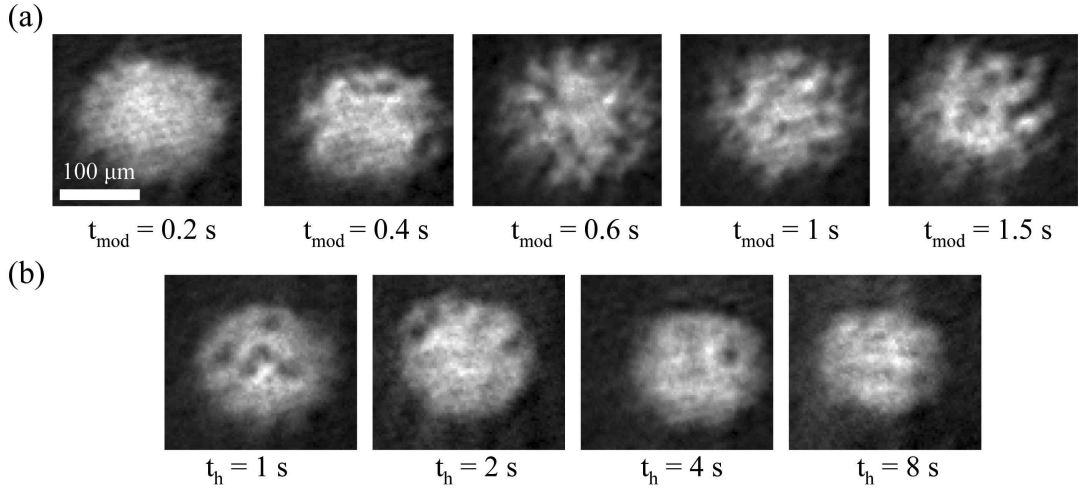

Figure 3.1: Excitation of a harmonically trapped BEC through harmonic modulation of the trapping potential radial frequency, with images obtained in absorption after expansion. Each image represents a separate run of the experiment. (a) With increased modulation time t_{mod}, vortices begin to appear in the cloud, located initially near the cloud edges. The BEC was expanded for imaging immediately after the excitation sequence. (b) After 1.5 s of modulation, the BEC was held in trap for variable hold time t_h. With enough hold time, the BEC returns to the ground state, though with an increased thermal component. On average, it appears that all vortices annihilate each other eventually, suggesting no net angular momentum is added to the cloud during excitation.

ing axis, since the vortex lines should be relatively impervious to tilting [27] and bending [40].

In another test, after a fixed modulation time, a variable hold time t_h in the harmonic trap was added before expansion. With increased hold time t_h, the cloud eventually returned to a state free of vortices, but with an increased thermal component, as shown in Fig. 3.1(b). In particular, a modulation time t_{mod} of 10 s resulted in the complete loss of the BEC. The heating seen indicates the addition of energy to the BEC, and the loss of vortices is consistent with possible damping mechanisms for vortices, including vortex-antivortex annihilation.

These techniques were also implemented in a toroidal trap geometry, created through the use of an additional, axially propagating blue-detuned barrier[8] (de-

[8]For an example of a similar toroidal trap, see Chapter 5.

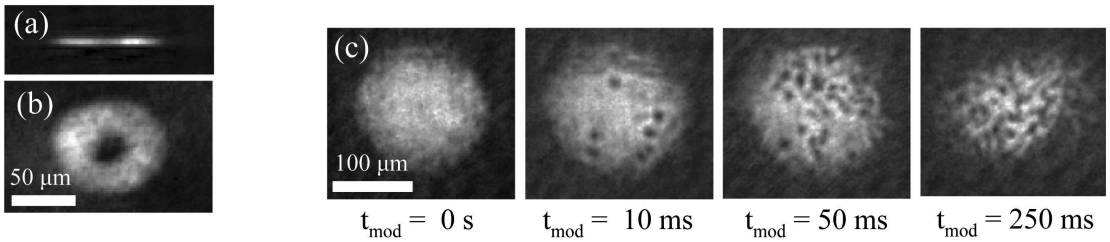

Figure 3.2: Excitation of a toroidally trapped BEC through harmonic modulation of the trapping potential. (a,b) *In-situ* images of the BEC in a toroidal trap, using horizontal phase-contrast and vertical (axial) absorption imaging, respectively. (c) Absorption images in expansion, with each image representing a separate run of the experiment. As the modulation time t_{mod} is increased, vortices begin to appear in the system. In this case, the required modulation time before establishing a highly excited state is much shorter than in the pure harmonic trap case. Additionally, vortices are well defined and appear to originate from within the cloud.

scribed in Section 2.6). Example in-trap images of such a BEC are shown in Fig. 3.2(a,b). By implementing a similar harmonic excitation of the magnetic bias field B_0 at 6.5 Hz, here with an amplitude of $\sim$ 10% of B_0, the system is very quickly driven to an excited state, characterized by the presence of vortex cores. Qualitative differences, when compared with the harmonic trap, are apparent in the image sequence; in addition to much shorter modulation times, the vortices are better defined and appear to originate from within the cloud, rather than near its edge.

Yet another type of excitation was briefly studied to test vortex formation mechanisms potentially relevant for studies of quantum turbulence in BECs. In this case, an axially propagating blue-detuned beam was aligned near the center of the trap, similar to the toroidal trap described above. An *in-situ* image of a BEC with the beam aligned at the center of the BEC and penetrating the cloud is shown in Fig. 3.3(a). However, rather than forming a BEC in this toroidal trap, the BEC was first formed in the harmonic trap, and then the blue-detuned beam was instantaneously turned on to an intensity that penetrated the cloud, as in Fig. 3.3(a), for a short period of time, equal to $\sim$ 7 ms. After the beam was instantaneously turned off, vortex observations were studied as a function of hold time t_h in the harmonic

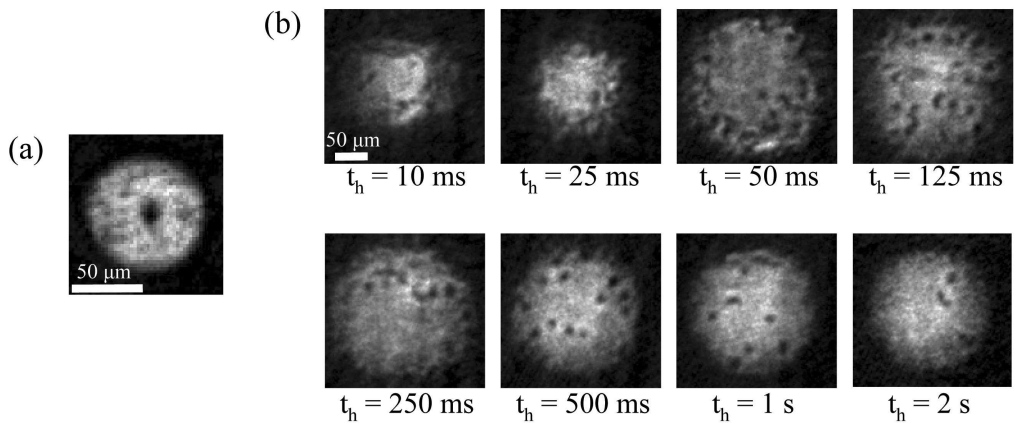

Figure 3.3: Excitation of a harmonically trapped BEC by flashing on an axially-propagating blue-detuned beam for a short period of time ($\sim$ 7 ms). (a) *In-situ* image of the BEC formed in the presence of the beam, demonstrating the beam position near the center of the cloud and a beam intensity that penetrates the BEC. (b) By instead forming a BEC in the harmonic trap and then flashing the beam, excitation of the cloud was observed. Images are axial absorption in expansion, with each image representing a separate run of the experiment. The length scale is the same for each image. As the hold time t_h is increased after flashing the blue-detuned beam, strong density fluctuations in the cloud evolve into vortices. With enough hold time the vortices gradually leave the system. Similar to the other method of exciting a harmonically trapped BEC, the vortices appear to originate on the edge of the cloud.

trap. A sequence of images is shown in Fig. 3.3(b). Apparent strong initial density variations in the cloud immediately after flashing the beam evolve into large numbers of vortices before the system gradually begins to relax with increased hold time t_h. Similar to the case where the magnetic field was modulated in the harmonic trap, vortices appear to originate on the edge of the cloud.

The physical mechanisms at work to produce vortices in these three experiments are not clear. Symmetric harmonic oscillation of the trap will induce corresponding breathing-type oscillations of the BEC, however, such symmetric fluid flows should not be able to produce vortices. There are certainly residual asymmetries in the trap, although any role contributed by these small asymmetries is unknown, but might be accessed through further experiments and simulations. Some aspects of the experiments appear qualitatively similar to what might be expected from

a turbulent state, particularly the large number of vortices present, along with the heating evident in the relaxed system, as shown in Fig. 3.1(b). These states do seem to satisfy the qualitative definition of turbulence offered above, being comprised of many vortices distributed in an irregular way. However, a quantitative connection to turbulence, without measurements indicating a Kolmogorov energy spectrum, is speculative. These experiments do bear some possible similarity to what might be expected from counterflow turbulence, obtained when superfluid is driven into a normal fluid, and thoroughly investigated in superfluid helium. Alternatively, cavitation of vacuum bubbles might be responsible for vortex production [122]. Whether such physical processes are possible in BECs is as yet unknown, and this topic is currently under investigation in the laboratory.

Also interesting is the possible effect of the trapping geometry on turbulence in the system. As noted above, in this flattened cloud vortex bending and tilting are inhibited, limiting vortex dynamics to an unknown degree. These limits on vortex dynamics may effect the development of turbulence and the establishment of the Kolmogorov spectrum in the system [123].

3.5 Relation to the vortex experiments of this dissertation

Considering the difficulty in characterizing these highly excited states, an alternative approach to studying turbulence in BECs was initiated in our laboratory and in the experiments described in this dissertation. Given the paucity of experiments dealing with vortices and antivortices and their dynamics in BEC **we have embarked on a long-term study of quantum turbulence by first understanding the many aspects of vortex creation, dynamics, annihilation, and decay in BECs, coupling experimental studies with theory and numerical simulations**. As experiments become more complicated, **we aim to posess refined experimental and theoretical tools to better understand the microscopic physics of quantum turbulence in BECs**. Our ultimate goal is to connect a firm, quantitative, microscopic understanding of quantum turbulence in BECs with the wealth

of information available from quantum turbulence studies in superfluid helium. We can thereby dream of a more complete understanding of quantum turbulence at all levels, from the microscopic to the macroscopic.

With these goals in mind, a simplified system was explored, described next in Chapter 4, where a single vortex-antivortex pair was controllably created and studied. By extending the technique utilized to create single vortex pairs, multiple vortex pairs were then created in a toroidal trap, described in Chapter 5, leading to the establishment of superfluid persistent currents. The physics of these two experiments may have particular bearing on the highly excited states generated through harmonic oscillation of the toroidal trap, as well as providing controlled studies of vortex-antivortex dynamics and lifetimes. Subsequent to these chapters, Chapter 6 describes an experiment exploring the loss of vorticity from a rapidly rotating BEC due to a controllable inhomogeneity in the trapping potential. These results are important in studying vortex damping mechanisms due to asymmetries in the system, which play an important role in vortex dynamics and vortex lifetimes, and consequently would have a significant role in the dynamics and decay of quantum turbulence in superfluid systems. Finally, a study of vortices resulting from non-equilibrium relaxation through the BEC phase-transition is described in Chapter 7. The quasi-equilibrium states observed result from the evolution of a state theoretically predicted to exhibit turbulence [121].

CHAPTER 4

VORTEX DIPOLES

4.1 Introduction

A vortex dipole in a classical or quantum fluid consists of a pair of vortices of opposite circulation, with the dynamics of each vortex core dominated by interaction with the fluid flow pattern of the counterpart oppositely-charged vortex, as well as the boundary conditions in the fluid. Although single vortices carry angular momentum, vortex dipoles can be considered as basic topological structures that carry *linear* momentum [124] in stratified or two dimensional fluids. Vortex dipoles are widespread in classical fluid flows, appearing for example in ocean currents [125] and soap films [126], and have been described as the primary vortex structures in two-dimensional turbulent flows [124]. In superfluids, the role of vortex dipoles is less well established; however, vortices and antivortices are prevalent in superfluid turbulence, as discussed in Chapter 3. Vortex dipoles are also significant in the Berezinskii-Kosterlitz-Thouless (BKT) transition [64], and phase transition dynamics [79, 121, 127, 128]. This prevalence across a broad set of systems and scenarios implies a quantitative study of vortex dipoles will contribute to a broader and deeper understanding of superfluid phenomena. The realization of vortex dipoles in dilute BECs is especially significant as BECs provide a clean testing ground for the microscopic physics of superfluid vortices [6, 16, 17, 129]. As mentioned previously, the dilute nature of BECs allow for precise modeling with the Gross-Pitaevskii equation (GPE), a relatively simple nonlinear Schrödinger equation. In this chapter an experimental and numerical study of the formation, dynamics, and lifetimes of single and multiply charged vortex dipoles in highly oblate BECs is presented.

Numerical simulations based on the GPE have shown that vortex dipoles are nucleated when a superfluid moves past an impurity faster than a critical velocity,

above which vortex shedding induces a drag force [130, 131]. Vortex shedding is therefore believed to be a mechanism for the breakdown of superfluidity [132, 133]. Experimental studies of periodic stirring of a BEC with a laser beam have measured a critical velocity for the onset of heating and a drag force on superfluid flow [134, 135]. These measurements were based on a sharp increase in the heating rate at a particular stirring velocity, and thus can be considered as *macroscopic* type measurements. Similarly, vortex phase singularities were observed in the wake of a moving laser beam in a subsequent experiment [31, 136], a type of *mesoscopic* observation. However, a *microscopic* picture of vortex dipole formation and the ensuing dynamics has not been established experimentally, prior to the work reported here. In the experiment described in this chapter, single vortex dipoles were deterministically nucleated by causing the highly oblate, harmonically trapped BEC to move past a repulsive barrier, while the BEC was held in the combined magnetic and optical trap. We measured a critical velocity for vortex dipole shedding, and found good agreement with numerical simulations and earlier theory [137]. Experimentally, the nucleation process exhibited a high degree of coherence and stability, allowing us to map out the orbital dynamics of a vortex dipole, and we found that vortex dipoles could survive for many seconds in the BEC without self-annihilation. We also provide evidence for the formation of multi-quantum vortex dipoles.

4.2 Experimental approach

This experiment utilized the trapping potential described in Section 2.6. We created an ^{87}Rb BEC in the combined 1090-nm and $B'_z = 44$ G/cm, $B_0 = 3.41$ G TOP trap, with trapping frequencies $(\omega_r, \omega_z) = 2\pi \times (8, 90)$ Hz. Evaporation in this trap achieved condensation at a critical temperature of $T_c \sim 90$ nK, and produced a BEC of $N_c = 2(0.5) \times 10^6$ atoms at a final temperature of $T \sim 52$ nK. The resulting BEC exhibited a $R_r = 52$ μm measured radial Thomas-Fermi radius, and an axial Thomas-Fermi radius of $R_z \sim 5$ μm.

In addition to the vertically-confining red-detuned 1090-nm beam, a repulsive

optical potential was created through the use of a focused blue-detuned laser beam that penetrated the BEC. The beam was focused onto the BEC by the optical system illustrated in Fig. 2.5 and had a Gaussian $1/e^2$ radius of 10(2) μm. The initial location of the beam was 20 μm to the left of the minimum of the harmonic trap, as shown in Fig. 4.1(a). To nucleate vortices, we translated the harmonic potential in the horizontal (x) direction at a constant velocity until the obstacle ended up 14 μm to the right of the harmonic trap minimum, using a magnetic push coil similar to that shown in Fig. 2.5. The maximum energy of the obstacle was $U_0 \approx 1.2\mu_0$ (where $\mu_0 \sim 8\hbar\omega_z \approx 90\hbar\omega_r$ is the BEC chemical potential), and was held on and constant during evaporative cooling; i.e. the BEC was formed in the presence of this beam. Coincident with the sweep, the height of the obstacle was linearly ramped to zero as shown in Fig. 4.1(b,c). This allowed us to gently create a vortex dipole that was unaffected by the presence of the obstacle, or by heating due to moving the obstacle through the edges of the BEC, where the local speed of sound was small. After a subsequent variable hold time t_h we removed the trapping potential and expanded the BEC for imaging, as described in Section 2.6.3, causing the vortex cores to expand relative to the condensate radius until they were optically resolvable.

4.2.1 Theory details

Simulations of the experimental procedure were performed by Ashton Bradley at the University of Otago, in collaboration with Matthew Davis at the University of Queensland. The methods and results of these simulations are reported in this chapter. At zero temperature, the experiment is simulated using a 3D GPE. An initial state for the combined harmonic-plus-obstacle trap with 2×10^6 atoms was found by integrating the GPE in imaginary time. The potential due to the obstacle laser beam used in the simulations was $U_{\rm S}(x, y, t) = U_0(t) \exp\{-2([x - x_0(t)]^2 + y^2)/w_0^2\}$, where $U_0(0) = 93\ \hbar\omega_r = k_B \times 35$ nK $\sim \mu_0$, and $w_0 = 10\ \mu$m. The barrier is assumed to be constant over the axial position coordinate z, and x and y are radial position coordinates with $(x, y, z) = (0, 0, 0)$ corresponding to the harmonic trap center. The

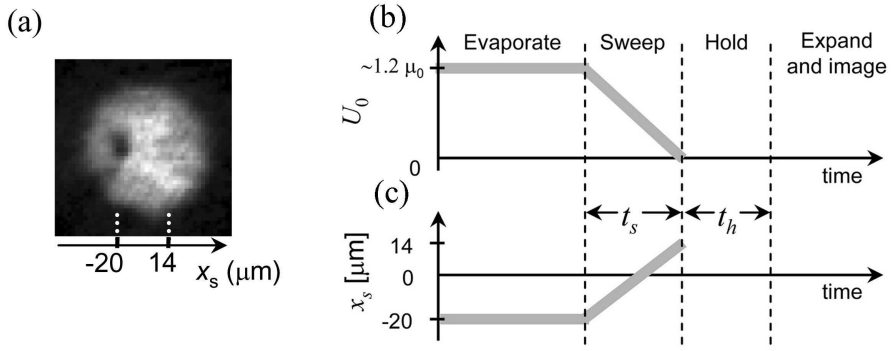

Figure 4.1: The BEC initial state and illustration of the experimental sequence. (a) *In-situ* axial absorption image of the BEC initial state with the obstacle located at $x_s = -20$ μm relative to the BEC center. (b,c) The maximum repulsive potential energy of the obstacle is $U_0 \approx 1.2\mu_0$ (where $\mu_0 \sim 8\hbar\omega_z$ is the BEC chemical potential) and is held constant during evaporative cooling. It is ramped down linearly as the trap translates; relative to the trap center, the beam moves from position $x_s = -20$ μm to $x_s = 14$ μm over a variable sweep time t_s. The BEC is then held in the harmonic trap for a variable time t_h prior to expansion and absorption imaging.

vortex dipole nucleation procedure was modeled by translating the obstacle while leaving the harmonic trap center fixed at $(x, y, z) = (0, 0, 0)$. The obstacle laser beam moves along the x-axis from position $x_0(0) = -20\,\mu$m to $x_0(t_s) = 14\,\mu$m during time t_s and at a variable velocity. As in the experiment, the laser intensity, and thus $U_0(t)$, linearly ramps to zero over time t_s.

4.2.2 Vortex nucleation results

In order to characterize vortex dipole nucleation, we studied the observations of vortex cores as function of the trap translation velocity. For example, in Fig. 4.2(a), a nucleated vortex pair is visible after expansion and absorption imaging. The average number of vortices observed as a function of the trap translation velocity v_s is plotted in Fig. 4.2(b). In our experimental procedure we found a $\sim$ 30% likelihood of a single vortex occurring during condensate formation even prior to trap translation; see Ref. [79] and Chapter 7 for further discussion of spontaneously formed vortices. This gave a non-zero probability of observing a single vortex for

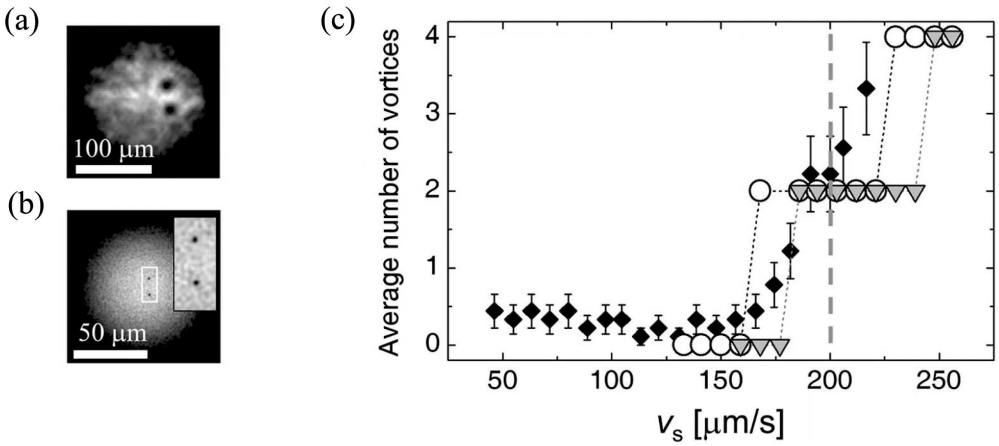

Figure 4.2: For $v_s \sim 190$ μm/s, images show a single pair of vortices having formed in the experiment (a) and simulations (b). Because the vortex core diameters are well below our imaging resolution, the BEC is expanded prior to imaging. Similarly, the vortex cores in the unexpanded numerical image are barely visible; a 10-μm-wide inset provides a magnified scale for the core size. (c) Average number of vortex cores observed for a range of translation velocities v_s with $N_c \sim 2 \times 10^6$ atoms in the BEC. Experimental data points (black diamonds) are averages of 10 runs each, with error bars showing the standard deviation of the observations. Numerical data for $N_c = 2 \times 10^6$ at a system temperature of $T = 52$ nK, corresponding to the experimental conditions, are indicated by triangles joined with dotted lines. Fewer atoms and lower temperatures reduce the critical velocity; as an example, open circles show the results of numerical simulations using $N_c = 1.3 \times 10^6$ and $T = 0$. Above $v_s \sim 200$ μm/s, multiply-charged vortex dipoles are observed. The critical velocity calculated using the methods of Ref. [137] is indicated by the vertical dashed line.

the lowest translation velocities in Fig. 4.2 even when flow without drag is expected.

Referring to Fig. 4.2(b), there is good agreement between simulation and experimental results, and we identified a critical velocity v_c for vortex dipole formation between 170 μm/s and 190 μm/s for $N_c = 2 \times 10^6$ atoms and temperature $T = 52$ nK. Experimental data points (black diamonds) are averages of 10 runs each, with error bars showing the standard deviation of the observations. Numerical data for $N_c = 2 \times 10^6$ at a system temperature of $T = 52$ nK, which corresponded to the experimental conditions, are indicated by triangles joined with dotted lines.

Recently, Crescimanno *et al.* [137] have calculated the critical velocity for vortex

dipole formation in a 2D BEC in the Thomas-Fermi regime. By using the nonlinearity and chemical potential of our 3D system in their 2D expression, we estimated a critical velocity of 200 μm/s. For our conditions, the maximum speed of sound at the trap center was calculated to be $c \sim 1700$ μm/s; our measurements showed that $v_c \sim 0.1c$, consistent with previous measurements of a critical velocity for the onset of a drag force obtained with comparable methods [135].

We emphasize that the simulations described above did not directly correspond to the experimental sequence, where the harmonic trap is translated rather than the obstacle. The acceleration of the BEC due to the turn-on of the magnetic push coil resulted in a small oscillation about the trap center as it translated. Bradley and Davis performed additional simulations to investigate the "impulse" regime where the harmonic trap was instantly accelerated to the sweep velocity, inducing a center-of-mass oscillation of the BEC. The resulting oscillation amplitude was 10 μm or more near the critical velocity, which resulted in a significantly lower critical velocity (~ 80 μm/s), and multiple vortex pairs (see below) were much more readily nucleated at lower trap translation velocities. However, the amplitude of such an oscillation in the experiment was measured to be ≤ 1 μm. These observations thus suggested that the experiment corresponded closer to an adiabatic regime where the translation of the trap is equivalent to translation of the beam. A complete model of the experiment would need to incorporate details of the trap acceleration that were not obtained. However, given the excellent agreement between the adiabatic regime of simulations and the full set of experimental results, including the experimental observations showing minimal BEC sloshing after trap acceleration, we concluded that the simulation methods were appropriate for comparisons with the experimental data.

4.3 Vortex dipole dynamics

In an axi-symmetric trap such as ours, a vortex dipole coincides with a meta-stable state of superfluid flow with potentially long lifetimes [138, 139, 140]. The vortices

exhibit periodic orbital motion, a 2D analogue of the dynamics of a single vortex ring [26, 136]. To observe these dynamics we nucleated a single vortex dipole and held the BEC for variable time t_h prior to expansion and imaging, with results shown in Fig. 4.3(a). Back-to-back expansion images from the experiment are shown, with 200 ms of successive hold time between the 180-μm-square images. The data sequence was taken using an obstacle height 3.15 times larger than that used for the data of Fig. 4.2, as we found this gave the highest degree of repeatability and the least sensitivity to beam displacement.

The repeatability and coherence of the vortex nucleation process was clear: in the back-to-back images with increasing t_h, the vortex positions and orbital dynamics could be followed and the dipolar nature and structure of the superfluid flow is microscopically determined. These measurements also determined the direction of superfluid circulation about the vortex cores, analogous to the case of single vortices [24]: the image sequence showed counter-clockwise fluid circulation about the vortex core in the upper half of the BEC and clockwise circulation in the lower half.

The orbital dynamics were also examined in zero-temperature GPE simulations, as shown in Fig. 4.3(b), showing 62-μm-square images, as the data represents in-trap rather than expanded BECs; the apparent vortex core size is thus smaller in these images. The experimental and numerical data were in good agreement regarding vortex dipole trajectories; Fig. 4.3 (c) shows the average positions x_v and y_v, relative to the center of a Thomas-Fermi fit of the data, of each of the two vortices from 5 sequences of experimental data, generated with an identical sequence as was used to generate the images in Fig. 4.3(a). The larger circle around each average position point represents the standard deviation of the vortex positions at that specific hold time, and was calculated from the 5 images obtained at that time step. A continuous dipole trajectory from sequence (b) was re-scaled to the Thomas-Fermi radius of the expanded experimental images, and superimposed as solid lines on the experimental data. The lifetime of a single vortex dipole was much longer than the first orbital period of $\sim$1.2 s (discussed in Section 4.3.2), although after the first orbit the vortex trajectories became less repeatable from shot-to-shot. However, it is the large-scale

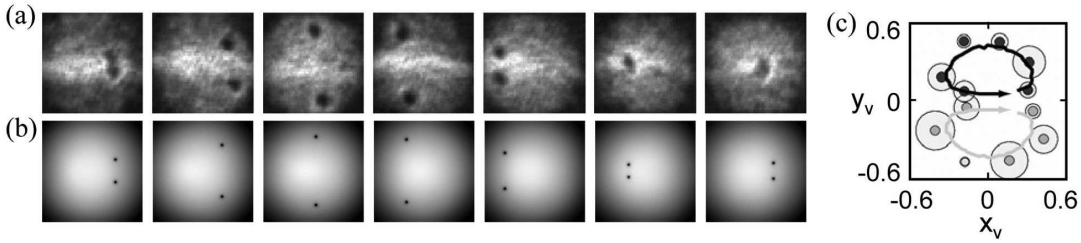

Figure 4.3: Sequences of images showing the first orbit of vortex dipole dynamics. (a) Back-to-back images showing the dipole orbit for a single dipole, with 200 ms between successive images and each 180 μm-square image showing an expanded BEC. (b) 62 μm-square images from numerical data obtained for conditions similar to the data of sequence (a), but for a temperature of T = 0. The orbital period is $\sim$1.2 s, and the apparent vortex core size is smaller in the simulations because we show in-trap numerical data. (c) Black and dark gray small circles show average positions x_v and y_v, relative to the center of the Thomas-Fermi distribution, of each of the two vortices from 5 sequences of experimental data, with each sequence using a procedure identical to that of sequence (a). The larger circle around each average position point represents the standard deviation of the vortex positions at that specific hold time, and is calculated from the 5 images obtained at that time step. A continuous dipole trajectory from sequence (b) is re-scaled to the Thomas-Fermi radius of the expanded experimental images, and superimposed as solid lines on the experimental data; no further adjustments are made for this comparison.

flow pattern of the first orbit that is perhaps most indicative of the qualitative connection with 2D dipolar fluid flows.

4.3.1 Multiply-charged vortex dipoles

For trap translation velocities well above v_c we observed the nucleation of *multiply-charged* vortex dipoles both experimentally and numerically, as shown in Fig. 4.4(a-d). Viewed on a coarse scale the ensuing dynamics were consistent with that of a dipole comprised of a highly charged vortex and antivortex. On a fine scale, particularly in numerical data, we saw loose aggregations of singly quantized vortices with the same circulation at the two loci of vorticity in the dipolar flow. In the experimental images obtained at higher sweep speeds, many individual vortices were often not clearly resolvable for the short hold times shown. Nevertheless, the data resembled characteristics of highly charged dipoles and suggest the formation of

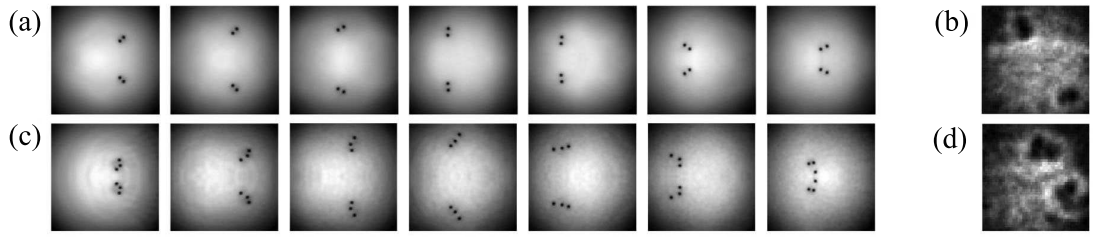

Figure 4.4: (a) Similar to the sequence of Fig. 4.3(b), but for a faster translation velocity with which a doubly charged vortex dipole is formed. Images are spaced in time by 150 ms, and the orbital period is 900 ms. (b) An experimental image in which a doubly charged vortex is formed. (c,d) Similar to (a,b) but for a triply charged dipole. The images of (c) have 112 ms between images and an orbital period of 675 ms.

many vortices because (i) the apparent vortex core sizes became larger, (ii) the orbital time period for the dipole structure was shorter, as expected for higher numbers of cores and faster superfluid flow, and (iii) multiple individual vortex cores were observable for longer hold times.

Although we did not performed an exhaustive analysis of these states, these results are presented to bring attention to these interesting metastable superfluid vortex structures. Examining Fig. 4.4, the times that the loci of the two dipolar flow elements took to complete one orbit were $\sim (900, 675)$ ms for Fig. 4.4 (a,c) respectively. One might at first expect the ratios of these numbers to strictly depend on the ratios of the number of singly quantized vortices around each locus of vorticity. However, this was clearly not the case, and we believe that the orbital periods were strongly influenced by the inhomogeneous BEC density distribution, as discussed below. Second, the numerical data of Fig. 4.4 appear to show that the singly quantized vortices orbit around each moving locus of vorticity. This was indeed seen in the numerical data when finer time scales were examined, although the small-scale orbits of vortices around each vortex dipole locus were not resolvable in our experiments.

Regarding the relative orbital periods, one might expect that the period for a doubly charged dipole, for example, would be close to half that for a singly charged dipole, since the motion is determined by self-induced velocity fields that scale with

the total charge. Experimental and numerical data show that dipoles with higher charges have shorter orbital periods, but that the orbital frequency is *not* linearly proportional to total charge. The origin of this lack of proportionality is not obvious. The two most likely factors that might influence orbital periods are (i) the fact that vortices of like charge do not perfectly coincide in location during an orbit of the entire aggregate, but rather also orbit each other with small spatial separations and a short orbital period, and (ii) the inhomogeneous density profile of the BEC.

To identify the effects of density inhomogeneity on vortex dipole dynamics, Bradley analyzed a flat circular system that had a homogeneous density profile inside radius R and zero density outside. By taking $R = 52$ μm, corresponding to the experiment, he proceeded by numerically integrating the Schwarz equation governing the evolution of point vortices in two dimensions:

$$\frac{d\mathbf{r}}{dt} = \mathbf{V}, \tag{4.1}$$

where $\mathbf{V}$ is the total velocity field induced by all other vortices, their images, and the image of the vortex itself. An image vortex was introduced for each vortex, to set the flow normal to the hard wall boundary to zero [141]. The stable points of the dipole occur at $(x, y) = (0, \pm r_s)$, where $r_s = R/\sqrt{2+\sqrt{5}}$, and are indicated by the crosses in Fig. 4.5; a vortex and antivortex placed at these positions are stationary if there are no other vortices in the system. Displacing the vortex and antivortex from the stable points, with reflection symmetry about the x-axis, led to orbital trajectories qualitatively similar to the dynamics observed in the GPE simulations and the experiment, though with quantitatively different orbital periods. An advantage of the Schwarz equation solution was that the dynamics of perfect charge-2 vortices, such as shown in Fig. 4.4(a), can be compared to the dynamics of doubly charged aggregates of singly charged vortices, such as is shown in Fig. 4.4(b). As seen here in Fig. 4.5(a) and (b), the orbital period of a perfect charge-2 dipole is identical to that of a charge-2 dipole of aggregated single charge vortices. Furthermore, the orbital period seen for these charge-2 cases is exactly half that of a charge-1 dipole (not shown). At least in a homogeneous system, the orbital period does not depend

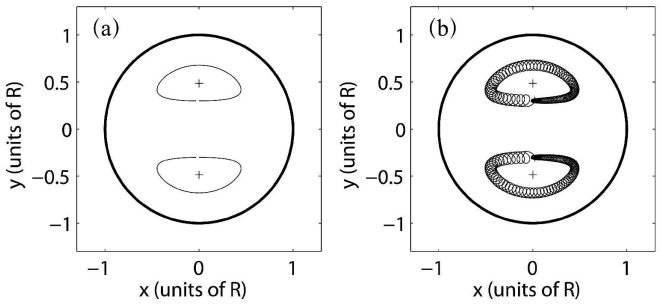

Figure 4.5: Dynamics of a doubly charged vortex dipole in a homogeneous two-dimensional BEC of radius $R = 52$ μm (radius indicated by the thick solid lines) for two cases: (a) the dipole consists of a doubly charged vortex and a doubly charged antivortex, and (b) the dipole consists of an aggregate of two singly charged vortices and a similar aggregate of two singly charged antivortices. In each case, crosses indicate stable points of vortex dipole motion (see text). (a) An example orbital trajectory for the two doubly charged vortices is shown as two thin solid lines. In this example, the period for one complete orbit around the stable points is 4.85 s. The orbital period seen for this charge-2 case is exactly half that of a charge-1 case (not shown) for the same initial vortex displacements away from the stable points. (b) For two charge-2 aggregates of singly charged vortices (a total of two vortices and two antivortices), the trajectories of each vortex core are again indicated as thin lines. The initial positions of the center of each aggregate match those for the vortices of case (a), and vortices within each aggregate are initially separated by 2 μm. As in case (a), the orbital period for the dipole is 4.85 s.

on whether the vortex dipole is made of an aggregate of singly charged vortices or two multiply-charged single vortices. Thus, the lack of direct proportionality of orbital frequency to total charge seen in the experiment most likely arises from the inhomogeneous density profile of the trapped BEC.

4.3.2 Vortex dipole lifetimes

While it is often assumed that in a finite-temperature environment, vortices of opposite circulation will attract and annihilate each other at close distances, this is not necessarily the case: vortices may approach each other so closely that they appear to coalesce — see for example the sixth image of Fig. 4.3(a) with $t_h = 1$ s — and yet still move away from each other after the encounter. Fig. 4.6 shows measurements of the average number of vortices observed with various hold times after

nucleating a vortex dipole. The error bars represent statistical uncertainty (as in Fig. 4.2) rather than counting uncertainty; however, for the doubly charged dipole case there was additional uncertainty in counting vortex cores because we did not always resolve 4 well-defined cores at the earlier hold times. Inset in Fig. 4.6 are two images showing two singly quantized vortices after 4 seconds of hold time in the harmonic trap. The difference between the two images illustrates the variation of vortex position observations after such a long hold time, which precluded our ability to track consistent vortex positions after times much longer than one orbital period. From this set of data, we concluded that singly and doubly quantized vortex dipoles may exhibit lifetimes of many seconds, much longer than a single orbital period of ~ 1.2 s for a singly quantized dipole. With such a strong trap asymmetry between the radial and axial directions, the vortex lines are relatively impervious to bending [40] and tilting [27], and annihilation is suppressed because vortex crossings and reconnections are inhibited.

4.4 Conclusions

Although vortex shedding is the microscopic mechanism for the breakdown of superfluid flow and the onset of a drag force, the nucleation of a vortex dipole does not imply immediate superfluid *heating* since dipoles are coherent structures that are metastable and do not immediately decay into phonons. The maximum energy of a vortex dipole in the BEC was estimated to be $k_B \times 0.45$ nK/atom for our system [134], so that at $T = 52$ nK the temperature would increase by less than 0.5% upon self-annihilation of a single dipole. This temperature change would be very difficult to measure, and microscopic observations of vortex dipole formation and dynamics are therefore complementary to heating and drag force observations.

In this experiment, we demonstrated controlled, coherent nucleation of single vortex dipoles in oblate BECs. The dipole dynamics reveal the topological charges of the vortices and show that the dipole is a long-lived excitation of superfluid flow. Sufficiently rapid translation of the harmonic trap causes vortices with identical

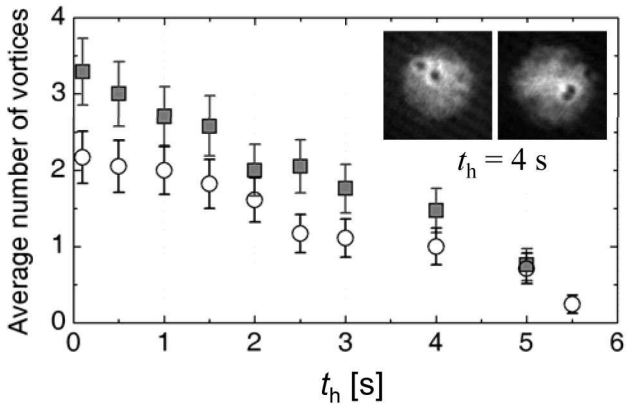

Figure 4.6: Number of vortices remaining after dipole nucleation as a function of hold time t_h, averaged over 17 realizations per data point. The circles show conditions for which a singly charged dipole is created, while the squares show data from a faster sweep where four cores (a doubly charged dipole) preferably occur. The error bars represent statistical uncertainty (as in Fig. 4.2(b)) rather than counting uncertainty; however, for the doubly charged dipole case there is additional uncertainty in counting vortex cores because 4 well-defined cores were not always resolved at the earlier hold times. The vortex cores can clearly persist for times much longer than the dipole orbital period of ∼1.2 s for a singly quantized dipole, and ∼ 0.8 s for a doubly quantized dipole. Inset figures: experimental images of singly charged dipoles obtained with identical sweeps and held for 4 seconds in the trap prior to imaging. The images illustrate the variability of vortex positions after such a long hold time, precluding our ability to track consistent vortex positions beyond one orbital period.

charge to aggregate into highly charged dipolar vortex structures that exhibit orbital dynamics and long lifetimes analogous to singly charged vortex dipoles. This suggests that dipole structures are readily accessible in highly oblate and effectively two-dimensional superfluids, and that they can be qualitatively understood and studied at a microscopic level.

CHAPTER 5

PERSISTENT CURRENTS

5.1 Introduction

This chapter describes an extension of the techniques outlined in Chapter 4 in order to create *persistent currents* in a BEC from an initially turbulent BEC. Persistent currents are interesting in their own right, but this experiment has further implications regarding how vortices interact with trap impurities or roughness, and with a thermal cloud. First a brief introduction to persistent currents is provided, followed by a detailed description of our method used to create these superflows (superfluid flows). Discussion of the persistence of the resulting superflows is provided.

The ability of a superfluid to support fluidic persistent currents follows from fundamental aspects of superfluids confined in multiply-connected geometries [142]. Such a current may persist for long periods of time, as the fluid does not exhibit viscous damping. Crucial to the maintenance of such a flow is a multiply-connected geometry. In our BEC experiments, for example, multiply-connected toroidal traps were created with the addition of a blue-detuned laser beam propagating along the axial direction through the center of the harmonic trap, repelling atoms from the beam focus at the trap center. With the barrier located in the fluid, and at sufficient height such that it penetrates the fluid and sets the size (larger than the healing length) of the spatial region absent of fluid, quantized circulation is supported about the barrier location. This process is similar to vortex core "pinning," where the vortex structure and size is approximately the same as in the bulk fluid, but where the vortex position is confined near a potential minimum created by a barrier. A vortex pinned by a laser beam will be somewhat stable [15, 143], as moving the vortex core and phase discontinuity from the pinning site (beam location) to the bulk atomic fluid is energetically costly. The vortex thus tends to remain located at the beam,

and vortex pinning in BECs has been experimentally studied [68]. This behavior may be generalized to the situation with a large impurity and resulting multiply-connected trap geometry, as quantized circulation will be stably localized at the barrier location. For the case of a wide (relative to the healing length) barrier, we identify this similar with a persistent current [10]. Such currents may exhibit multiple quanta of circulation, and persistent currents have been experimentally observed in superconductors [144], in superfluid ^{4}He [145], and ^{3}He [146], and persistent currents were recently observed for the first time in a BEC [75]. In this chapter a novel mechanism for the creation of multiply-charged currents (superflows) in BECs through the generation of vortex pairs and subsequent thermal damping in a toroidal geometry is described, and evidence for the persistence of the flow is given.

5.2 Experimental procedure

As described in Chapter 4, superfluid flow exceeding a critical velocity can result in the creation of vortex dipoles. The vortex pairs were shown to be long-lived, dynamically moving throughout the condensate with well-defined orbits. The critical velocity measured in the system was $\sim$ 170 μm/sec $\approx v_c/10$, where v_c was the calculated speed of sound in our system, $\sim$ 1700 μm/s. We modified this vortex creation technique, in a way that allowed us to create and selectively collect vortices leading to superflows, by first creating an ^{87}Rb BEC in a toroidal geometry by focusing an axially propagating 660-nm blue-detuned beam through the middle of our harmonic trap, similar to the methods described in Chapter 4 and pictured in Fig. 2.5. Different from the previous methods, the initial collimated beam was reduced in diameter before the final lens, yielding a larger diffraction-limited spot size at the BEC position, with a $1/e^2$ radius of 23(3) μm. The BEC was formed through forced RF evaporation in the combined magnetic and optical potential with the 1090-nm beam and blue-detuned beam turned on. The blue-detuned barrier height U_0 was in the range of $U_0 \sim 131\hbar\omega_r$ to $U_0 \sim 151\hbar\omega_r$, while the chemical potential of the BEC was $\mu_0 \sim 90\hbar\omega_r$. Thus, in units of the chemical potential

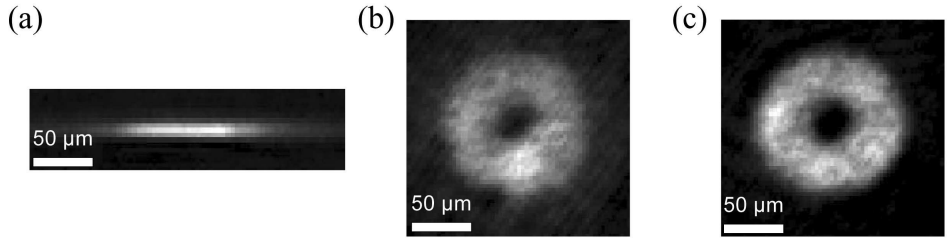

Figure 5.1: *In-situ* images of the BEC in the toroidal trap. (a) Horizontal phase-contrast image, corresponding to the time-step where vortex pairs are generated, but without the blue-detuned beam enabled. (b) Vertical absorption image at the same time-step, with the blue-detuned beam enabled. (c) Vertical absorption image after additional cooling.

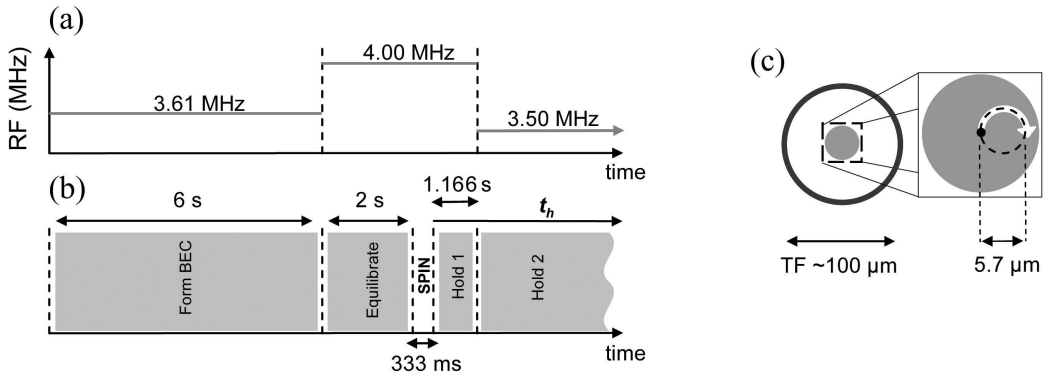

Figure 5.2: Scheme used to create a superflow. (a) RF sequence. (b) Timing sequence (see text). (c) Diagram of the spin sequence, shown relative to the harmonic trap center. The harmonic trap center moves in a circle of $r = 5.7(0.2)$ μm over 333 ms in response to the magnetic push coils (see text). Thus, in the trap rest-frame, the blue-detuned beam (represented by the solid gray circle) appears to circle about its initial position, as diagramed in zoomed in portion of the figure (not to scale). Subsequent to the spin sequence the harmonic trap is held stationary, keeping the blue-detuned beam centered on the harmonic trap.

the barrier height was in the range of $U_0 \sim 1.4\mu_0$ to $U_0 \sim 1.8\mu_0$. As expected, this barrier height produced a clear hole in the middle of the cloud; *in-situ* images are given in Fig. 5.1(b,c), where a flat, annular cloud is visible.

Also different in this experiment compared to the methods of Chapter 4 was the RF evaporation scheme; the scheme is represented in Fig. 5.2(a). The initial jump of the RF from 4 MHz to 3.61 MHz formed a BEC with a considerable thermal fraction

($T/T_c \approx 0.9$, with $T_c \approx 116$ nK) over 6 seconds. The cloud then equilibrated over 2 seconds as the RF was jumped back out to 4 MHz. A circular movement of the harmonic trap center was then implemented, using a pair of magnetic push coils (as seen in Fig. 2.5) driven 90 degrees out of phase. These coils create a bias field in the radial plane whose direction slowly rotates; this technique is a two-dimensional extension of the method used to linearly shift the harmonic trap to create vortex dipoles, as described in Section 4.2. This bias field pushed the harmonic trap center in a circle of diameter 5.7(0.2) μm in 333 ms (3 Hz), while the RF continued to be held at 4 MHz, and the BEC followed the harmonic trap center. A diagram of the spin procedure, in the rest frame of the harmonic trap, is shown in Fig. 5.2(c). Subsequent to the spin procedure, the blue-detuned beam remained at the center of the harmonic trap, and after an additional hold at 4 MHz for 1.166 s (Hold 1 in Fig. 5.2(b)) the RF jumped down to 3.5 MHz (Hold 2 in Fig. 5.2(b)), inducing further cooling. This further evaporation removed much of the remaining thermal component, resulting in a BEC with $T/T_c \approx 0.6$, now with $T_c \approx 82(12)$ nK after 5 s of Hold 2. The cloud was then held for a total variable time t_h (including Holds 1 and 2) of up to 1.166 s + 50 s after spinning, before the blue-detuned barrier height was ramped to zero over 250 ms and expansion and near-resonant absorption imaging were implemented. A summary of the BEC and thermal cloud atom numbers and temperatures during this sequence is given in Table 5.1. Uncertainties quoted in the table were estimated from the fitting routines used to fit the atom clouds. For small numbers of atoms however, such as $N_{thermal} = 0.19 \times 10^6$ in the final row of the table, for example, the fitting routines have limited reliability. Thus, the corresponding temperatures quoted are less certain than indicated.

Table 5.1: Number and temperature during the spin sequence

Sequence Step	Condensate ($\times 10^6$)	Thermal ($\times 10^6$)	$T(nK)$	$T_c(nK)$
End of 6 s jump	0.97(0.19)	2.08(0.42)	103(15)	116(17)
At spin	0.95(0.19)	2.15(0.43)	104(16)	118(18)
End of Hold 1	0.85(0.17)	0.82(0.16)	75(11)	96(14)
5 s of Hold 2	0.86(0.17)	0.19(0.10)	47(7)	82(12)

5.2.1 Vortex creation and pinning

In order to look for the presence of vortices and superflows in our BECs, the above experimental procedure was implemented and results were studied as a function of the hold time t_h, and the evaporative RF values. Examining the first image (t_h = 0 ms) in Fig. 5.3, it is clear that the movement of the beam led to the creation of many vortices, represented by density dips in the image[1]. Such a state has features of quantum turbulence, as the presence of vortices suggests that movement of the beam exceeds the critical velocity of the fluid and nucleates vortex pairs. This results in a disordered arrangement of vortices and antivortices. Treating the blue-detuned beam as a repulsive cylinder of radius $r = 23$ μm, a rough estimate of the velocity of the outer edge point of the cylinder, moving in a circle of 5.7 μm at 3 Hz, gives a velocity of $\sim$ 430 μm/sec, much greater than the measured critical velocity of 170 μm/sec. Additionally, the larger beam size implies that the beam edges are located closer to the edge of the BEC, where the critical velocity is even lower. It is therefore reasonable to expect many vortices and antivortices to be created during the 333-ms spin stage, producing a turbulent initial state.

For each of the images in Fig. 5.3, ballistic expansion of the BEC was implemented immediately after the 250-ms ramp-off of the blue-detuned beam. Moving through the sequence of images in Fig. 5.3, with successive hold time t_h, it appears that vortices begin to leave the system. Since this damping rate was found to be sensitive to the initial thermal fraction immediately before the spin stage, thermal damping is suggested as the primary mechanism for the loss of vortices, consistent with prior work examining vortex damping at finite temperature [35].

The circular motion of the harmonic trap serves to bias the system, putting one sign of vortex closer to the center of the cloud (on average); this implies there is net angular momentum in the system, as vortices close to the center present a greater contribution to the total angular momentum [147, 148]. With vortices close to the blue-detuned beam location, they may be localized to the beam, as was seen

[1]For ease of description relative movement between the beam and trap center is described in the frame of the harmonic potential.

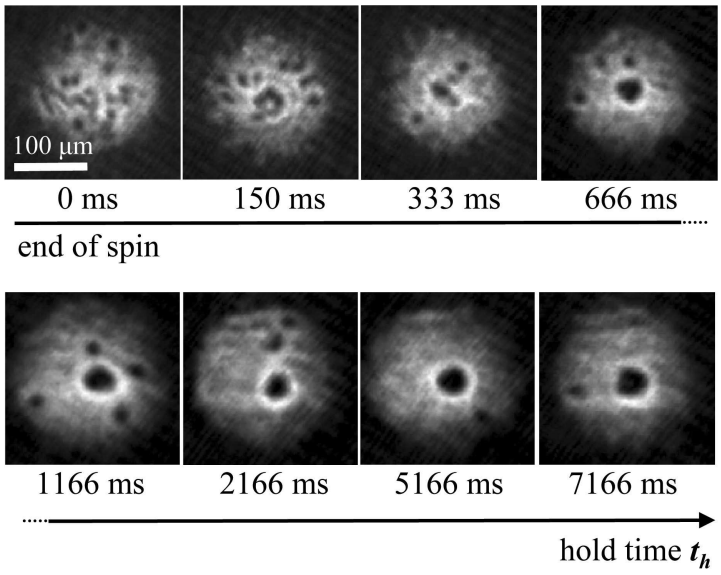

Figure 5.3: Superflow formation process; images are acquired with axial absorption imaging, expanding immediately after the blue-detuned beam ramp-down. Imaging just after the spin ($t_h = 0$ ms), rotating the trap leads to the creation of a turbulent initial state (first image). The image scale is identical for each image. With increasing hold time t_h an apparent superflow is established (indicated by the central dip in the middle of the BEC) as vortices leave the system. After ~ 7 s of hold (last image), a large density dip is visible, suggesting the presence of multiple vortices (see text) at the center of the BEC and the blue-detuned beam location.

experimentally in the work of Tung *et al.* [68]. Eventually, with enough hold time, an apparent superflow is established around the blue-detuned beam in the center of the cloud, and unpinned vortices simultaneously leave the system. The presence of the superflow is indicated by the large dark holes in the images of Fig. 5.3; since these images are taken *after* the beam ramp off, they are not due to the hole in the BEC created by the blue-detuned beam. With the ramp-off of the blue-detuned beam there is no active suppression of the density in the middle of the cloud, and the time required to fill in a non-topological defect is small when compared with the ramp-off time [149]. Thus, the density dip indicates the presence of vortices, and the size of the density dip suggests the presence of multiple quanta of circulation. when compared with the core size of a single vortex. Two singly quantized vortex cores may be seen in Fig. 4.2(a) for comparison. We emphasize that this is not

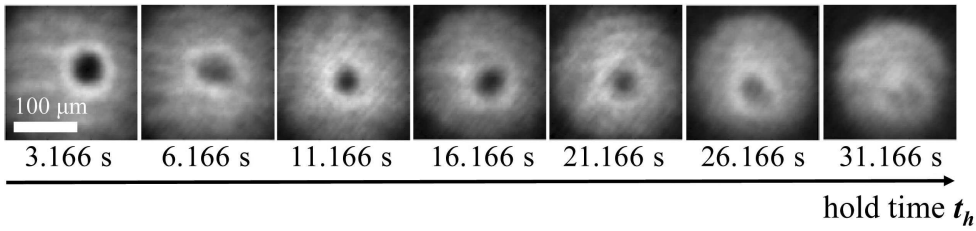

Figure 5.4: Evidence of current persistence. Average of 5 images (see text) taken immediately after the blue-detuned beam ramp-off for each indicated hold time t_h. The large dark spots are indicative of multiple vortices at the location corresponding to the blue-detuned beam. The relative drift of the magnetic trap and beam position (see text) is also apparent in the gradual misalignment of the spot relative to the cloud center.

necessarily indicative of a "giant vortex" as was observed in the work of Engels *et al.* [43], particularly because we do not have the same type of density suppression mechanism at work or the high rotation rates of that experiment. Furthermore, with the pinning potential removed the well-known instability of multi-charge vortices will cause them to break in to single cores [147, 150]. Here, we have removed the pinning potential immediately prior to expansion, so the vortices are still closely spaced together and the limited imaging resolution of the imaging system gives the appearance of a large, central density dip. More details about the loss of circulation about the central blue-detuned beam are discussed in Section 5.2.3, and there was some evidence for interesting metastable arrangements of vortices resulting from the ramp-down of the central blue-detuned beam.

5.2.2 Superflow persistence

By holding a BEC in the toroidal trap for t_h and looking for evidence of centralized vortices after the blue-detuned beam was ramped off, we investigated the persistence of angular momentum in the system. In Fig. 5.4, an average of 5 images[2] from the experiment corresponding to each hold time t_h is shown. The average was generated by directly summing the images together. Again, expansion was implemented

[2]The average image at 11.166 s was generated from 4 images.

immediately after the ramp-down of the blue-detuned beam, as in Fig. 5.3. The images, on average, show the presence of a large central dip suggestive of multiple vortices grouped in the middle of the cloud, as explained above. Over the 31.166 s of hold time examined in the figure, gradual drift of the central dip to the lower portion of the cloud is apparent, and gradual loss of the superflow is seen as the relative contrast of the density dip decreases. Given a measured high degree of stability in optical alignment, which only required adjustment at the beginning of a day of data runs, this core movement is likely due to slow drift in the magnetic trap center: the beam gradually becomes misaligned relative to the harmonic trap. The corresponding loss of pinned vortices is consistent with previous experiments; Ref. [75] observed high sensitivity to barrier beam displacements, leading to the loss of superflows.

In order to resolve individual singly-quantized vortices, we added 3 s of hold time after ramping off the blue-detuned beam but *before* expansion. Without the presence of a pinning potential, and in a finite temperature environment [35], vortices separate and spread out towards the edges of the cloud. With enough additional hold time, the vortices were individually resolvable with the imaging system [147, 150]. The statistical nature of the experiment is apparent, as the number of vortices observed in a current for early hold times varied from $\sim$3 to 5 (inset images in Fig. 5.5).

The black squares in Fig. 5.5 show the average number of vortices counted over 10 runs per data point when spinning up and holding a BEC in the toroidal trap, and implementing 3 seconds of additional hold after the blue-detuned beam ramp-off, allowing the vortices to separate. An exponential fit to the data gives a vortex lifetime of 31(4) s for the toroidal trap. In a second measurement, we ramped down the beam after 5.166 seconds of hold time and then added subsequent hold time; in this way we measured the lifetime of free vortices in our trap. These data points are represented by the grey circles in Fig. 5.5. An exponential fit to this data gives a vortex lifetime of 15(1) s. We see that the lifetime of vortices in the toroidal geometry is approximately double that of the free vortex lifetime, indicating the enhanced support of circulation in the toroidal trap. Note, however,

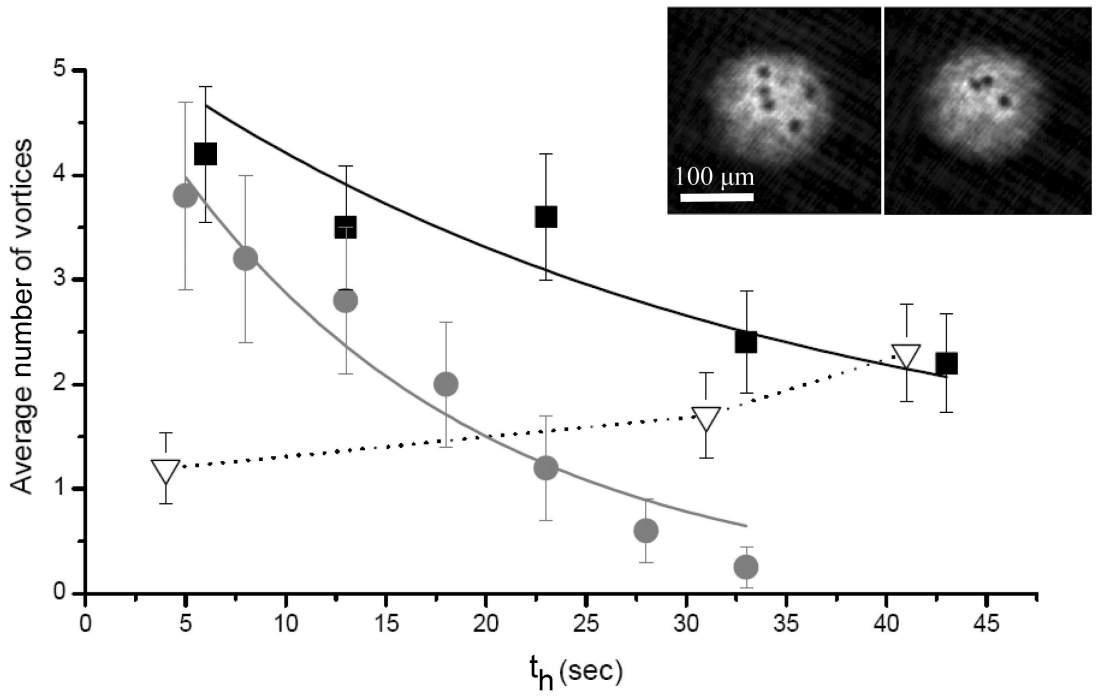

Figure 5.5: Evidence of current persistence, counting vortices. Black boxes represent average number of vortex cores over 10 runs per point, allowing 3 s of hold time after ramp-down of the toroidal beam to resolve individual cores (examples inset). Error bars represent statistical uncertainty rather than counting uncertainty. An exponential fit to the data gives a lifetime of 31(4) s. Grey circles show the lifetime of vortices released from the beam immediately after creating a superflow. An exponential fit gives the lifetime of these free vortices of 15(1) s. White triangles show extraneously generated vortices (see text) with the blue-detuned beam held on but no initial spin of the cloud.

that the angular momentum damping rate is not what is measured. Here, only the numbers of vortices are observed, and their positions are not indicated. Thus, the observations of free vortices show an upper limit of the angular momentum decay rate, and the difference between angular momentum damping with and without the blue-detuned beam is likely to be much greater than a factor of 2.

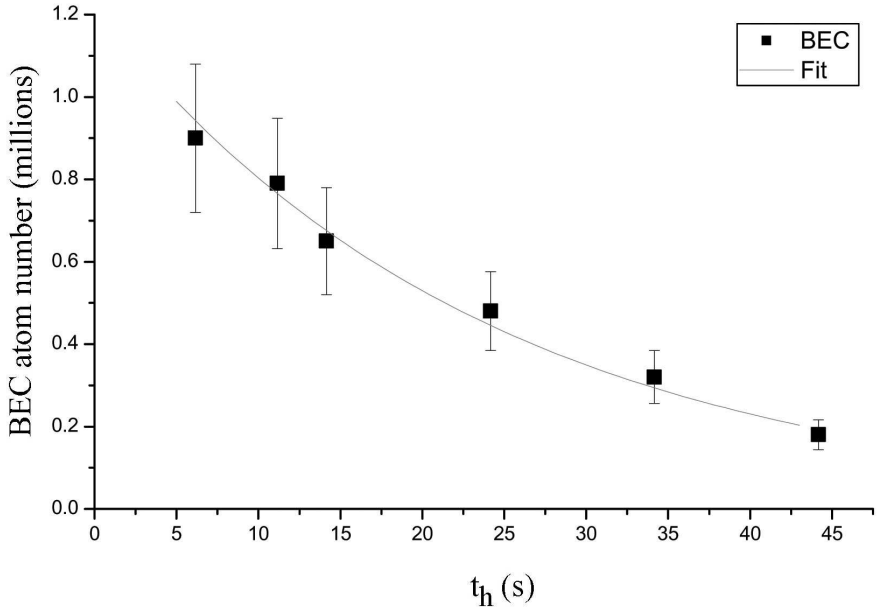

Figure 5.6: Plotted is the BEC atom number for long holds in the TOP trap, without the blue-detuned beam (Hold 2). The BEC atom number decreases with increasing hold time, and an exponential fit the data yields a lifetime of 24(3) s for the BEC atom number.

The white triangles in Fig. 5.5 indicate average vortex observations in the toroidal trap *without* rotating the trap or the beam. The point at $t_h = 4$ s indicates the observation of spontaneous vortices in our system [79][3]. Additional to the magnetic field drift and beam misalignment, the BEC atom number decreases with hold time in the trap (Fig. 5.6), likely due heating through coupling of external vibrations to the combined optical and magnetic trap or some other unknown process. An exponential fit to the data yields a lifetime of 24(3) s for the BEC atom

[3]See also Chapter 7

number. As the BEC lost atoms, and the blue-detuned beam misaligned relative to the trap center, the beam eventually approached areas of low density at the edge of the BEC where the superfluid critical velocity is low, and the creation of vortex pairs is relatively easy. A short study of the vortex observation statistics for a blue-detuned beam aligned close to or intersecting the edge of the BEC indicated it was possible to create vortices without *any* intentional oscillation of the cloud. Given the very small amplitude of circular motion of the beam or the trap necessary to create vortex cores (5.7 μm), along with the reduced critical velocity near or at the edge of the BEC, residual vibration of the beam is suggested as a possible cause of the apparent rise in vortex statistics without spinning. Nonetheless, even when taking into account extraneously created vortices, there is clear separation in vortex observation statistics between the toroidal and harmonic case over a wide range of hold times, and the lifetime of the BEC is even shorter than the decay time of the superfluid current. These are strong indications of current persistence in this system.

5.2.3 Vortex dynamics after beam ramp-down

The dynamics of the vortices after ramping off the pinning potential presented some interesting and perhaps unexpected results. Vortices of like charge tend to repel one another [147, 150], so one might expect that without the pinning potential, the vortices would quickly separate. Instead, as much as 3 s of hold time was required to consistently resolve individual vortices. Fig. 5.7(a,b) shows example images for increasing hold times after the beam ramp down, but before expansion, corresponding to a cold cloud with $T/T_c \approx 0.6$. After as much as a 2-s hold in the trap with this condition, the vortices are still located in the middle of the cloud.

Fig. 5.7(c,d,e) correspond to a slightly lower BEC fraction, with a relative temperature of $T/T_c \approx 0.74$, where $T_c \approx 75$ nK, indicating an increased thermal component. For these images, the RF field was disabled during Hold 2 for 4 seconds before ramping down the blue-detuned beam, thus the BEC is heated by collisions with background atoms, resulting in a higher final cloud temperature. With short holds

after the ramp down of the beam, regular arrangements of vortices shown in the figure were seen infrequently. Fig. 5.7(c) corresponds to a 500-ms hold after beam ramp-down, while Fig. 5.7(d,e) correspond to a 1-s hold after beam ramp-down. As predicted in Ref. [151], regular arrays of vortices are expected when ramping the beam to intermediate heights, starting with a persistent current. It seems possible that the ramp down of the blue-detuned potential implemented above prompted the generation of these regular arrangements. Exhaustive explorations of this phenomenon, and possible connections to cloud temperature, were not conducted in the context of the studies described in this chapter. However, these preliminary results suggest further study of the de-pinning of vortices in this system is warranted.

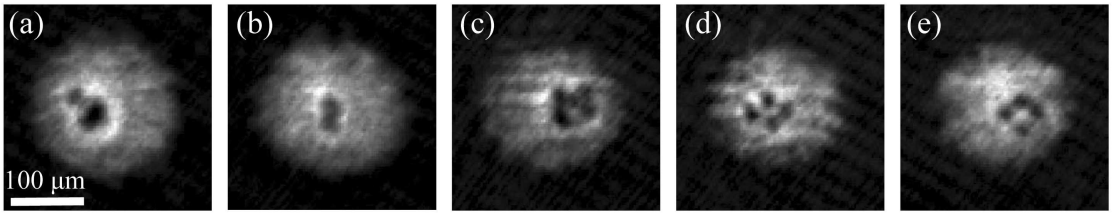

Figure 5.7: Expansion images after producing a superflow, ramping off the blue-detuned beam and holding in the harmonic trap for various times before expansion. (a) 1-s hold after the beam ramps off. (b) 2-s hold. (c) At a slightly higher final cloud temperature, sometimes regular structures were seen, such as this arrangement of what appears to be 5 vortices after a 500-ms hold. (d,e) Arrangements of 4 vortices seen after 1 second of hold.

5.3 Theory results

The stability of a pinned current was investigated by collaborators K. H. Law and P. Kevrekidis, at the University of Massachusetts, and R. Carretero-González at San Diego State University. For large enough numbers of atoms in the BEC, the addition of a central, Gaussian-shaped barrier was found to stabilize a superflow. As the barrier height increased, windows of instability were suppressed, and even in the presence of dissipation (phenomenologically modeling finite-temperature conditions), stable conditions were found. The investigation was able to tie increasing

beam intensity to the ability to pin increasing numbers of vortex cores. In particular, for $N = 2 \times 10^6$ atoms and a Gaussian $1/e^2$ radius of $w_0 = 20$ μm for the central barrier, close to the value measured in the experiment of $w_0 = 23(3)$ μm, the results shown in Table 5.2 were found:

Table 5.2: Vortex pinning vs. barrier height, $w_0 = 20$ μm

Number of Vortices	Barrier height ($\hbar\omega_r$)
3	142
4	144
5	146
6	150
7	154

The barrier heights needed to pin 3-5 vortices show excellent agreement with the experimental conditions ($\sim 131\hbar\omega_r \rightarrow 151\hbar\omega_r$), and the experimental results, where between 3-5 vortices were usually observed after ramping down the blue-detuned beam and waiting for 3 seconds before expanding and imaging.

5.4 Superflow creation without the 1090-nm beam

Utilizing an evaporative RF and spin sequence closely similar to that described in Fig. 5.2, attempts were made to create superflows in the magnetic potential without the 1090-nm beam, but still with the addition of an axially-propagating blue-detuned beam. The TOP bias field B_0 was left at 3.41 G, and with $B'_z = 44$ G/cm, thus the vertical trap frequency is slightly different than the TOP trap described in Section 2.3. The resulting axial trap frequency was $\omega_z \approx 2\pi \times 13$Hz (calculated), rather than $\omega_z = 2\pi \times 15.3$ Hz, and the radial trap frequency was $\omega_r \approx 2\pi \times 8$ Hz. After forming a BEC with an RF jump to 3.50 MHz for 6 s, the RF was jumped out to a value of 3.7 MHz, and a 666 ms spin over two rotation cycles was used. The RF then jumped back to a lower value (3.48 MHz) for a variable hold time, followed by a 100-ms ramp down of the blue-detuned beam and expansion. Despite the smaller radial size of the BEC in this trap, the blue-detuned beam spot-size was

still 23(2) μm. The results in this trap were not as extensively studied, but confirm vortex creation and pinning dynamics similar to the results seen in the flattened trap. An image taken immediately after ramping off the blue-detuned beam over 100 ms and then expanding the BEC is shown in Fig. 5.8(a). Again, an intensely dark spot is seen, with size and optical depth distinctly different from a single vortex core.

Examining Fig. 5.8(b-e) we see again the separation of the vortex cores as additional hold time is added after ramping down the blue-detuned beam. Again, the vortices remained centralized for short times, gradually separating and allowing counting. As many as 7-8 vortices were visible after 5 s of hold time.

5.5 Conclusions

One may ask the question of whether these superflows fulfill the expectations associated with persistent currents. Since a persistent current is characterized by dissipationless flow in a multiply-connected geometry, the limited lifetimes of circulation seen in our experiment seem to limit the applicability of this definition. However, other experimental investigations of persistent currents in BECs (Ref. [75, 84]) saw similar limits on the lifetimes of their flows ($\sim$ 10 s), suggested as being due to blue-detuned beam misalignment. The similar relative misalignment of the blue-detuned beam in our experiment, in combination with the loss of BEC atom number, implies systematic, rather than fundamental, limits on the persistence of these superflows;

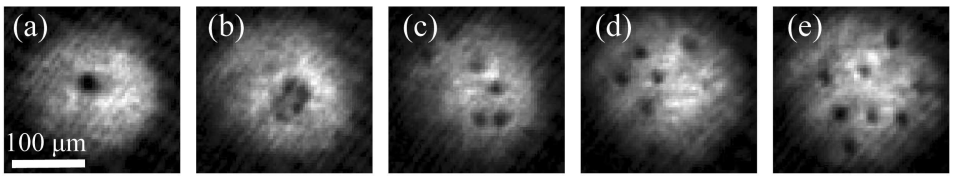

Figure 5.8: Expansion images after producing a current in the trap without the 1090-nm beam, ramping off the beam and holding in the harmonic trap for various times before expansion. (a) No hold after the beam ramps off. (b) 250-ms hold. (c) 750-ms hold. (d) 3-s hold. (e) 5-s hold.

in particular the BEC atom number lifetime of 24(3) s is even shorter than the vortex lifetime of 31(4) s in the toroidal trap. In fact, for particularly long hold times centralized density dips indicative of a superflow were seen infrequently and not extensively studied; Fig. 5.9 shows such an image for $t_h = 51.166$ s.

The observation of persistent currents in BECs further demonstrates the superfluid nature of the condensed gas. These results do not represent the first observations of persistent currents in BECs, but emphasis is given to the novel mechanism described for their creation. Although the final results are statistical in nature, with variable numbers of vortices resulting in any realization of the experiment, the method was relatively easy to implement.

The suitability of this method for creating persistent currents in a regular TOP trap highlights the effectiveness and wide applicability of the method, useful in both flattened condensates where vortex bending [40] and tilting [27] are inhibited, and in more three-dimensional clouds where they are not. Even though in the 2:1 aspect ratio trap, vortex dipoles are not as visible early in the sequence, and would be expected to have short lifetimes in this trap [71], the effectiveness of the blue-detuned beam is apparent. Localized circulation was visible (aligned with the blue-detuned beam propagation axis), and up to 7-8 vortices were counted after the beam ramp down. This method thus appears to have wide applicability in TOP traps for stochastically generating persistent currents with large winding numbers.

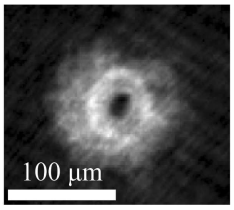

Figure 5.9: A centralized density dip, indicating superfluid circulation about the blue-detuned beam, for $t_h = 51.166$ s. The BEC was expanded and imaged immediately after the ramp-down of the blue-detuned beam. Note the smaller size of the expanded BEC when compared with Fig. 5.7, for example, consistent with the smaller BEC atom number after a long hold in the toroidal trap.

Furthermore, it was relatively easy to create large numbers of vortices in a flattened toroidal trap with a small spin amplitudes, or even without spinning. This relates to the ease of driving the system in to a highly excited state in the flattened toroidal trap (see Chapter 3). The initially turbulent BEC state was driven into a persistent current state through interaction with the blue-detuned impurity at the center of the cloud, and the background thermal atoms. These are perhaps the most interesting aspects of this persistent-current formation mechanism. With this work we have demonstrated the possibility of microscopic studies of three important pieces of the turbulence puzzle in BECs: (i) the formation, (ii) damping, and (iii) evolution of such states. This work opens the door for future studies linking these three ideas. Also, the reliance of the system on thermal damping in order to establish the current showcases interesting physics. Studies of such "open quantum systems" are of general and wide interest.

CHAPTER 6

SPIN DOWN OF A VORTEX LATTICE

6.1 Introduction

In addition to studying how one may rotate a superfluid and introduce vortices into the system, it is interesting to examine how angular momentum and vorticity is lost. Of particular interest is the sensitivity of the system to defects and asymmetry in the trapping potential. These asymmetries may have an important effect on vortex lifetimes and vortex dynamics, and understanding the behavior of vortices in the superfluid system is consequently important in understanding the behavior of quantum turbulence in the system. Studies of rotating superfluid helium have previously investigated vortex damping, often described in terms of the interaction between the normal and superfluid components [12]. Damping may also be induced through the interaction of the vortices with other quasi-particles in the fluid [152]. Vortices may also decay through the emission of phonons and through Kelvin-wave oscillations [12, 40, 51]. However, few experiments have focussed on damping of vortices due to impurities. BEC systems are attractive for such a study as the symmetry and smoothness of the trapping potentials can be highly controlled. For example, experiments described in Ref. [43] controlled the symmetry of a TOP trap allowing for very long lived atom-cloud rotations (up to 5 minutes). The careful control of trap symmetry also allowed for the generation of large vortex lattices.

Conceptually, the effect of radial-plane asymmetry in the trap may be seen from the following equations [153]. First, we may write the expectation value of the angular momentum of the BEC about the z-axis:

$$\langle\psi|L_z|\psi\rangle = i\hbar \int \psi^*(\vec{r},t)\frac{\partial}{\partial\phi}\psi(\vec{r},t)d\mathbf{r} \equiv \langle\psi|(\vec{\mathbf{r}}\times\vec{\mathbf{p}})_z|\psi\rangle. \tag{6.1}$$

Here, $|\psi\rangle$ is the BEC quantum state, $\vec{\mathbf{r}}$ the position operator, and $\vec{\mathbf{p}}$ the momentum operator. We can then take the time derivative of this equation, giving:

$$\frac{d\langle L_z\rangle}{dt} = \frac{1}{i\hbar}\int |\psi|^2(\vec{\mathbf{r}}\times\vec{\mathbf{p}})_z V(\mathbf{r})d\mathbf{r}. \tag{6.2}$$

The momentum operator may be written in spherical coordinates as

$$(\vec{\mathbf{r}}\times\vec{\mathbf{p}})_z = \frac{\hbar}{i}\frac{\partial}{\partial\phi}. \tag{6.3}$$

Thus, for a time-independent potential $V(\mathbf{r})$ with radial symmetry, $\frac{d\langle L_z\rangle}{dt} = 0$. If the potential instead has radial *asymmetry* the angular momentum is not conserved when considering *only* the BEC and ignoring any exchange of momentum between the BEC and the trapping potential.

In order to study the effect of trap asymmetry on the angular momentum of our BECs, we first spun up the BEC such that many vortices were in the cloud, and then carefully added an asymmetric element (an impurity) to the potential. By examining the decay of vortices (thus angular momentum decay) versus interaction time in the perturbed potential, an experimental picture of the decay of angular momentum in our system was obtained.

6.2 Vortex lattice creation

Vortices were added to the BEC through direct transfer of angular momentum from a rotating asymmetric potential. This transfer of angular momentum was accomplished through the following well-established method, first experimentally implemented and described in Ref. [34], and widely utilized [18, 154].

In the normal configuration of the TOP trap, the path of the rotating instantaneous minimum of the spherical quadrupole potential (see Section 2.3) traces a circle in the radial plane; the method employed here modifies this circle into an ellipse, with a slow rotation of the major and minor axes. In the initial TOP trap configuration, two sinusoidal waveforms at $\omega_{rot} = 2\pi \times 4$ kHz drive two orthogonal coil pairs oriented in the radial plane. The combination of the resulting two

orthogonal magnetic fields is the bias field of strength B_0, whose direction rotates in the radial plane at angular frequency ω_{rot}. In order to modify the symmetric trap to create an ellipse in the radial plane, two additional relatively low-amplitude 90° out-of-relative-phase sinusoids are generated, at angular frequency $\omega_{mod} \sim \omega_{rot}$. One of these signals is added to the signal that drives one coil pair, and the other is added to the signal driving the orthogonal pair. Examining one of the resulting final signals with the addition of the extra sinusoid, for a fixed phase relationship of 0° between the initial signal and the added sinusoid, the amplitude of the total signal is reduced; the converse situation applies for the orthogonal total signal, which is increased. Thus, for $\omega_{mod} \equiv \omega_{rot}$, implying a fixed phase relationship between the signals, the result is a stationary ellipse. However, if $\omega_{mod} \neq \omega_{rot}$, then the phase relationship between the signals varies at an angular frequency of $\Delta\omega/2$, where $\Delta\omega = |\omega_{mod} - \omega_{rot}|$. As the amplitudes of the two signals vary with the relative phase, the ellipse rotates in the radial plane at angular frequency $\Delta\omega/2$. The ratio of the minor and major axis (set by the amplitude of the additional sinusoids) of the ellipse utilized to spin up vortices in our experiment was ~ 0.8. This approach to creating vortices is well-known, and details of this trap configuration may be found in Ref. [34]. More extensive details of the electronic circuit and signal generators used to create the bias field B_0 in our experiment may be found in Ref. [8].

Vortices will be created by rotating the ellipse at $\sim 0.7\omega_r$ [34]. In our experiment, a value of $\Delta\omega \sim 2\pi\times 12$ Hz was used (resulting in a $2\pi\times 6$ Hz $= 0.78\omega_r$ rotation of the ellipse). This method was implemented in the magnetic trap without the presence of the 1090-nm red-detuned beam, hence the trapping frequencies are $(\omega_r, \omega_z) = 2\pi\times(7.8,15.3)$ Hz respectively. Crucial to the creation of a vortex lattice in this scheme is control of the forced evaporation RF values. After creating a BEC with forced evaporative cooling, the RF was jumped out to a high value ($\sim$ 7 MHz), for 4 seconds of spinning. The RF was then jumped back down to a lower value ($\sim$ 5 MHz) and after and 1.5 seconds of hold time t_h, now back in the normal TOP trap, we produced a lattice of vortex cores. After subsequent expansion and axial absorption imaging, such a rotating state is seen in the leftmost image of Fig. 6.1.

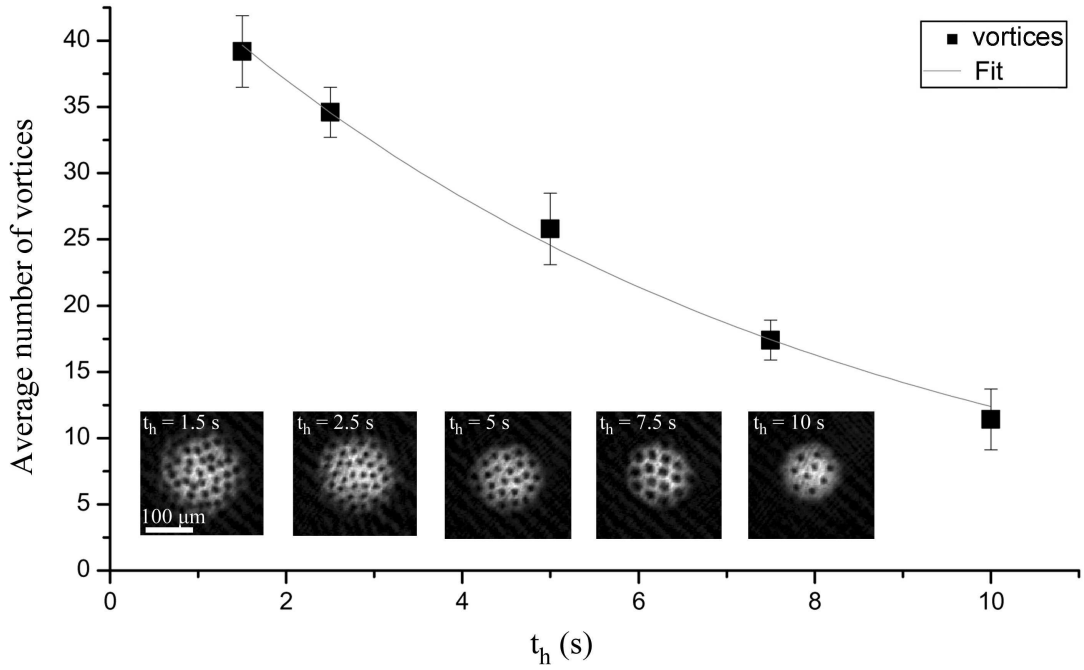

Figure 6.1: Measured vortex lifetime in the bare magnetic potential, each point is averaged over 4 realizations of the experiment. The error bars represent the standard deviation. An exponential fit to the data gives $\tau = 7.3(0.4)$ sec. (inset) Example absorption images after expansion, showing the resulting lattice and its decay. Each image is taken from a different run of the experiment. The length scale for each image is identical to that shown on the leftmost inset image.

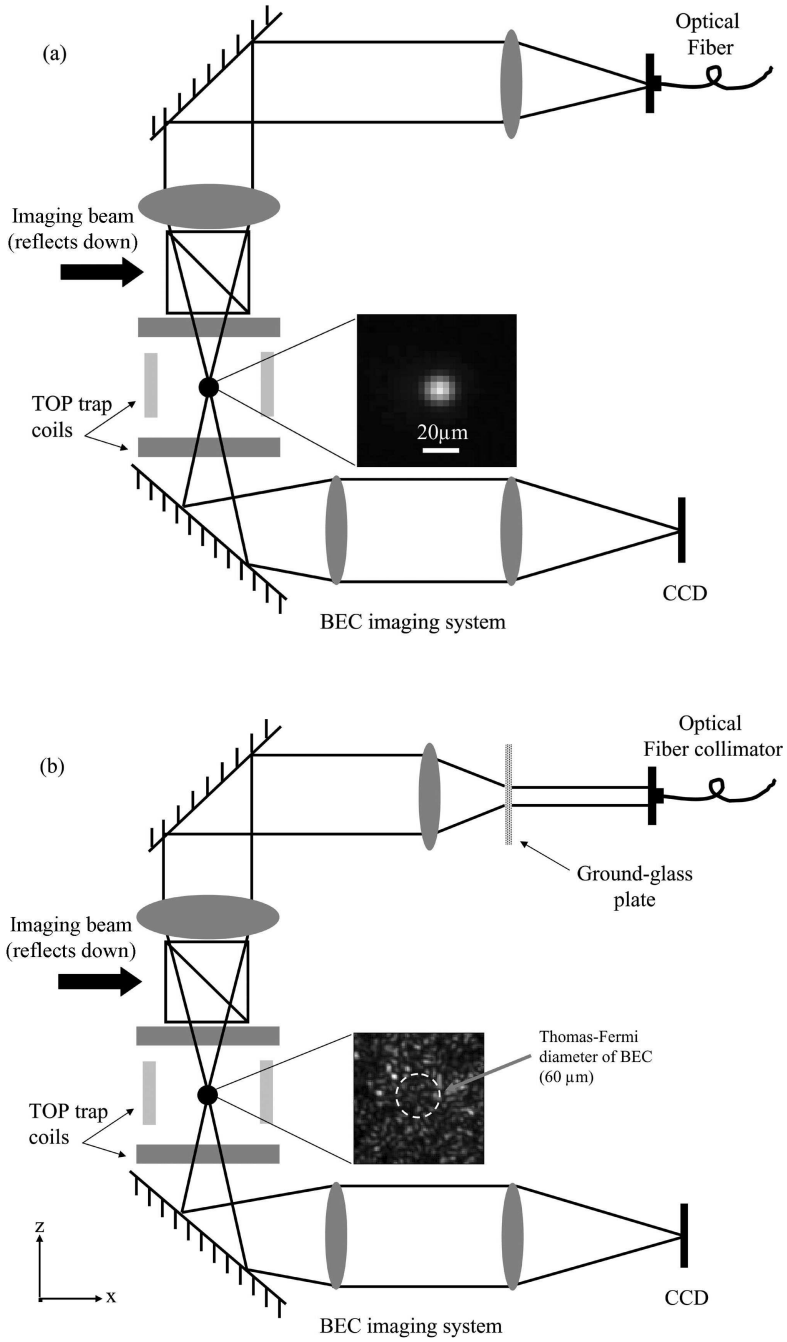

Figure 6.2: (a) System to focus the blue-detuned Gaussian beam onto the BEC. The beam focus occurs at the BEC location, and the $1/e^2$ radius was $w_0 = 23$ μm. (b) Similar system, but set up to image speckle on to the BEC. The optical fiber terminates in a collimator, and is incident on a ground-glass diffuser. The ground-glass plate is placed one focal length away from the closest lens and imaged to the BEC location through the second lens. An example speckle pattern is shown, with the Thomas-Fermi radius of the BEC superimposed.

Due to residual uncontrolled asymmetry in the magnetic trap, as well as the presence of a thermal cloud [35], the lifetime of vortices is finite. In other words, vortex number and hence angular momentum decreases with hold time t_h in our trap. Starting with a lattice of ∼40 vortices, we held the resulting cloud in the trap to measure the vortex lifetime, and an exponential fit to the data yields a lifetime of 7.3(0.4) s as shown in Fig. 6.1. Note that these images were obtained absent the presence of any impurity.

6.3 Lattice damping with a Gaussian beam

To add asymmetry to the trap, two methods were used: the addition of a Gaussian bump to the potential, and the addition of a disordered potential created by imaging optical speckle onto the BEC location (Fig. 6.2). First, the addition of a Gaussian bump to the potential will be described. By focusing a blue-detuned 660-nm wavelength beam along the axial direction of the trap, a bump is created. The 660-nm laser light propagates through the system shown in Fig. 6.2 with a resulting focused spot size at the BEC location of 8(2) μm. This repulsive potential was then positioned at 3 different places within the BEC. These included a spot $\sim$ 7 μm away from the center of the BEC, one aligned $\sim$ 14 μm away from the center of the BEC (approximately half of the Thomas-Fermi radius of $R_{TF} = 30(2)$ μm), and one intersecting the edge of the BEC, with the beam center aligned $\sim$ 20 μm away from the center. *In-situ* images in absorption, showing the beam penetrating the BEC are shown in Fig. 6.3.

For each of the three beam positions, a lattice of cores was produced, the beam was ramped on with a fixed rate up to a variable intensity, held on for a variable amount of time, and then ramped off. The cloud was expanded and imaged with near resonant light, and vortices were counted. Details of the beam ramp-on, hold-time, and ramp-off are summarized below.

In general, the scheme for investigating the dissipation of angular momentum in the system is shown in Fig. 6.4. In each case, a lattice was generated with a 4-s

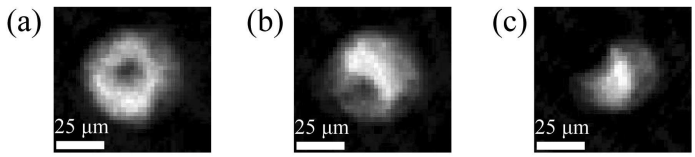

Figure 6.3: Three different beam positions were utilized in the experiment, here shown with *in-situ* absorption images. (a) Beam was aligned ~ 7 μm away from the center of the BEC. (b) Beam was aligned ~ 14 μm away from the center of the BEC, or approximately half of the Thomas-Fermi radius of the BEC, with $R_{TF} = 30(2)$ μm.(c) Beam was intersecting the edge of the BEC, with the beam center aligned ~ 20 μm away from the center of the BEC.

spin, followed by a 2-s hold, allowing for some equilibration of the vortices. The blue-detuned beam height[1] was then ramped on from zero up to full strength over 500 ms and held at full strength in in the following way, before being ramped to zero again:

- **I(a)**. The Gaussian beam was linearly ramped on to a beam-height value of U_g, over 500 ms, to each value among a set of 9 beam-height values (defined below), and held for 250 ms before being ramped to zero over 500 ms. This represents a constant hold time, variable intensity test.

- **I(b)**. The Gaussian beam was ramped on to a subset of values U_g of the set of 9 values (defined below) over 500 ms, then held for a variable amount of time (defined below), before being ramped to zero over 500 ms. This was a variable hold time, constant intensity test.

Crucially, the cloud was expanded and imaged after 5 s of total hold time after the spin and equilibration time steps, in an effort to compensate for the natural decay of the lattice seen in Fig. 6.1. Thus, independent of any ramp and hold scheme regarding the blue-detuned beam, each image is taken at the same time

[1]The term "beam height" refers to the peak repulsive potential height resulting from the light-atom interaction (Eq. 2.1), calculated using the optical intensity at the center of the blue-detuned focused spot.

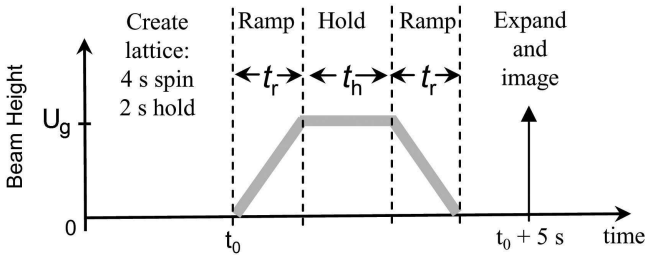

Figure 6.4: The timing sequence for investigating the spin down of the a lattice due to the Gaussian beam. A lattice was formed by spinning the cloud for 4 s, and letting it equilibrate for 2 s. The beam was ramped on over $t_r = 500$ ms and then either held to different beam heights U_g (see text) for a fixed time of $t_h = 250$ ms (case **I(a)**), or held for a variable time t_h (case **I(b)**). The beam height was then ramped to zero over $t_r = 500$ ms, and any additional hold time was added such that 5 s of total hold time elapsed after the formation of the lattice. The BEC was then expanded and imaged using near resonant absorption imaging.

step, allowing for comparison between the various blue-detuned beam ramp-and-hold schemes. The set of beam powers corresponding to case **I(a)** were: P_{tot} =(4, 14, 24, 34, 53, 73, 93, 113, 135) μW. Assuming a Gaussian beam profile, one can calculate the on-axis beam intensity from the following formula: $I_0 = \frac{2*P_{tot}}{\pi w_0^2}$, where $w_0 = 8(2)$ μm was the measured beam waist at focus. Referring to Eq. 2.1, the beam heights U_g, given in units of $\hbar\omega_r$, with $\omega_r = 2\pi \times 7.8$ Hz, were calculated to be U_g =(8, 31, 52, 73, 116, 159, 204, 246, 295) $\hbar\omega_r$. For case **I(b)**, a subset of three beam power values was chosen: (4, 14, 24) μW, corresponding to $U_g = (8, 31, 52)$ $\hbar\omega_r$. The hold times for case **I(b)** were t_h =(0, 0.25, 0.5, 0.75, 1, 2, 3, 4) s.

For each implementation of a ramp scheme, the resulting vortex observations were tallied over ∼10 runs of the experiment, generating an average vortex observation statistic for each hold time t_h and beam height U_g. Due to fluctuations in the initial lattices day-to-day, data points were normalized to the average initial number of vortices for each set of runs, in practice $\sim 15 - 25$ vortices[2]. Thus, resulting plots of the aggregate data (as seen in Fig. 6.5, for example), taken from multiple days of data runs, each start at a value of 1. In order to compare the various ramp schemes, resulting average vortex observation statistics were plotted vs. a product

[2]The source of day-to-day fluctuations in vortex numbers was not determined.

of the beam height $U(t)$ and the time since the beam was turned on (essentially the area under the curve seen in Fig. 6.4). The resulting metric is thus a *beam-height-time product*, where the area is in units of $\hbar\omega_r \cdot$ sec. Vortex observation results are plotted against this metric, rather than a metric such as the final beam height, as it provided a consistent way of comparing the resulting data points from the set of blue-detuned ramp schemes.

The results for case **I(a)** are shown in Fig. 6.5. The following function was used to fit the data:

$$f(\beta_g) = (1 - \eta_0)e^{-\beta_g/\gamma} + \eta_0, \tag{6.4}$$

where η_0 is some offset normalized vortex number, γ is a decay constant, and β_g is a variable with units of $\hbar\omega_r \cdot$ s. We define β_g as $\beta_g = \int dt\, U(t)$, so that β_g is the integrated beam-height and time product (i.e. the area under the curve shown in Fig. 6.4). This definition includes the ramp on and off of the beam. With the beam aligned 7 μm off of the center of the BEC, the fit gave $\gamma = 55(17)\ \hbar\omega_r \cdot$ s, with an offset of $\eta_0 = 0.39(0.07)$. For the condition with the beam aligned at approximately half of the Thomas-Fermi radius, the fit gave $\gamma = 26(5)\ \hbar\omega_r \cdot$ s, with an offset of $\eta_0 = 0.24(0.03)$. With the beam intersecting the edge of the BEC, the fit gave $\gamma = 25(5)\ \hbar\omega_r \cdot$ s, with an offset of $\eta_0 = 0.06(0.04)$.

For case **I(b)**, data points were taken with the beam aligned at approximately half of the Thomas-Fermi radius for three values of the beam height, $U_g = (8, 31, 52)$ $\hbar\omega_r$, and hold times $t_h = (0, 0.25, 0.5, 0.75, 1, 2, 3, 4)$ s. The vortex observation results are shown in Fig. 6.6(a,b,c). Fig. 6.6(d) combines all the data onto one plot and fits the following function to the curve

$$f(\beta_g) = e^{-\beta_g/\gamma}. \tag{6.5}$$

Fitting only the data corresponding to the 24 μW case, Fig. 6.6(c), yields $\gamma = 31.8(2.5)\hbar\omega_r \cdot$ s. Fitting the combined data from Fig. 6.6(a,b,c) yields $\gamma = 31.4(1.3)\hbar\omega_r \cdot$ s. It is worth noting that these decay constants, corresponding to a case in which the *hold time* was varied, are similar to the decay constant $\gamma = 26(5)$ $\hbar\omega_r \cdot$ s from fitting the curve in Fig. 6.5(b), where the *intensity* was varied. The

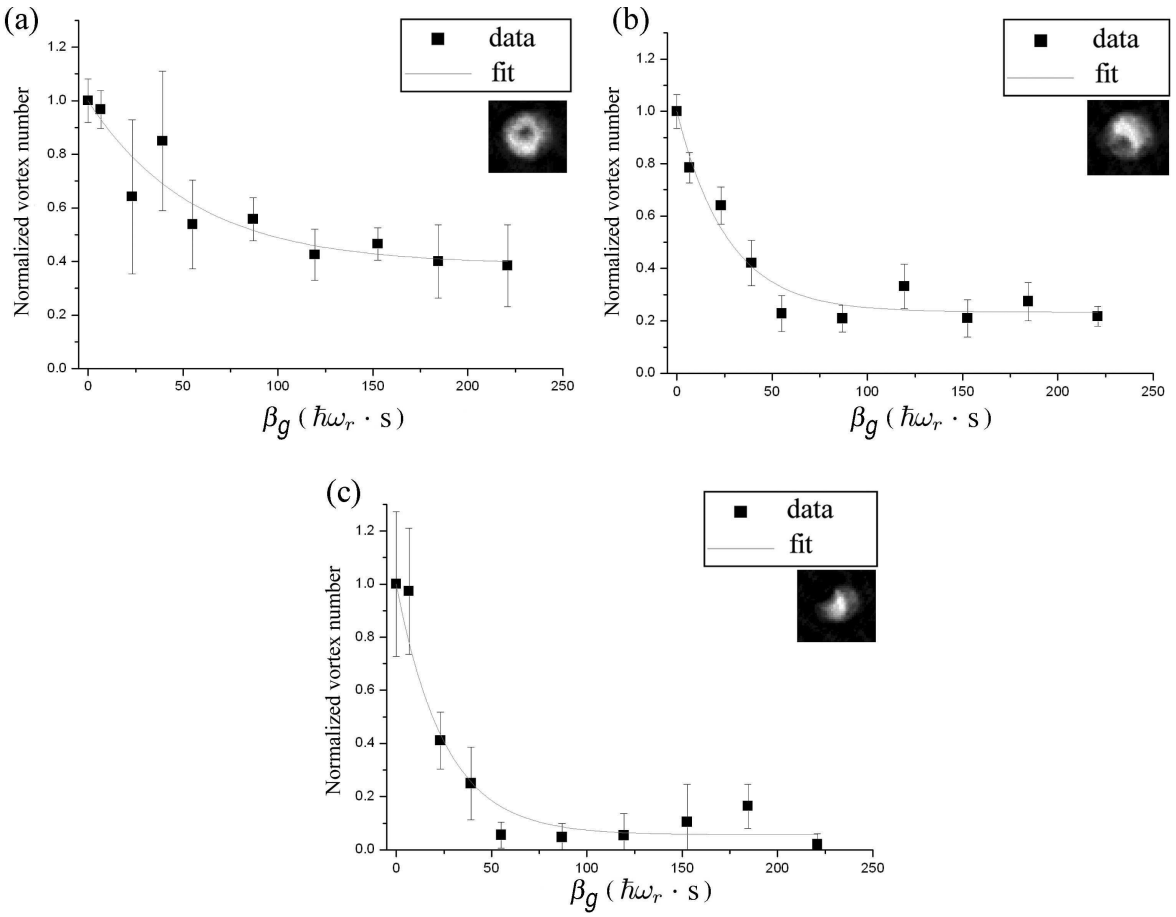

Figure 6.5: Damping results for the Gaussian beam, aligned at the three positions shown inset in the figure, normalized to the initial number of vortices. Results are plotted against the beam-height-time product β_g. Error bars on the plot represent the standard deviation of the data points over the ~ 10 runs of the experiment per data point. (a) Vortex observation results with the beam aligned just off center of the BEC. The resulting fit gives a time constant of $\gamma = 55(17)\ \hbar\omega_r \cdot \mathrm{s}$, with an offset of $\eta_0 = 0.39(0.07)$ (see text). (b) Vortex observation results with the beam aligned at approximately half the Thomas-Fermi radius. The resulting fit gives a time constant of $\gamma = 26(5)\ \hbar\omega_r \cdot \mathrm{s}$, with an offset of $\eta_0 = 0.24(0.03)$. (c) Vortex observation results with the beam intersecting the edge of the BEC. The resulting fit gives a time constant of $\gamma = 25(5)\ \hbar\omega_r \cdot \mathrm{s}$, with an offset of $\eta_0 = 0.06(0.04)$.

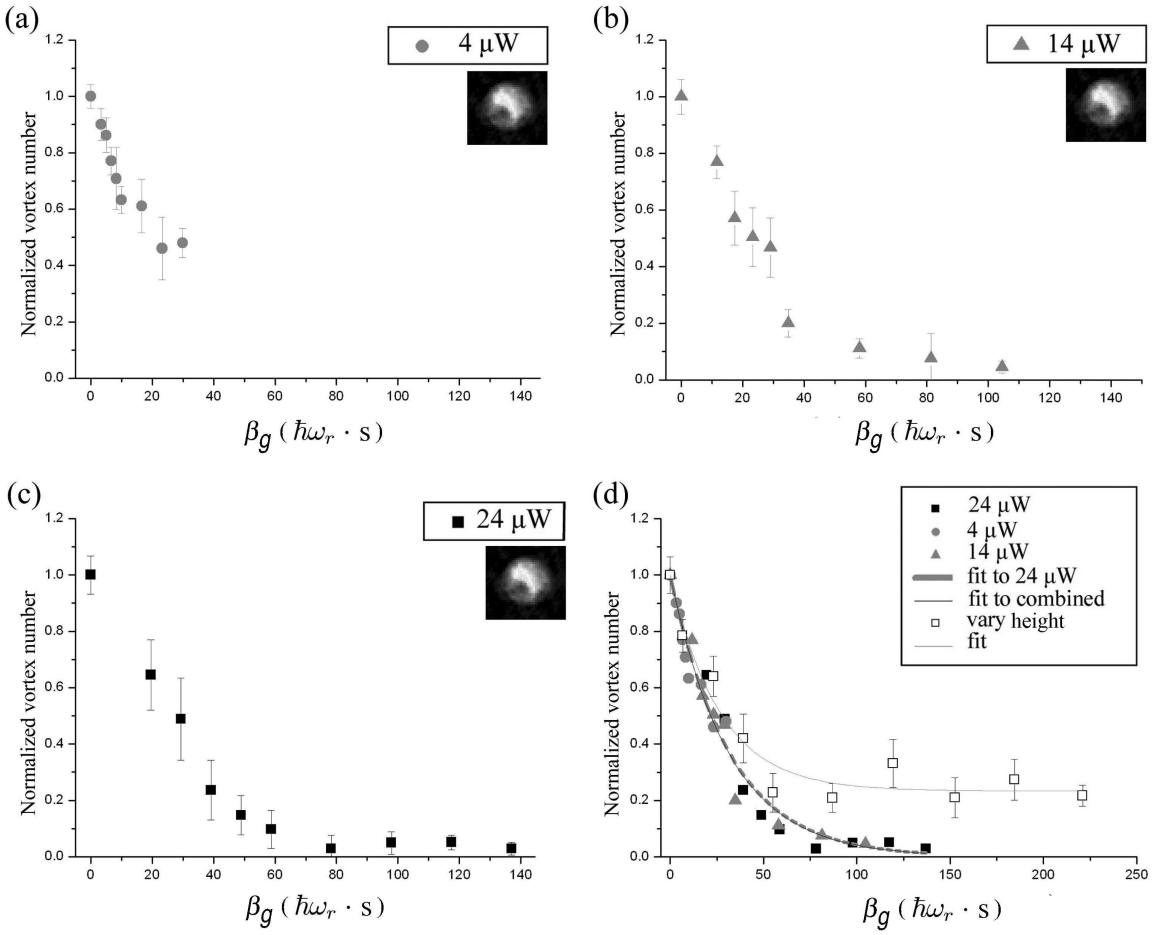

Figure 6.6: Damping results for the Gaussian beam, aligned at half the Thomas-Fermi radius, normalized to the initial number of vortices. Results are plotted against the beam-height-time product. Error bars on the plot represent the standard deviation of the data points over the ~ 10 runs of the experiment per data point. (a,b,c) Damping as a result of a fixed (4,14,24) μW total beam power respectively, and varied hold time. (d) The results of fitting the curve for 24 μW, shown with a grey dashed line, yielding $\gamma = 31.8(2.5)\hbar\omega_r \cdot$s and the combined data from (a), (b), (c) (black solid line), yielding $\gamma = 31.4(1.3)\hbar\omega_r \cdot$ s. Data points from Fig. 6.5(b), where the final beam height was varied, are also shown with open boxes.

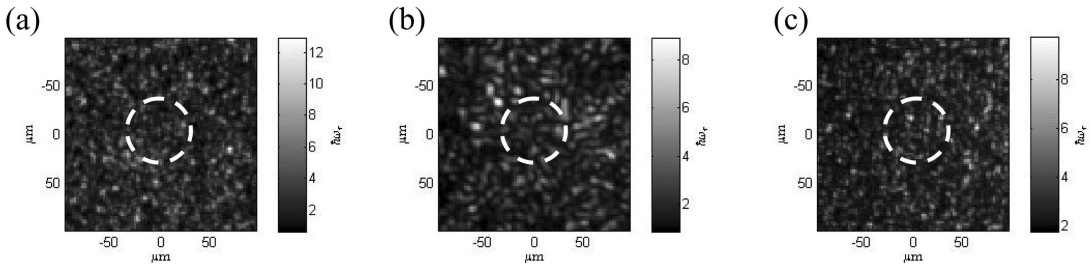

Figure 6.7: Speckle images, centered on the BEC position, for a typical beam intensity used in the experiment. Overlaid on the plots is the approximate Thomas-Fermi diameter of the condensate. (a)Blue-detuned speckle. (b) Red-detuned speckle. (c) Red-detuned speckle, but with a smaller spatial scale than (b).

beam position is the same for both cases, thus, comparison of these sets of data suggest that the potential-time product we have defined as β_g is in fact the significant figure of merit in determining the amount of damping in the system. Further discussion of this metric will be included at the end of this chapter.

6.4 Lattice damping with speckle

The generic optical system shown in Fig. 6.2 was used to image a ground glass diffuser on to the BEC, resulting in a speckle pattern at the BEC location. For blue-detuned speckle at a wavelength of 660 nm, a 10° diffraction angle ground glass diffuser was used, and two 75 mm lenses were used in the collimated imaging system. The resulting speckle pattern is shown in Fig. 6.7(a). Red-detuned speckle was also utilized, using 1090-nm light. Here, an extra 50-mm lens was inserted in to the system, approximately 45 mm to the right of the ground glass plate in Fig. 6.2(b); this lens served to approximately focus the input 2-mm radius collimated beam, onto a 25° ground glass diffuser. The plate was then imaged with a 50-mm lens followed by a 110-mm lens. Since the resulting system has a magnification of ∼2X, and the light has longer wavelength (1090 nm), the resulting speckle pattern was larger grained than in the blue-detuned case and is shown in Fig. 6.7(b). Smaller grained red-detuned speckle was also utilized using an imaging system the same as that used in the blue-detuned case; an image is shown in Fig. 6.7(c).

Similar to the Gaussian beam, the input blue-detuned beam to the ground-glass plate was ramped on to various intensities and held for various times before being ramped off. However, unlike the Gaussian beam scheme, the ramp time was not held constant; instead for each of the three speckle fields, a constant ramp slope dU_d/dt (see below) was respectively maintained for each case. A diagram of the timing sequence is given in Fig. 6.8. Thus, for larger final input beam intensities, the ramp took longer to reach maximum intensity. Prior to the application of the speckle, as in the Gaussian beam case, a 4-s spin was followed by a hold, in this case 3 s, allowing a vortex lattice with ~ 20 vortices to form. The speckle pattern was then ramped on, held, and ramped off, and any additional hold was implemented such that all images was taken after a total of 2 s of hold after establishing the lattice. Three specific ramp schemes were investigated:

- **II(a)** The beam incident on the ground-glass plate was ramped to various intensities, resulting in various "disorder strengths" $U_{d,max}$ (defined below), with each ramp maintaining the same slope.

- **II(b)** Using the same slope and ramps as in case **II(a)**, an additional 250 ms hold was added before ramping the beam off.

- **II(c)** Using the same slope as in case **II(a)**, one specific disorder strength $U_{d,max}$ was chosen from case **II(a)**, and the hold time was varied.

Following [155], the speckle pattern was characterized by taking the standard deviation over an ~ 200-μm-square box, centered at the BEC position, characterizing a "disorder strength," given here in units of $\hbar\omega_r$. The standard deviation was taken on a pixel-by-pixel basis, and the disorder strength U_d is defined as:

$$U_d = \sqrt{\frac{1}{N}\sum_{i=1}^{N}(U_i - \overline{U})^2}, \tag{6.6}$$

where N is equal to the total number of pixels, U_i the value of the ith pixel given in units of $\hbar\omega_r$, and $\overline{U}$ is the mean potential energy over the 200-μm-square box. Although the speckle pattern has an overall approximately Gaussian envelope (due

to the initial Gaussian input beam), the $1/e^2$ width of the pattern was on the order of 900 μm for the blue-detuned speckle; thus the intensity over the 200 μm-square box is fairly constant. For the blue-detuned speckle, the resulting set of disorder strengths for case **II(a)** were $U_{d,max}$ = (0.17, 0.40, 0.63, 0.87, 0.96, 1.11, 1.21, 1.35, 1.44, 1.54, 1.73) $\hbar\omega_r$. In ramping on and off the beam incident on the ground-glass plate, the slope was set to match a 500-ms ramp to $U_{d,max}$ = 1.35 $\hbar\omega_r$, or dU_d/dt = 2.7 $\hbar\omega_r$/s, resulting in corresponding ramp times of t_r = (83, 167, 250, 333, 367, 417, 450, 533, 567, 633) ms. For case **II(b)**, a subset of disorder strengths were used, since with the addition of a 250-ms hold, some of the resulting total ramp and hold times would have exceeded 2 s. The subset used was $U_{d,max}$ = (0.17, 0.63, 0.87, 0.96, 1.11, 1.21, 1.35) $\hbar\omega_r$. For case **II(c)**, a disorder strength of $U_{d,max}$ = 0.63 $\hbar\omega_r$ was used, with hold times t_h = (0, 0.1, 0.25, 0.5, 0.75, 1, 1.25, 1.5) s.

For the large-grained red-detuned speckle, the approximate Gaussian envelope of the speckle was on the order of 500 μm. The speckle is again characterized over a 200-μm-square box, and the set of disorder strengths used for ramp scheme **II(a)** were $U_{d,max}$ = (0.45, 0.65, 0.84, 1.05, 1.24, 1.45, 1.65) $\hbar\omega_r$. The slope for this speckle pattern was chosen to match that of a ramp to $U_{d,max}$ = 1.45 $\hbar\omega_r$ in 750 ms,

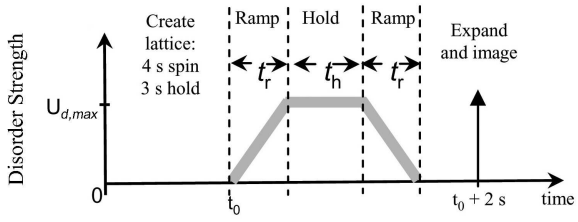

Figure 6.8: The timing sequence for investigating the spin-down of the vortex lattice due to speckle. A lattice was formed by spinning the cloud for 4 seconds, and letting it equilibrate for 3 seconds. The beam was ramped on over a variable time t_r resulting in disorder strength $U_{d,max}$ and then immediately ramped off (case **II(a)**), or held at the value $U_{d,max}$ for 250 ms (case **II(b)**), or held at a value $U_{d,max}$ for a variable time t_h (case **II(c)**). Since the slopes dU_d/dt were matched for all ramps for a given speckle pattern, ramps to higher values $U_{d,max}$ take longer to accomplish. After the ramp sequence, the cloud was held for any remaining time such that the image was taken after 2 s of total hold after establishing the lattice.

or $dU_d/dt = 1.93\ \hbar\omega_r$/s, resulting in the corresponding ramps: t_r = (214, 321, 428, 535, 642, 750, 857) ms. Again, for case **II(b)**, a subset of disorder strengths were used: $U_{d,max}$ = (0.45, 0.65, 0.84, 1.05, 1.24) $\hbar\omega_r$. For case **II(c)**, with variable hold times, a disorder strength of $U_{d,max} = 0.65\ \hbar\omega_r$ was used, with hold times t_h = (0, 0.1, 0.25, 0.5, 0.75, 1) s.

For the small-grained red-detuned speckle, the approximate Gaussian envelope of the speckle was on the order of 1000 μm. Characterizing the speckle over a 200-μm-square box, the set of disorder strengths used for ramp scheme **II(a)** were $U_{d,max}$ = (0.51, 0.56, 0.64, 0.69, 0.76, 0.89, 1.05) $\hbar\omega_r$. The slope for this speckle pattern was chosen to match that of a ramp to $U_{d,max} = 1.05\ \hbar\omega_r$ in 750 ms, or $dU_d/dt = 1.40\ \hbar\omega_r$/s, resulting in the corresponding ramps: t_r = (83, 167, 250, 333, 366, 417, 450, 500) ms. Again, for case **II(b)**, a subset of disorder strengths were used: $U_{d,max}$ = (0.51, 0.56, 0.64, 0.69, 0.76, 0.89) $\hbar\omega_r$. For case **II(c)**, with variable hold times, a disorder strength of $U_{d,max} = 0.51\ \hbar\omega_r$ was used, with hold times t_h = (0, 0.1, 0.175, 0.25, 0.5, 0.75) s.

The resulting vortex observation statistics for the three ramp schemes and three speckle patterns are shown in Fig. 6.9. The data points were plotted against the disorder-strength-time product, defined as $\beta_d = \int dt\, U_d(t)$, again integrated over ramp and hold times. Error bars represent the standard deviation over the experimental runs used to generate each point; here 3 runs of the experiment were averaged. Again, the simple exponential decay shown in Eq. 6.5 was used to fit the resulting data; here, the total data corresponding to cases **IIa**, **IIb**, and **IIc** for each speckle pattern were fitted. For the blue-detuned speckle, the fit to the data gives $\gamma = 0.53(0.04)\hbar\omega_r \cdot$ s. For the large-grained red-detuned speckle, the fit gives $\gamma = 0.57(0.04)\hbar\omega_r \cdot$ s, and for the small-grained red-detuned speckle, the fit gives $\gamma = 0.36(0.03)\hbar\omega_r \cdot$ s.

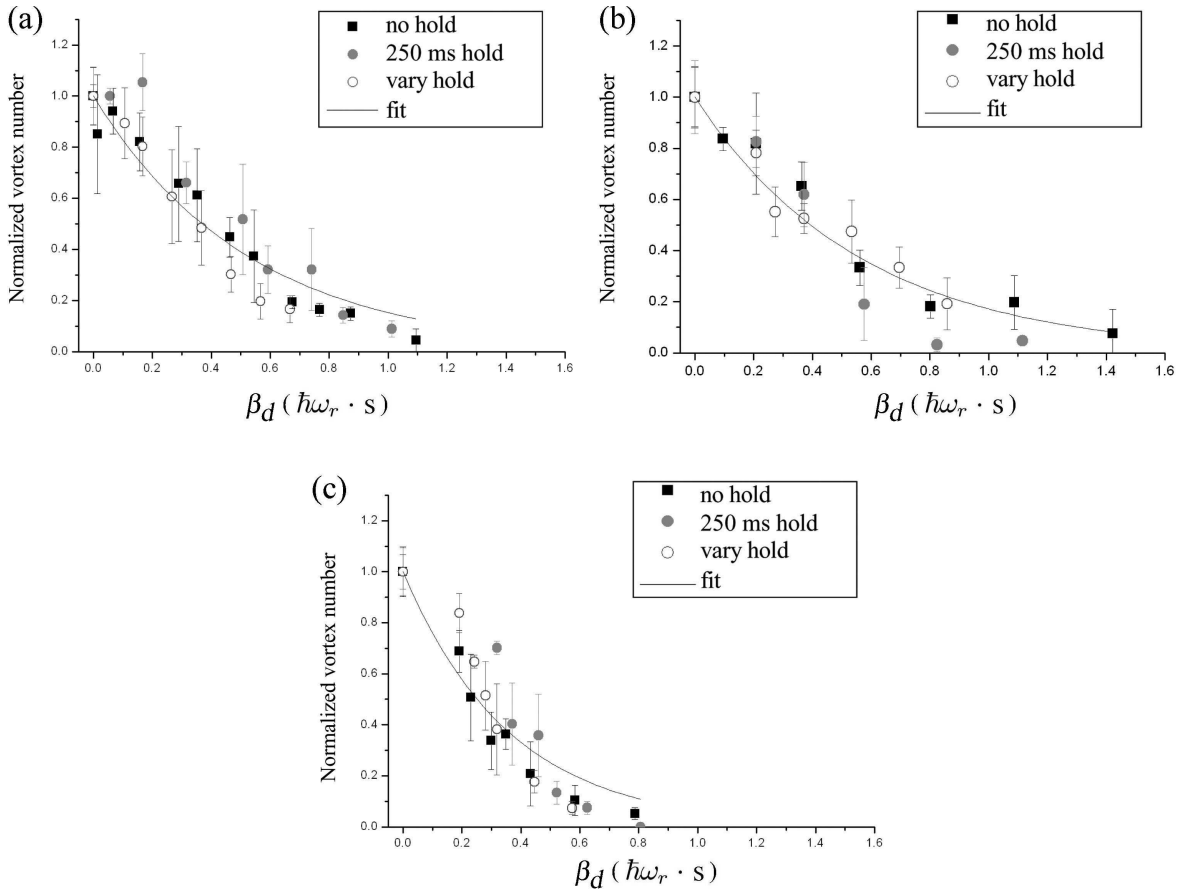

Figure 6.9: Damping results for speckle, normalized to the initial number of vortices; each point is averaged over 3 runs of the experiment and error bars represent the standard devation. Results are plotted against the disorder-strength-time product β_d. (a) Vortex observation results for the blue-detuned speckle. Data corresponding to cases **II(a)**, **II(b)**, and **II(c)** are combined on the plot. The resulting fit to the total data gives $\gamma = 0.53(0.04)\ \hbar\omega_r \cdot \mathrm{s}$ (see text). (b) Vortex observation results for the large-grained red-detuned speckle. The fit to the total data gives a decay constant of $\gamma = 0.57(0.04)\ \hbar\omega_r \cdot \mathrm{s}$. (c) Vortex observation results for the small-grained red-detuned speckle. The fit to the total data gives a decay constant of $\gamma = 0.36(0.03)\ \hbar\omega_r \cdot \mathrm{s}$.

6.5 Qualitative comparisons with theory

Initial numerical investigations by Law, Kevrekidis, and Carretero-Gonzáles have provided some qualitative comparisons to these experiments. The simulations implement a 2-D GPE solver, and represent simulations at zero temperature. Starting with a lattice of ∼20 vortices, a Gaussian beam was introduced with a beam height of approximately 96 $\hbar\omega_r$ and aligned at half of the Thomas-Fermi radius. After 5 s of damping, many vortices have left the cloud, and a disordered, non-lattice arrangement of vortices and corresponding phase was seen, as in Fig. 6.10(a,b). Such disordered arrangements of vortices were also seen in the experiment, as in Fig. 6.10(c), shown here for qualitative comparison only. The 3 experimental runs, each taken under identical conditions, correspond to a beam peak height of 8 $\hbar\omega_r$, centered $\sim$ 14 μm away from the BEC center (approximately half the TF radius), held on for 4 s, and expanded immediately after ramping the beam off. The beam height used in the experiment is much lower than that used in the numerical example. Further numerical studies will provide for more quantitative comparisons. In general, though damping is seen in the numerics, it is as yet unclear whether damping takes place at similar time-scales and beam heights as in the experiment.

6.6 Discussion of results

The introduction of gradual asymmetry into the trap results in the loss of vortices for both the single displaced Gaussian beam, and red and blue-detuned speckle, in accordance with expectations. Comparison between the damping with a Gaussian beam and speckle requires a consistent metric to be utilized in characterizing the potential. However, though easily assigned in the case of a Gaussian beam, using the peak intensity of the beam to calculate a beam height, the random and distributed nature of the speckle intensity field makes it more difficult to pick such a metric. The use of the standard deviation of the speckle pattern to characterize the disorder strength is used here, as is consistent with the literature [155], but makes for difficult comparison with the Gaussian beam. The use of this metric suggests that the

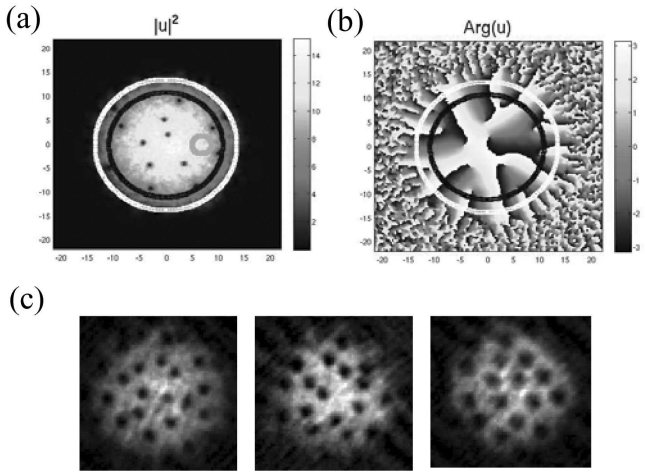

Figure 6.10: Qualitative comparisons between experiment and theory. (a) Density profile a cloud, generated with 2-D GPE simulations, showing a disordered set of vortices after 5 seconds of exposure to a Gaussian beam at height $\sim 96\ \hbar\omega_r$) and aligned at half the TF radius, and (b), the corresponding phase profile. The circles included on the image designate regions in which to count vortices; the initial condition for this run was a lattice of (20,14) vortices within the (white, black) circles respectively. The final condition shown here contains (14,11) vortices. (c) Shown for qualitative purposes only, 3 experimental runs, each of the 3 taken under identical conditions, corresponding to a beam height of 8 $\hbar\omega_r$, aligned at approximately half the TF radius, held on for 4 s, and expanded immediately after ramping the beam off. In the experiment, strong beams such as that used in the numerical simulations led to a near complete damping of vortices if the beam was held on to near the imaging time ($t_h = 4$ s in case **I(b)**). A weak beam is thus used here for qualitative comparison with the numerical simulations, as the weak beam allowed many vortices to remain in the system, allowing the arrangement of the vortex cores to be observed. The disordered arrangement of vortices is qualitatively similar to the numerical simulations, despite the difference in vortex number and large difference in beam intensity.

damping rate due to speckle is much higher than the rate due to a Gaussian beam, for a given potential height, U_g or $U_{d,max}$, as may be seen through examination of Fig. 6.5 and Fig. 6.9, for example. The physical implication of this comparison, given a somewhat inconsistent metric between the two situations, is unclear. There is some indication when comparing the damping rate for the Gaussian beam near the center of the cloud, with the damping rate for a beam at the edge of the cloud, which suggest that the rate of angular momentum loss is faster when the beam is at the edge of the cloud. This may significant, as a vortex lattice rotates similar to a solid body relative to the lab frame [11], implying that the fastest rate of fluid flow relative to a Gaussian beam or speckle pattern (fixed in the lab frame) would occur at the edge of the BEC. Since the speckle pattern fills the image plane, and the full area of the BEC, edge effects may be most important. Further work, including utilizing numerical simulations of the experiment, will ideally allow for more direct comparisons between the damping rate due to speckle versus a single Gaussian beam.

Perhaps the most significant aspect of the experiment is the importance of the beam-height-time product β_g or the disorder-strength-time product β_d as figures of merit in determining the loss of angular momentum from the system. Since the chemical potential of the cloud is estimated to be $\sim 48\hbar\omega_r$, and Gaussian beam heights on the order of $8\hbar\omega_r$ led to significant damping for the case of the Gaussian beam, it appears that small defects can have a significant damping effect, assuming the beam is held on for a long enough time. Similar effects were seen with the speckle pattern for low disorder strengths.

A significant deviation from this behavior is seen in Fig. 6.5, where the offset η_0 is seen. These data points were obtained by varying the intensity of the beam, but keeping a *fixed* hold time of 250 ms. The leveling of the curve indicates a departure from damping dependent on the beam-height-time product. For the purpose of discussion, we can imagine a Gaussian beam with a peak potential height just over the chemical potential of the BEC. This beam will fully penetrate the cloud, forming a hole. Such a precise beam height was not utilized in the experiment; however, if

plotted on Fig. 6.5, the point would lie at a value of $\sim 36\hbar\omega_r \cdot \mathrm{s}$. Thus, data points located to the right of this value correspond to beam conditions which fully penetrate the cloud. This value falls close to the decay constant γ values produced through fitting the data in the figure. Perhaps this behavior indicates a saturation of damping for a fixed interaction (hold) time as the Gaussian beam potential height nears the chemical potential, or at least a much larger decay constant, resulting in the apparent leveling of the decay curve near the value η_0. This hypothesis may be checked in numerical simulations or with further experimental studies.

CHAPTER 7

SPONTANEOUS VORTICES

7.1 Introduction

This chapter summarizes several experiments conducted in the lab studying the spontaneous formation of vortices in the BEC transition. First, a review of the spontaneous vortex formation mechanism is presented from a theoretical standpoint. A summary of an experiment that may be interpreted as model of the spontaneous vortex creation mechanism, where three independent BECs were interfered, is given next. An experiment concerning the first experimental observations of spontaneous vortices in BECs is discussed, and experimental progress on further study of spontaneous vortex formation in our BECs is described. The spontaneous vortex creation mechanism has been theoretically discussed in the context of superfluid turbulence [121, 156, 157]; the intermediate stages of non-equilibrium superfluid formation are characterized by the presence of a tangle of vortices and antivortices and their interactions. The resulting final states represent the evolution to quasi-equilibrium, and experimental study of these final states may give insight into vortex-antivortex annihilation and dynamics. Moreover, spontaneously formed vortices represent a fundamental source of extraneous vortices in each of the experiments described in this dissertation, with observation rates dependent on the specific experimental sequences.

7.2 BEC phase transition

Phase transitions are ubiquitous across diverse physical systems and occur at all energy scales, from the familiar phase transition of water to ice, for example, to the phase transitions that occurred in the early universe [158]. Physical systems

that are unrelated on a microscopic level can be organized into universality classes that exhibit similar physics during the phase transition. It is therefore helpful to broadly characterize dynamics of phase transitions, and how a system reaches an equilibrium state. The dynamics of the phase transition, especially when a system is out of equilibrium, present convenient experimental signatures for the study of spontaneous symmetry breaking through the formation of topological defects [159]. In a BEC, such defects manifest as topological structures such as vortices [79, 128] or solitons [160].

The process of spontaneous vortex formation in a BEC is related to the growth of correlations in the system as the gas passes through the condensate phase transition. A parameter denoted by ξ quantifies the length over which changes in the order parameter ψ may be accurately predicted. The Kibble-Zurek model [127, 158, 161] provides a prescription for calculating this correlation length ξ. The relaxation rate of the system $1/\tau$ quantifies an equilibration time of the system, where $\tau = \tau_0 k_B T/|\mu|$, where τ_0 is a phenomenological parameter, equal to the elastic collision time between particles, T the system temperature, and μ is the chemical potential. We assume the temperature decreases linearly with time; $T(t) = (1 - \frac{t}{\tau_Q})T_c$, where $1/\tau_Q$ characterizes the quench rate of the system and is τ_Q known as the quench time. The quench rate may be appropriately thought of as a cooling rate for a thermodynamic phase transition. The quench rate $1/\tau_Q$ is not necessarily equal to $1/\tau$, and in particular, if $1/\tau_Q < 1/\tau$, the system falls out of equilibrium and the correlation length ξ is frozen at [128]

$$\xi = \lambda_{T_c}(\tau_c/\tau)^{1/4}. \tag{7.1}$$

Here, λ_{T_c} is the thermal deBroglie wavelength at the critical temperature T_c. Descriptions of the parameters λ_{T_c} and T_c may be found in Ref. [4]. The freezing-in of this characteristic length scale is especially significant if ξ is smaller than the harmonic-oscillator length of a harmonically trapped BEC, the characteristic length scale describing the size of the BEC for low atom numbers. The transition process may be then characterized by the formation of independent phase-uncorrelated

regions of characteristic size ξ, and this mis-match of length scales implies the existence of multiple uncorrelated regions, referred to here as "proto-condensates," within the emerging condensed region. The progressive interference of these regions may trap phase loops of 2π, as described in a model experiment in the subsequent section. Such a phase loop describes a quantized vortex, and the spatial density of these topological defects is shown in the Kibble-Zurek model to be proportional to $1/\xi^2$. Significantly, the density of defects is thus tied to the formation rate $1/\tau_Q$; in particular, for faster formation rates a higher density of defects is predicted. A schematic of the spontaneous vortex formation process is shown in Fig. 7.1.

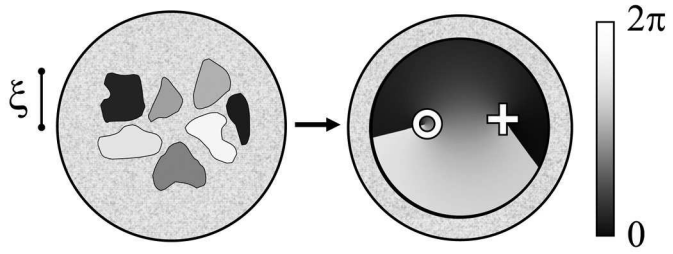

Figure 7.1: Schematic showing the vortex formation process. As the cloud experiences a quick quench, self-coherent regions of length scale ξ may form. Depending on the relative phase between adjacent regions, indicated by shades of gray, 2π phase windings may be present as the BEC continues to grow. These topological defects appear as vortex cores, with either sign (+/-) of circulation, denoted by the cross and circle. Figure taken from [79].

7.3 Vortex formation through merging independent BECs

Before discussing our work on spontaneous vortices, it is relevant to summarize an earlier experiment performed in the group: "Vortex formation by merging of multiple trapped Bose-Einstein condensates," published in Physical Review Letters on March 16, 2007 [71], and more fully discussed in David Scherer's PhD thesis [8]. A brief description of the experimental procedure is included below and the relevance to spontaneous vortex creation is noted.

7.3.1 BEC formation in a three-well potential

The experiment utilized a blue-detuned laser field to create a repulsive barrier. The 660-nm beam generating the barrier was directed along the axial direction of the trap, similar to previously described methods used to focus a Gaussian beam to the BEC position as in Fig. 2.5. Different in this experiment was the shape of the resulting potential: instead of a Gaussian focused spot, a "Y-shaped" barrier was imaged onto the trap position. By overlaying this potential with the $(\omega_r, \omega_z) = 2\pi \times (7.8, 15.3)$ Hz TOP trap (Section 2.3), the result was a potential with three local minima, as shown in Fig. 7.2. The barrier was ramped on over two seconds prior to BEC formation. With a final evaporative RF ramp over 10 seconds, 3 BECs were formed in the combined potential. Depending on the strength of the blue-detuned barrier, the three independent condensates would either combine as the BEC continued to grow as in Fig. 7.2(d), for a weak barrier, or remain separated as in Fig. 7.2(e), for a strong barrier.

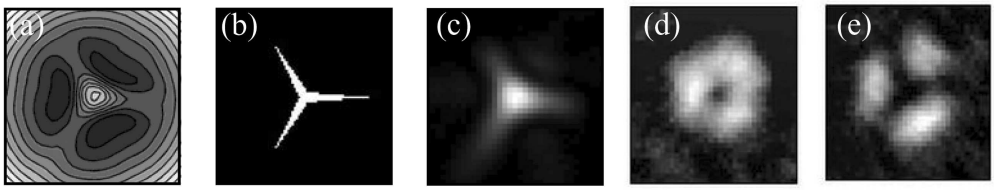

Figure 7.2: (a) Potential energy contours of the harmonic trap combined with a Y-shaped repulsive potential. (b) Binary mask used to create the Y-shaped beam, and (c) a CCD image of the resulting beam. (d,e) Phase-contrast images of the condensate, in-trap, viewed along the axial direction. In (d) a weak barrier was implemented with 45 μW of power in the beam. The image in (e) is representative of the strong barrier situation with 170 μW of power, yielding three condensates at the completion of evaporative cooling. Images are 85 μm-square. Adapted from [71].

7.3.2 Merging of independent BECs

The relative phases of the three clouds were initially indeterminate. Upon merging, any phase differences would lead to interference and most likely fluid flow[1]. Merging of the condensates was accomplished through two methods: either the condensates would merge together naturally as they continued to grow, for low-intensity barriers (weak-barrier regime), or they could be forcibly merged through ramp-down of the blue-detuned beam (strong-barrier regime).

Depending on the uncertain relative phases between the three condensates, a 2π phase gradient was theoretically calculated to occur with a probability of $P_v = 0.25$, in the limit of slow merging [162]. Since a 2π phase gradient corresponds to a quantized vortex, in the limit of slow merging we expected the formation of a single vortex; we emphasize that there is no explicit rotation or spinning added to the trap, instead, the vortex forms stochastically as a function of the random relative phases between adjacent condensates. For fast formation rates, interference fringes were predicted to occur, and the formation of multiple vortices was understood to be possible through the decay of interference fringes into vortices and antivortices.

Results obtained for various merging times τ in the strong-barrier regime are shown in Fig. 7.3. By varying the merging time, different vortex observation statistics were observed, and for slow merging times the results approached the expected value of $P_v = 0.25$. For faster merging rates greater numbers of vortices were observed. Vortices were also observed in the weak-barrier regime, with similar observation results. For additional details on this experiment, see Ref. [153].

7.3.3 Relevance to the Kibble-Zurek model

Seeing vortex formation as a result of the merging of independent condensates serves as a "3 proto-condensate" model of the Kibble-Zurek mechanism. The situation is considerably more complicated in the general Kibble-Zurek case, as the number of proto-condensates and merging time are not fixed or directly controllable quanti-

[1] fluid flow velocity $v \propto \nabla\phi$, see Eq. 1.2

ties. However, this experiment functions as a proof-of-principle, showing that vortex formation is possible when merging independent, phase-uncorrelated BECs.

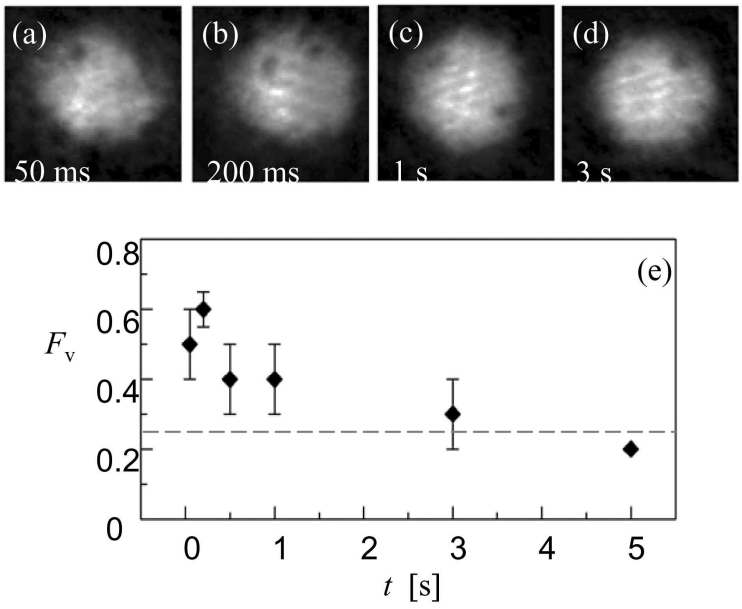

Figure 7.3: (a,b,c,d) Vortex observations for different merging times, corresponding to the strong-barrier regime; the barrier was ramped off over the time τ indicated. (e) By varying τ, the expected value of $P_v = 0.25$ is approached in the limit of slow merging ($P_v = 0.25$ is shown by the dashed line). Figure taken from [8]

7.4 Observation of spontaneous vortex cores in the BEC transition

This section summarizes a second experiment performed in the group: "Spontaneous vortices in the formation of Bose-Einstein condensates," published in *Nature* on October 16, 2008 [79]. Additional details may be found in Chad Weiler's PhD thesis [9]. This work served as motivation for our continued studies on spontaneous vortex formation.

7.4.1 Spontaneous vortex formation

As described above, for a fast quench one expects to see vortices spontaneously forming in the wake of condensation. For faster $1/\tau_Q$, which can be associated with

faster condensation, the number of defects observed (defect density) is expected to increase. We formed a BEC in the 2:1 harmonic trap, as described in Section 2.3. Two independent evaporative sequences were used to create BECs: a 6-s RF ramp (Quench A), and a sudden jump to a final RF value (Quench B). Following the methods of Ref. [128] the correlation length was estimated to be $\xi \approx 0.6$ μm. Since the radial harmonic oscillator length is $a_r \approx 3.8$ μm, we expected spontaneous vortex formation in our system. In calculating the quench time τ_Q, which was then used to estimate the correlation length, some uncertainty is present as the best experimental estimator of this parameter is unclear. We used the BEC formation time t_F, which we defined as the time elapsed between the first observation of a BEC component ($\sim 10\%$ of the final BEC number) and the time at which the BEC number reached $\sim 90\%$ of its final value. Fig. 7.4(a) shows the formation rate for the two RF evaporative schemes. Included on the plot is work done by Matthew Davis and Ashton Bradley at the University of Queensland[2] who simulated the experiment numerically using a finite-temperature model of the atomic system. Their data is represented by the solid lines in Fig. 7.4(a).

Examining figure Fig. 7.4(b), the probability of observing a single vortex is seen, derived from the numerical simulations. In order to measure vortex observation statistics in the experiment, we formed a BEC using one of the two evaporative RF schemes, expanded, and looked for the presence of vortex cores. By repeating the experiment many times, observation statistics were acquired. For Quench A, 23-28% of 90 runs contained at least one vortex, and for Quench B 15-20% of 98 runs showed at least one vortex. Examining Fig. 7.4(b), we see good agreement with the numerical results; experimental data windows and vortex observation statistics are represented by the grey boxes. The results agreed well with the numerics.

7.4.2 Spontaneous vortices in a toroidal trap

A toroidal trap was formed with the addition of a blue-detuned beam, propagating along the axial direction, similar to experiments described previously. This toroidal

[2]Ashton Bradley is currently at the University of Otago.

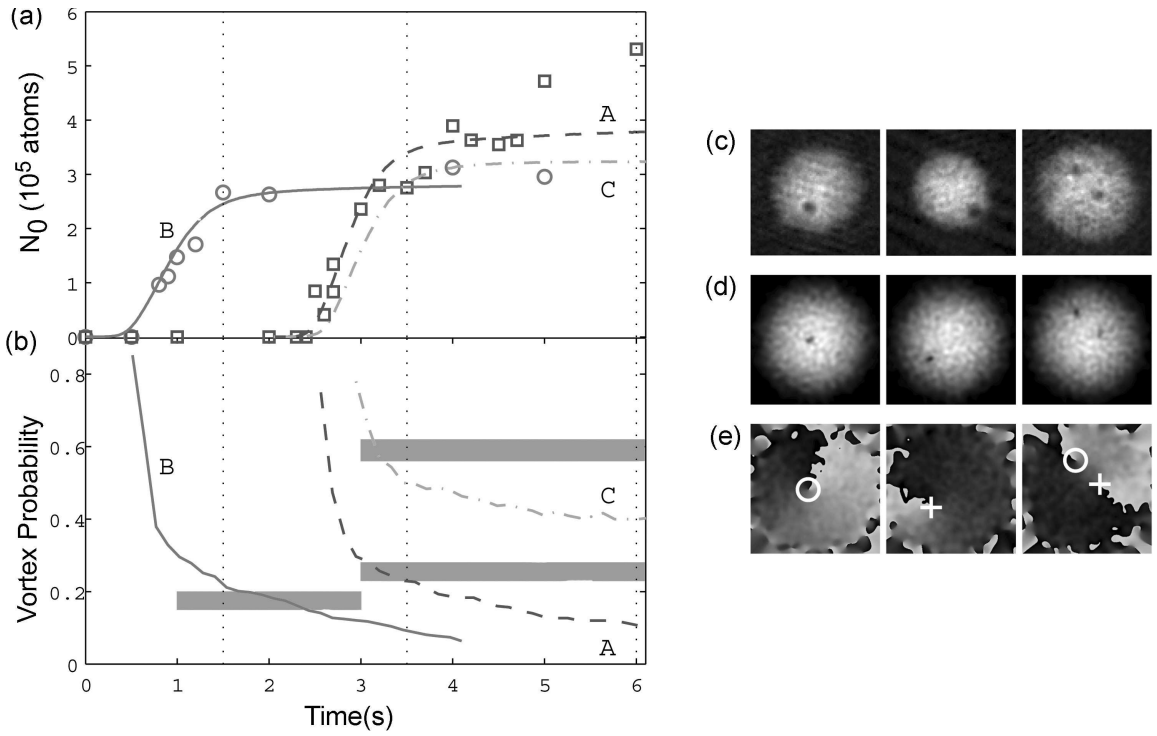

Figure 7.4: (a) Formation rates for the two RF schemes (A,B) and the toroidal trap (C, see text.) Experimental data is represented by the circles and boxes, the lines indicate numerical data. (b) Observation probability for a single vortex core as a function of time. Experiment data windows and vortex observation statistics are indicated by the grey boxes. (c) Expanded images of BECs showing the presence of spontaneous vortex cores, taken from the experiment. (d,e) Numerically derived data, showing the presence of vortex cores in simulated cloumn density and corresponding phase. Figure adapted from [79].

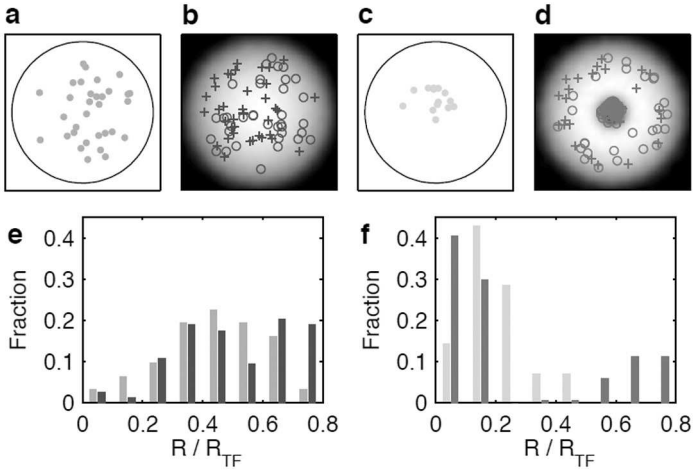

Figure 7.5: Vortex core pinning. (a, c), Representation of the experimentally measured positions R of all vortex cores relative to the Thomas-Fermi radius (R_{TF}) (outer circles) for (a), the harmonic trap and (c), the toroidal trap. (b, d), Corresponding theoretical results, crosses and circles indicate oppositely charged vortices. (e, f), Comparison of the statistics of the vortex locations, binned in steps of $0.1R_{TF}$, for the experimental data (left bars) and theoretical simulations (right bars). Harmonic trap results are shown in (e), toroidal trap results are shown in (f). For the experimental data, only images clearly showing a single core are considered. Caption and figure taken from [9].

trap was constructed without the addition of the red-detuned light sheet, hence the trap exhibits a ∼2:1 (radial:axial) BEC geometry. The blue-detuned laser beam had a 6-μm focused spot at the BEC location and was ramped on prior to BEC formation, as in the 3-well experiment. The final power in the beam was 18 μW, corresponding to a potential energy of $k_B \times 20$ nK. This may be compared to the chemical potential of the BEC, $\mu \approx k_B \times 20$ nK. The beam thus penetrates the cloud, producing a toroidal total potential.

Evaporation in this trap (quench C on Fig. 7.4(a)) led to the spontaneous creation of vortices, with $\sim$ 56-62% of runs containing at least one visible vortex core. This geometry, as discussed in Chapter 5, can lead to the pinning of vortices, inhibiting decay. The results seen experimentally and numerically provided evidence for the existence of pinned cores. After ramping the beam down and expanding for imaging, note was taken of the position of vortex cores within the expanded BEC

over the set of experimental and numerical runs. The aggregate of all data is seen in Fig. 7.5. When compared with the purely harmonic trap, grouping of vortices at the trap center is seen in both the experimental and numerical toroidal trap data. This implied the possibility of pinning of vortices during the BEC formation process.

7.5 New results: faster formation rates in a combined trap

A primary limitation of the experiments discussed so far was a limited formation rate. In particular, we hoped to obtain faster formation rates to look for the dependence of vortex observation statistics on BEC formation rate. After the completion of the first spontaneous vortex experiment, we implemented the 1090-nm beam for combined optical and magnetic traps (see Section 2.6). This section summarizes how we were able to utilize the combined optical and magnetic trap to condense more quickly and examine the resulting vortex statistics. Limitations of the work and directions for future experiments are discussed finally.

7.5.1 New method of evaporation

Typically, forced RF evaporative cooling was the primary method of evaporating in the combined optical and magnetic trap in order to produce BECs. However, the addition of the optical beam opens up several new possibilities for BEC formation. Since the atoms are confined vertically by the optical field, the quadrupole gradient B'_z may be changed with negligible shift of the vertical position of the combined trapping potential. Since the equilibrium sag position, given by Eq. 2.2, is sensitive to B'_z, the cloud will instead feel a net force due to an effective gradient as B'_z is changed. In effect, one side of the vertically confining potential is "tipped" as the equilibrium position shifts by ~ 0.25 mm towards the quadrupole origin. A diagram of this is shown in Fig. 7.6(a,b). This force can kick atoms out of the vertically confining beam, providing another evaporative mechanism. By combining this technique with a simultaneous RF ramp or jump, faster formation rates were possible. A list of the evaporative schemes used follows:

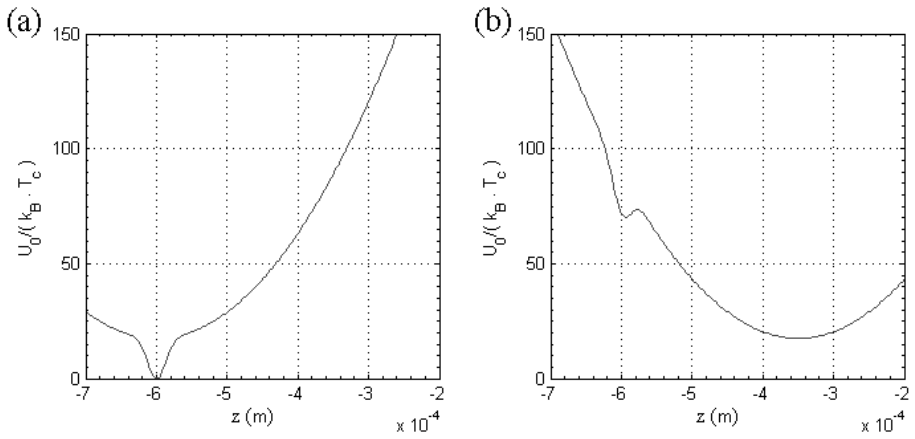

Figure 7.6: (a) Initially, the beam is aligned with the center of the magnetic field. (b) As the quadrupole gradient is shifted to a typical value of $B'_z = 60$ G/cm, the atoms continue to be held in place by the beam as the equilibrium position of the magnetic trap shifts by ~ 0.25 mm towards the quadrupole origin (z = 0 on plot). The vertical axis is scaled by $k_B \times T_c$, $T_c \sim 100$ nK is the critical temperature.

- **Evap. I**: fastest formation. After transferring a thermal cloud with $T \geq T_c$ to the combined optical and magnetic trap, evaporation was implemented by snapping the RF to a value of 3.9 MHz and implementing a 1-s ramp of the quadrupole gradient B'_z from 44 G/cm to 57 G/cm, with B_0 held at 3.41 G. In order to determine the formation rate, horizontal phase-contrast images of the BEC during the evaporative ramps were taken. The results from fitting the data are shown in Fig. 7.7. By examining the time scale over which the BEC number N_c rose from $\sim$10% to $\sim$90% of its final value, the formation time was estimated to be $t_F \approx 160(40)$ ms. As discussed earlier, it is not clear what to use for τ_Q, so we take this definition of t_F as τ_Q in comparing quench rates between the various evaporation schemes.

- **Evap. II**: moderately fast formation. The RF was ramped from 4 MHz to 3.9 MHz with an exponential ramp over 2 s; the exponential time constant was set to $\tau = 1\ s$. Again, the quadrupople gradient was shifted over the 2-s time interval; this time B'_z ramped from 44 G/cm to 60 G/cm. The results from fitting the transition data are shown in Fig. 7.8. The formation time for this

ramp was estimated as $t_F \approx 525(75)$ ms, again by estimating the time taken for N_c to rise from ∼10% to ∼90% of its final value.

- **Evap. III**: moderately slow formation. This formation scheme was performed with $B_0 = 3.41$ G and $B'_z = 44$ G/cm. A 6-s RF exponential ramp with $\tau = 2$ s from 4 MHz to 3.53 MHz was implemented. The results from fitting the transition data are shown in Fig. 7.9. The formation time for this ramp was estimated as $t_F \approx 1.30(0.1)$ s.

- **Evap. IV**: slowest formation. A 10-s $\tau = 5$ s exponential ramp was performed in the trap with $B_0 = 3.41$ G and $B'_z = 44$ G/cm. The results from fitting the transition data are shown in Fig. 7.9. The formation time for this ramp was estimated as $t_F \approx 2.6(0.2)$ s.

7.5.2 Spontaneous vortex formation in the combined trap

By expanding and looking for vortices, comparisons were made between the various formation schemes. Fig. 7.11 shows vortex formation results for **Evap. I** as a function of time from the beginning of the formation ramp, with each point an average of 35 separate runs of the experiment, taken over several days. The vortex statistics decay with time and the final state of the system is expected from theory to be a ground-state BEC with no vortices. An exponential fit to the data gives a time constant of $\tau = 2.5(0.5)$ s. Although the signal-to-noise ratio improves with hold time (as the evaporative ramp completes), the decay of vortices (most likely due to annihilation) implies that one should look as early as possible in the BEC formation to accurately count vortices. For fast formation rates with large numbers of vortices, under counting is thus a potential problem.

For **Evap. I**, looking as early as possible in the evaporation sequence, the highest overall spontaneous vortex observation statistic was seen. On a particular day of data runs, on average 4.8(0.1) vortices were observed over 29 runs of the experiment, with as many as 9 vortices visible in a few single runs of the experiment.

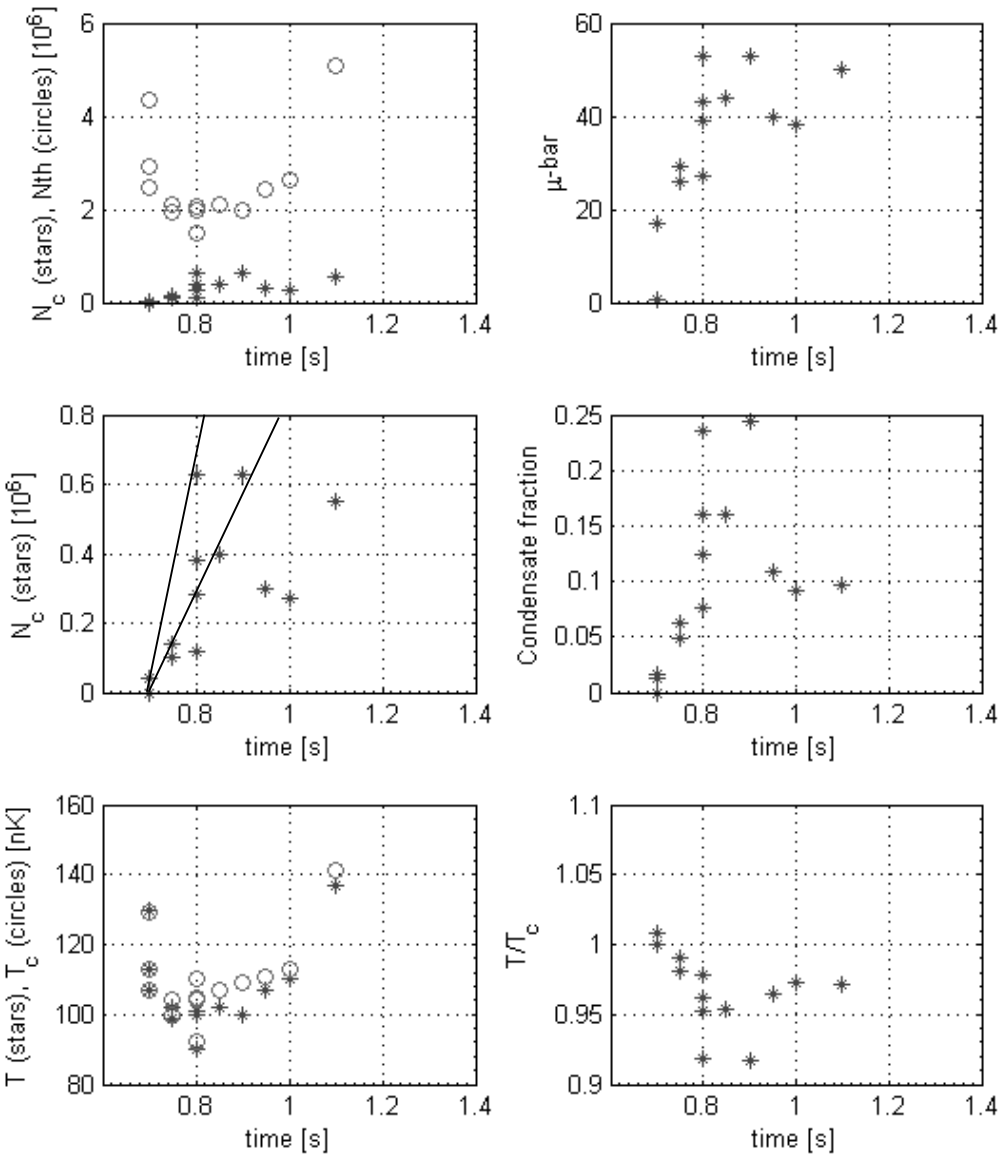

Figure 7.7: Results from fitting the transition data for **Evap. I**, the snap RF and 1-s B_z' ramp. The formation time was taken from the plot showing N_c, the condensed atom number. Given the large shot-to-shot fluctuations and fluctuations in the condensate size and number values, we estimated the formation time for the early part of this rapid cooling sequence as shown with the solid lines in the second plot of the first column. By examining the time scale over which N_c rose from ∼10% to ∼90%, the formation time was estimated to be $t_F \approx 160(40)$ ms. $\overline{\mu}$ (or μ-bar) is defined as $\mu/\hbar\omega_r$.

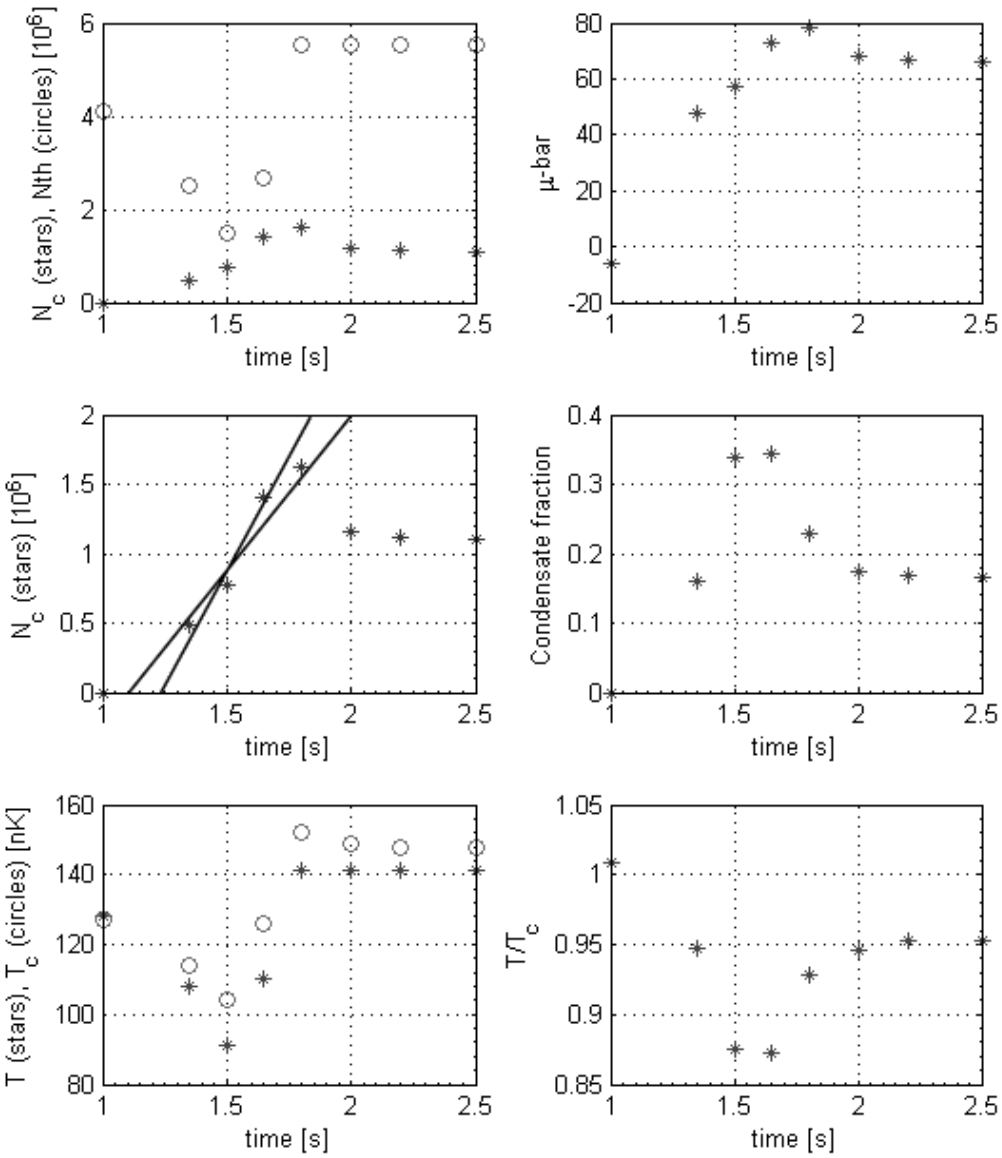

Figure 7.8: Results from fitting the transition data for **Evap. II**, the 2-s RF and B'_z ramp. As in Fig. 7.7, the formation time was taken from the plot showing N_c, the condensed atom number, and was estimated with the lines shown. By examining the time scale over which N_c rose from ∼10% to ∼90% of its final value, the formation time was estimated to be $t_F \approx 525(75)$ ms.

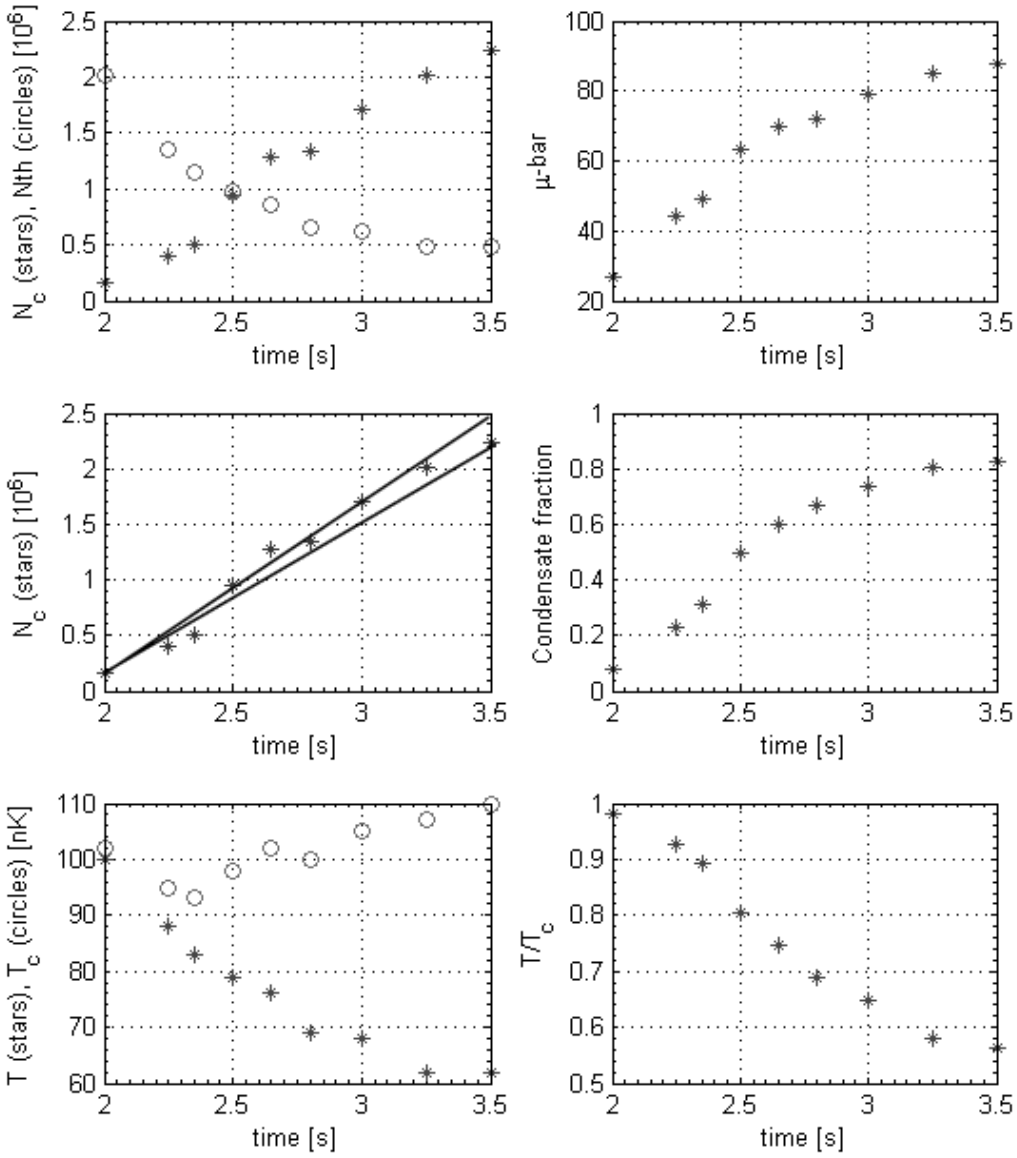

Figure 7.9: Results from fitting the transition data for **Evap. III**, the 6-second RF ramp, with B'_z held constant. As in Fig. 7.7 and Fig. 7.8 the formation time was estimated to be $t_F \approx 1.30(0.1)$ s.

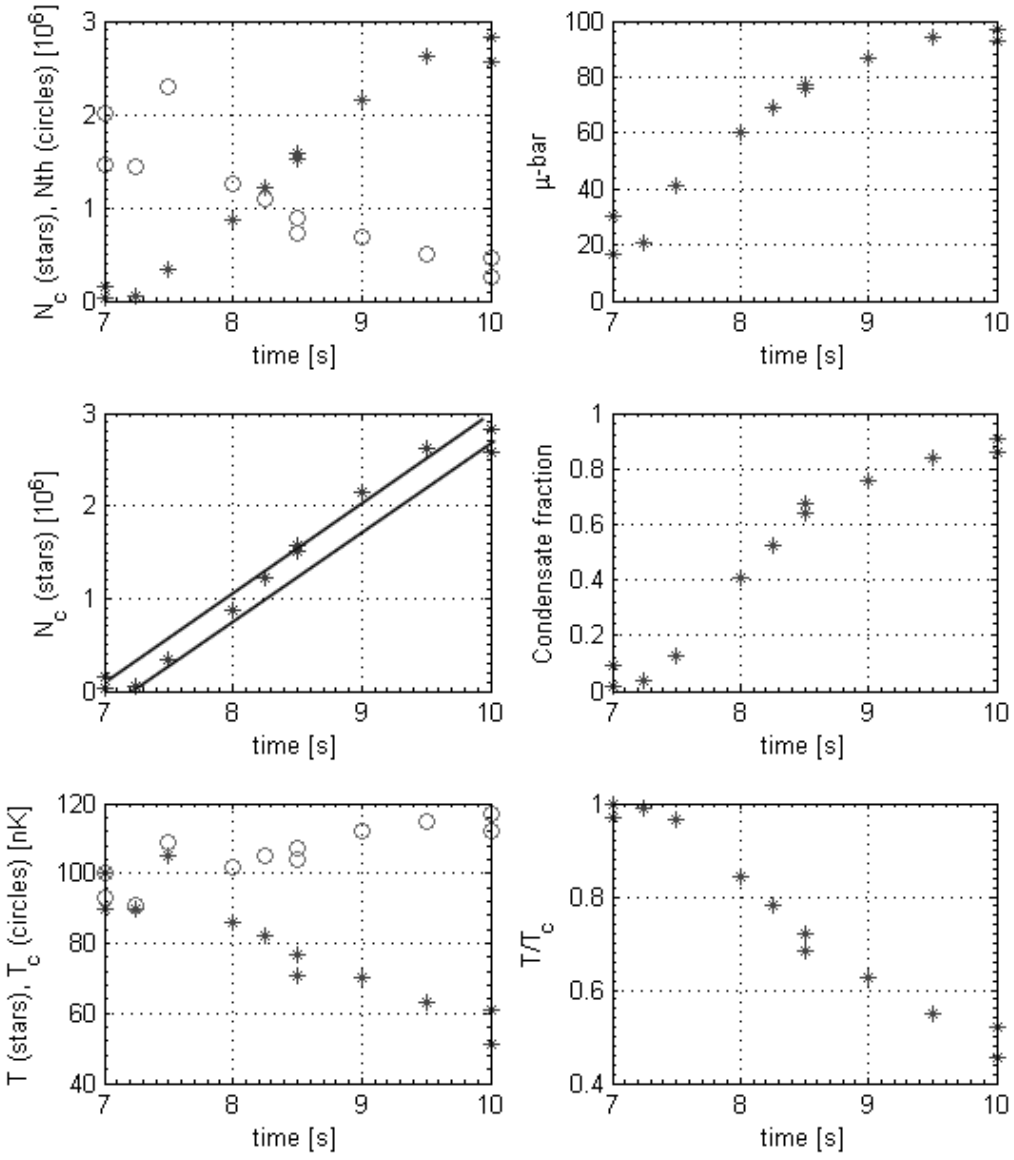

Figure 7.10: Results from fitting the transition data for **Evap. Scheme IV**, the 10-second RF ramp. As in Fig. 7.7-7.9, the formation time was determined as $t_F \approx 2.6(0.2)$ s.

This vortex observation statistic is considerably higher than was seen in the bare harmonic trap, where the observation static was ~ 0.23 vortices per cloud. Example images, showing the presence of multiple vortices, corresponding to **Evap. I** are inset in Fig. 7.12. The vortex observation statistics corresponding to **Evap. II**, **III**, and **IV** were 2.2(0.2), 1.4(0.1) and 0.6(0.1) vortices respectively.

As a caveat to this analysis of the data, note is taken of the complicated aspect of accurately counting the number of vortices seen in the cloud, primarily through the difficulty in selecting the time at which the signal-to-noise ratio was sufficiently high enough to reliably resolve vortices visually, further complicated by density fluctuations in the cloud. These non-ideal factors make positive identification of a vortex difficult, as can be inferred from the inset of Fig. 7.12.

With the ability to vary the formation time, hence τ_Q, and referring to Eq. 7.1, one would expect the defect (vortex) density to increase with decreasing formation time. In Fig. 7.11 and Fig. 7.12, one can see this behavior is manifest in the experimental data, confirming an important characteristic of the Kibble-Zurek model in this system. The expected defect density N_d predicted by the Kibble-Zurek model scales with the quench time τ_Q as $N_d \propto \tau_Q^{-1/2}$ [128]. Taking the $\log_{10}$ of both sides, one expects a plot of $\log_{10}(N_d)$ vs. $\log_{10}(\tau_Q)$ would exhibit a slope of $\gamma = -1/2$. A log-log plot of the data showing the average number of vortices vs. formation time is shown in Fig. 7.13, and a linear regression fit gives a slope of $\gamma_{fit} = -0.71(0.09)$. Also plotted is the expected slope of $\gamma = -1/2$. However, the final BECs obtained in each evaporative ramp differed in the final BEC size (volume), with the fastest ramp (**Evap. I**) producing the smallest BEC. In order to account for the different final BEC volumes, the radius of each cloud was measured, giving $r \sim 32$ μm for **Evap. I**, $r \sim 35$ μm for **Evap. II**, and $r \sim 44$ μm for **Evap. III** and **Evap. IV**. An approximate normalized average vortex number can be obtained by multiplying the average number obtained for **Evap. (I, II)** by (1.8, 1.4) respectively. The results are plotted in Fig. 7.14. A fit to this slope yields $\gamma_{fit} = -0.94(0.05)$, with relatively more narrow 90% confidence bands when compared with Fig. 7.13.

Although the -1/2 slope lies within the confidence bars of the fit in Fig. 7.13,

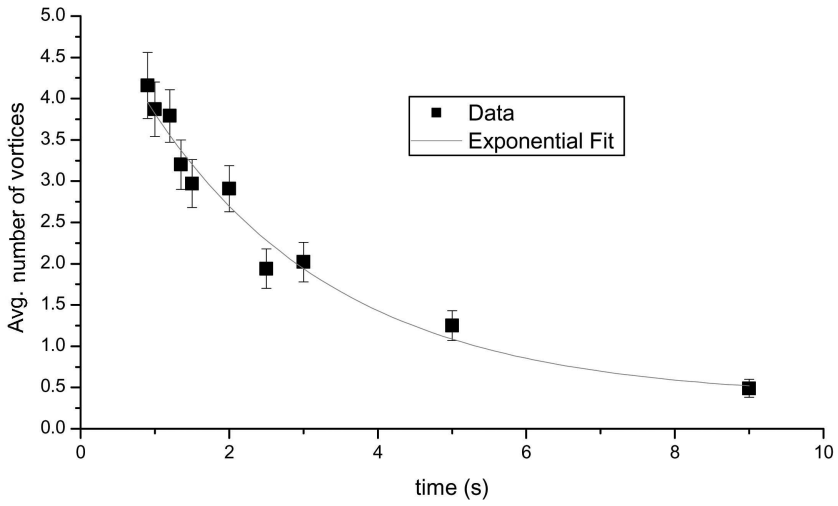

Figure 7.11: The decay of vortex observation statistics corresponding to the fastest formation rate is shown, averaged over several days of data runs. Each point represents the average of 35 runs of the experiment. Here, t=0 is defined as the start of the final RF evaporative ramp. An exponential fit to the data gives a time constant of $\tau = 2.5(0.5)$ s.

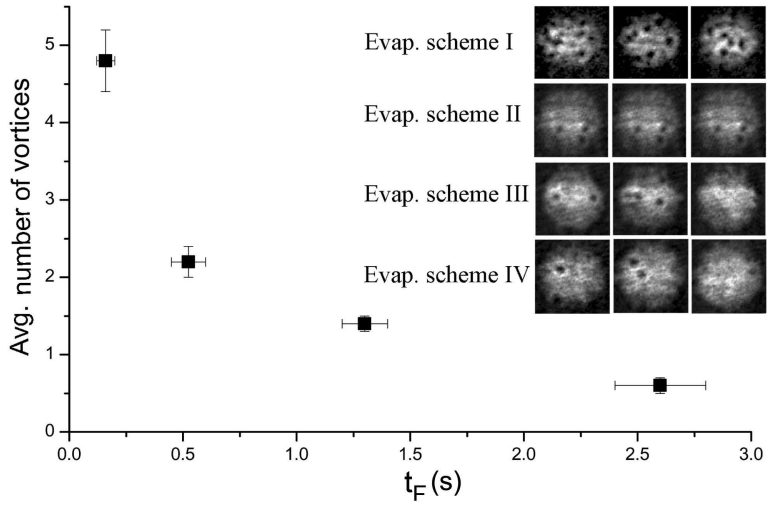

Figure 7.12: Spontaneous vortex observations as a function of formation time. The error bars for the average number of vortices are statistical in nature, and data points represent the average number of vortices seen over a single day of data runs (with ∼29-100 runs of the experiment for each data point). The error bars for the formation time were estimated from the plotted formation data. (inset) Example images in expansion of multiple spontaneously formed vortices for each formation scheme.

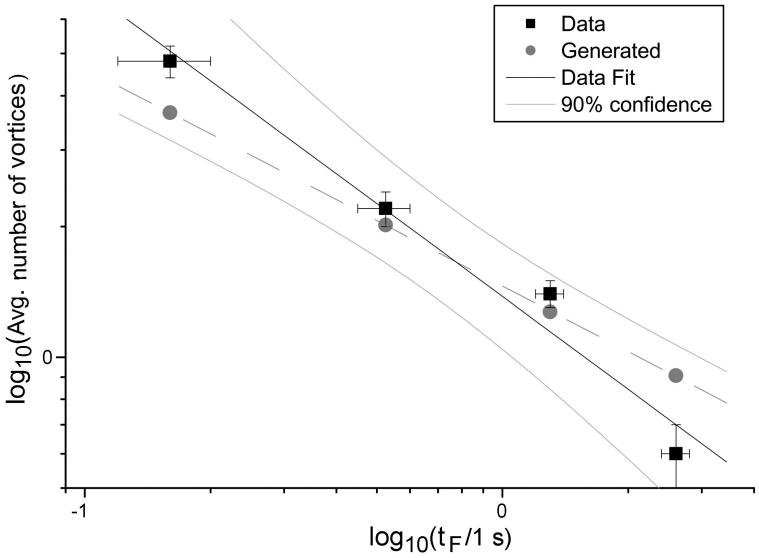

Figure 7.13: Average vortex observations for the 4 different formation times are plotted. A linear regression fit to the data (black squares)was performed in order to compare with [159], giving a slope $-0.71(0.09)$. Additional points (gray circles) illustrate what a set of data with a slope of -0.5 would show. These points do not represent experimental or numerical data. This generated line lies within the 90% confidence bands.

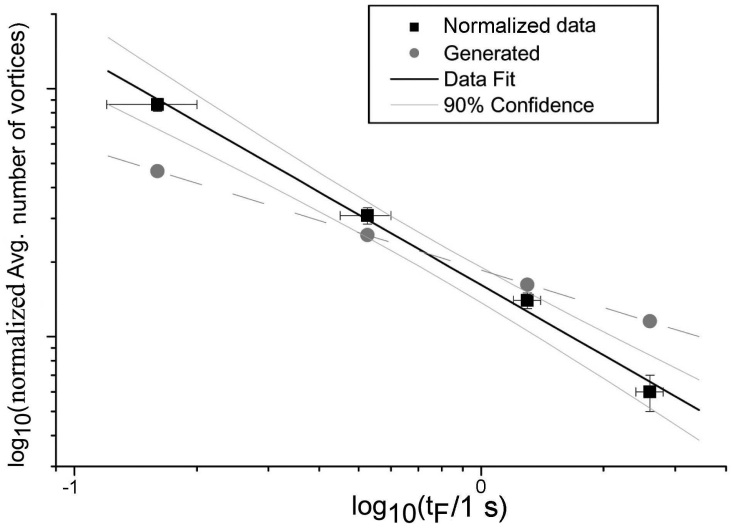

Figure 7.14: Average vortex observations corrected for the differing final BEC sizes is shown, giving a normalized version of Fig. 7.13. A linear regression fit to the data (black squares)was performed in order to compare with [159], giving a slope $-0.94(0.05)$. As in Fig. 7.13, gray circles illustrate a slope of -0.5. The generated -0.5 slope is now clearly outside the 90% confidence bands in this plot.

an additional question is posed by the work of Yates and Zurek [159]. There are two expected slopes: a value of $\gamma = -0.5$ is expected for a so-called *underdamped* case, and $\gamma = -2/3$ for an *overdamped* case, where overdamping and underdamping regimes refer to fast and slow respective rates of vortex annihilation.

There may also be additional effects coming in from the inhomogeneity of the system, which has been shown to affect the defect formation scaling. Qualitatively, in an inhomogeneous system, the gas does not undergo the phase transition uniformly. Instead, a phase front forms, which propagates at a velocity given by [160]:

$$v = v_0 |\epsilon|^{\nu(z-1)}, \tag{7.2}$$

where v_0 is determined by the microphysics of the system, and is equal to ξ_0/τ_0, and $\epsilon = \frac{T_c - T}{T_c}$. In the effectively 1-D system, studied in Ref. [160], the edge of the propagating phase front propagates along one axis, and values for (ν, z) are $(\nu = 2/3, z = 3/2)$ and $(\nu = 1/2, z = 2)$ for a "plausible" and "mean-field" case respectively [160]. The resulting defect density slope is $\gamma \approx -1$, implying proportionality between the quench rate and the defect density. This value corresponds well with the normalized vortex slope seen in Fig. 7.14, further complicating the interpretation of the results. Since we have not obtained enough data to clearly distinguish between the three regimes of overdamping, underdamping, and the inhomogeneous case, a direct comparison of the scaling phenomena seen in the experiment to the Kibble-Zurek model remains elusive. Additionally, uncertainty appears in the experimental estimation of the quench time τ_Q, which was assumed to be equal to t_F, as defined above. More discussion follows in the conclusion of this chapter.

7.5.3 Spontaneous vortex formation in a DC trap

A potential conceptual and systematic concern in a TOP-trap Kibble-Zurek experiment is the presence of a rotating component of the trap. Although the frequency of rotation, at $\omega_{rot} = 2\pi \times 4$ kHz, is large enough such that the cold atoms should only be sensitive to the time average, atomic micromotion scales are sub-micron,

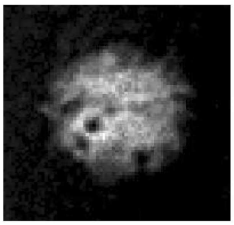

Figure 7.15: Spontaneous vortices resulting from a quench in the DC trap, absorption imaged in expansion.

and micromotion should not lead to turbulence, a check must be made that the signs of the spontaneously generated vortices do not exhibit bias. Quadrupolar surface mode excitation [23] was utilized in the bare-magnetic trap, and no bias was found in the data [79]. However, one might simply utilize the DC optical combined trap (Section 2.6.4), as this trapping configuration contains no rotating component. Condensation in this trap was achieved by implementing a final RF ramp to 1.68 MHz over 6 s with an exponential time constant of $\tau = 1$ s, after transferring a thermal cloud just above condensation into the trap. By expanding and imaging in the normal expansion field, spontaneously generated vortices were observed as shown in Fig. 7.15. These observations served as a check on our spontaneous vortex observations, further ensuring they were not coming from an external rotating influence.

7.6 Conclusions and future directions

In total, the experiments described in this chapter are among the first to study the formation of spontaneous vortices in BEC, and the first to investigate the scaling of vortex formation with quench time. The ability to reproducibly create condensates over a range of formation rates, with approximately an order of magnitude difference between the slowest and fastest formation rates, suggests the possibility of further rigorous experimental comparison to the Kibble-Zurek model. The results summarized in this chapter are consistent with a primary prediction of the Kibble-Zurek model: the vortex observation statistics increase with shorter formation time.

Direct comparison of the defect density power law predicted by the Kibble-Zurek model with the data is more difficult. The apparent difference between Fig. 7.13 and Fig. 7.14, indicates this difficulty. The dramatic difference between the two slopes, coupled with the three different possible slopes given by the Kibble-Zurek model, $\gamma = -1/2$ for the homogenous underdamped case, $\gamma = -2/3$ for the homogenous overdamped case, and $\gamma \approx -1$ for the inhomogeneous case, complicates interpretation of the results.

It seems that the normalized plot (Fig. 7.14) exhibits the best fit, with a slope of $\gamma = -0.94$. However, an overarching difficulty in tallying the vortex observation statistic is the necessary counting of vortices in the images of the cloud, first complicated by the signal-to-noise ratio in the images, and density fluctuations. Additionally, some difficulty may be seen in distinguishing vortices on the edge of the cloud where the density of the cloud, hence the optical depth, is low. In total, these difficulties imply some user dependence in vortex counting numbers and likely underestimation of the error bars in Fig. 7.12, Fig. 7.13, and Fig. 7.14. Also, the decay of vortices with time provides for possible undercounting of vortices, as mentioned above. Further work in the lab will seek to examine these states through interferometric methods, comparing instead correlation length in the system as a function of formation rate, a metric expected to be proportional to the vortex density.

In addition to exploring the fundamental physics of phase-transitions, investigations of the formation of spontaneous vortices in BECs involve the study, at a microscopic level, of the evolution of an out-of-equilibrium initial state predicted to exhibit quantum turbulence. These studies thus form a demonstrated approach for studying the properties and evolution of quantum turbulence in BECs, including the influence of finite temperature on the system. When coupled with numerical simulations, these results, and any additional experimental studies, will continue to shed light on this regime of quantum turbulence.

CHAPTER 8

CONCLUSIONS

The results of the four main experiments discussed in Chapters 4-7 show that BECs represent a particularly convenient system for microscopically studying fundamental aspects of quantum turbulence. This is particularly true due to resolvable vortex cores (after ballistic expansion), the dilute nature of the gas amenable to quantitatively accurate modeling with mean-field theories and finite-temperature environments, and the high level of experimental control over experimental parameters such as trap geometries. Specifically, for studies of turbulence in BECs, it is crucial to understand the formation, dynamics, and decay of quantized vortices. The experiments described in this dissertation represent considerable progress towards building a better microscopic understanding of these aspects of quantized vortices in BECs, and have set the stage for further work. As numerical studies to be undertaken by our collaborators model the experiments described within, and as new experimental and numerical results are obtained, the strengthening of existing connections between experiment and theory will lead to more complete models and powerful tools for future work. This concluding chapter provides a brief review of each of the experiments described in this dissertation, including a discussion of the impact of each experiment, along with discussions of future direction for experimental work.

8.1 Progress towards studies of quantum turbulence

A primary motivation for many of the experiments described within this dissertation were the experiments described in Section 3.4: by harmonically exciting the BEC through modulation of the bias field B_0, or by suddenly adding energy to a BEC, excitations and vortices were seen in the system in both simply and multiply-connected geometries. The apparent ease with which these excitations entered the

system when the atom cloud was held in a toroidal trap was particularly striking. Possible connections to vibrating wire experiments, fluid counterflow experiments, and bubble cavitation experiments in superfluid helium are suggested. Given that quantum turbulence is characterized by the presence of many vortices and their interactions, the presence of many vortices in our BECs suggests the feasibility of an ongoing effort into studying and understanding quantum turbulence in our BECs.

However, macroscopic definitive signatures of a turbulent state were not pursued, and the complete nature of these states, absent an exploration of the energy spectrum in an effort to compare with that expected from the Kolmogorov theory, remains unknown. Nevertheless, the striking appearance of vortex cores in these states fits within the qualitative definition of turbulence given in Section 3.3.3, and initiated our efforts to more completely understand the microscopic behavior of vortices in our system by exploring a variety of simplified and better-controlled vortex configurations.

8.1.1 Vortex dipoles

By examining the fluid flow in the wake of a moving obstacle (a blue-detuned laser beam), relative to the rest frame of the harmonic trap, the generation and dynamics of vortex dipoles were microscopically determined for the first time in BEC experiments. The additional observation of multiply-charged vortex dipoles in both experiments and numerical simulations represent a new set of metastable fluid-flow structures in BEC. The dipoles exhibited defined flow patterns organized into periodic orbits of the vortices, in qualitative analogy with classical dipolar flows.

This experiment afforded us much information regarding the behavior of vortices and antivortices in the system: in particular, (i) the long lifetimes of the vortex dipoles indicated that vortices and antivortices can closely approach each other without annihilation, and (ii) the propensity of like-charge vortices to remain closely spaced about the loci of circulation in the dipolar flow was unexpected. Additionally the generation of vortices through movement of a barrier through the system provides important clues to the behavior seen in the harmonically-excited toroidal

trap.

8.1.2 Persistent currents

Extending our vortex dipole creation techniques into a toroidal, multiply-connected geometry, we were able to selectively nucleate many vortices near a repulsive barrier forming the center of a toroidal potential. With the addition of thermal damping to remove extraneous vortex cores, the initial turbulent state evolved and multiply-charged persistent currents were stochastically created. These superflow structures were long-lived, and were able to be created in both the flattened toroidal potential, created with the addition of the 1090-nm red-detuned light sheet and repulsive central barrier, as well as in a sagged TOP trap combined with a repulsive central barrier. The wide applicability of this technique represents a new paradigm for the creation of persistent currents in harmonically trapped BECs.

The low amplitude of relative beam motion necessary for exciting many vortex cores, in combination with the increased likelihood of seeing extraneous vortices as the atom cloud number decayed and the repulsive potential moved to the side of the BEC provides further information regarding the behavior seen in the harmonically-excited toroidal trap, where vortices were easily generated through harmonic modulation of the trap.

8.1.3 Vortex lattice spin-down

By first introducing angular momentum into the system through production of a vortex lattice, the dynamics of the loss of angular momentum from the BEC system was investigated as a response to impurities introduced into the potential well holding the BEC. Such systematic limits on the lifetime of vortices in the system necessarily alter the dynamics of vortices, and thus are relevant to the study of quantum turbulence in the system. A benefit to using BECs in such studies is the clean and controllable potentials used to confine the gas of atoms. By selectively adding impurities, physics that may be relevant to other superfluid systems may be

microscopically explored.

8.1.4 Spontaneous vortices

The spontaneous vortex formation mechanism is characterized by the evolution of an out-of-equilibrium turbulent state into quasi-equilibrium, characterized by the presence of vortex cores. Expanding on our previous work, representing the first observations of spontaneous vortices in BECs, we were able to modify the BEC formation rate in an effort to compare directly with the Kibble-Zurek model, which predicts a vortex density dependent on the quench rate.

As a key component of the Kibble-Zurek model, the increased density of vortex cores with faster formation rates was confirmed in our system. The quantitative match of the scaling rate with the rate predicted by the Kibble-Zurek model is somewhat less clear, although the results seem to point towards the relevance of an inhomogenous Kibble-Zurek model in our system. There is much room for future work exploring spontaneously formed vortices in BECs as an avenue of understanding phase transition dynamics as well as quantum turbulence.

8.2 Future directions

These research results suggest many different directions for future work. The creation of vortex dipoles can be extended in various ways, in experiments that attempt to pin the resulting vortex and antivortex, with the goal of studying vortex annihilation and dynamics with the added ability to controllably place the vortex pair within the condensate. Details of the resulting orbits of the released dipoles might be explored, and the behavior near the stable points (see Section 4.3.1) might be characterized. Additionally, with the introduction of even more beams, it may be possible to produce more exotic pinned vortex states.

Extending the persistent current work, an experiment might be undertaken that explores the vortex dynamics as the the barrier beam is ramped down. The regular configurations of vortex cores occasionally seen in the experiment (see Section 5.2.3),

are expected from simulations [151], and an experiment to examine these states in more detail would be worthwhile.

There is also much work to be done regarding the formation of spontaneous vortices in the system, as further experiments will hopefully provide for a direct test of the Kibble-Zurek scaling law in this system. Since a primary limitation of the experiment was the ability to reliably distinguish vortex cores, interferometric methods of characterizing the condensate are currently underway, and determining a coherence length as a function of formation time will be soon tested. With enough data, this alternative method of characterizing vortex densities will hopefully be able to distinguish between the various Kibble-Zurek scaling laws, and will also be applicable to studies of quantum turbulence.

As a broad picture of the formation, dynamics, and decay of quantized vortices in our system is established, continued studies of turbulence will be facilitated. Finally, we are confident that experimental and numerical studies of BECs will likely provide further clues to properties of quantum turbulence, as well as further advance a microscopic understanding of quantum turbulence built on firm experimental results and corresponding numerical simulations.

REFERENCES

[1] M. H. Anderson, J. R. Ensher, M. R. Matthews, C. E. Wieman, and E. A. Cornell. Observation of Bose-Einstein Condensation in a Dilute Atomic Vapor. *Science*, 269(5221):198–201, 1995.

[2] K. B. Davis, M. O. Mewes, M. R. Andrews, N. J. van Druten, D. S. Durfee, D. M. Kurn, and W. Ketterle. Bose-Einstein condensation in a gas of sodium atoms. *Phys. Rev. Lett.*, 75(22):3969–3973, Nov 1995.

[3] C. C. Bradley, C. A. Sackett, J. J. Tollett, and R. G. Hulet. Evidence of Bose-Einstein condensation in an atomic gas with attractive interactions. *Phys. Rev. Lett.*, 75(9):1687–1690, Aug 1995.

[4] C. J. Pethick and H. Smith. *Bose-Einstein Condensation in Dilute Gases*. Cambridge University Press, 2002.

[5] L. Pitaevskii and S. Stringari. *Bose-Einstein Condensation*. Oxford University Press, New York, N.Y., 2003.

[6] P. G. Kevrekidis, D. J. Frantzeskakis, and R. Carretero-González, editors. *Emergent Nonlinear Phenomena in Bose-Einstein Condensates*. Springer-Verlag, Berlin Heidelberg, 2008.

[7] P. Meystre. *Atom Optics*. Springer-Verlag, New York, NY, 2001.

[8] D. R. Scherer. *Vortex Formation by Merging and Interference of Multiple Trapped Bose-Einstein Condensates*. Ph.D Thesis, The University of Arizona, 2007.

[9] C. N. Weiler. *Spontaneous Formation of Quantized Vortices in Bose-Einstein Condensates*. Ph.D Thesis, The University of Arizona, 2008.

[10] D. R. Tilley and J. Tilley. *Superfluidity and Superconductivity*. Taylor & Francis, London, 1990.

[11] R. P. Feynman. Application of quantum mechanics to liquid helium. *Progress in Low Temperature Physics*, 1:17–53, 1955.

[12] R. J. Donnelly. *Quantized Vortices in Helium II*. Cambridge University Press, New York, 1991.

[13] C. F. Barenghi, R. J. Donnelly, and W. F. Vinen, editors. *Quantized Vortex Dynamics and Superfluid Turbulence*. Springer-Verlag, Berlin, 2001.

[14] C. Cohen-Tannoudji, B. Diu, and F. Laloë. *Quantum Mechanics*. Herman, Paris, France, 1977.

[15] A. J. Leggett. Bose-Einstein condensation in the alkali gases: Some fundamental concepts. *Rev. Mod. Phys.*, 73(2):307–356, Apr 2001.

[16] A. L. Fetter and A. A. Svidzinsky. Vortices in a trapped dilute Bose-Einstein condensate. *J. Phys. B*, 13(12):R135–R194, Dec 2001.

[17] A. L. Fetter. Vortices in an imperfect Bose gas. I. The condensate. *Phys. Rev.*, 138(2A):A429–A437, Apr 1965.

[18] J. R. Abo-Shaeer, C. Raman, J. M. Vogels, and W. Ketterle. Observation of Vortex Lattices in Bose-Einstein Condensates. *Science*, 292(5516):476–479, 2001.

[19] M. R. Matthews, B. P. Anderson, P. C. Haljan, D. S. Hall, C. E. Wieman, and E. A. Cornell. Vortices in a Bose-Einstein condensate. *Phys. Rev. Lett.*, 83(13):2498, Sep 1999.

[20] A. L. Fetter. Rotating trapped Bose-Einstein condensates. *Rev. Mod. Phys.*, 81(2):647–691, May 2009.

[21] K. W. Madison, F. Chevy, W. Wohlleben, and J. Dalibard. Vortex formation in a stirred Bose-Einstein condensate. *Phys. Rev. Lett.*, 84(5):806, Jan 2000.

[22] K. W. Madison, F. Chevy, W. Wohlleben, and J. Dalibard. Vortices in a stirred Bose-Einstein condensate. *J. Mod. Opt.*, 47(14-15):2715, Nov 2000.

[23] F. Chevy, K. W. Madison, and J. Dalibard. Measurement of the angular momentum of a rotating Bose-Einstein condensate. *Phys. Rev. Lett.*, 85(11):2223, Sep 2000.

[24] B. P. Anderson, P. C. Haljan, C. E. Wieman, and E. A. Cornell. Vortex precession in Bose-Einstein condensates: Observations with filled and empty cores. *Phys. Rev. Lett.*, 85(14):2857, Oct 2000.

[25] J. R. Abo-Shaeer, C. Raman, J. M. Vogels, and W. Ketterle. Observation of vortex lattices in Bose-Einstein condensates. *Science*, 292(5516):476, Apr 2001.

[26] B. P. Anderson, P. C. Haljan, C. A. Regal, D. L. Feder, L. A. Collins, C. W. Clark, and E. A. Cornell. Watching dark solitons decay into vortex rings in a Bose-Einstein condensate. *Phys. Rev. Lett.*, 86(14):2926, Apr 2001.

[27] P. C. Haljan, B. P. Anderson, I. Coddington, and E. A. Cornell. Use of surface-wave spectroscopy to characterize tilt modes of a vortex in a Bose-Einstein condensate. *Phys. Rev. Lett.*, 86(14):2922, Apr 2001.

[28] K. W. Madison, F. Chevy, V. Bretin, and J. Dalibard. Stationary states of a rotating Bose-Einstein condensate: Routes to vortex nucleation. *Phys. Rev. Lett.*, 86(20):4443, May 2001.

[29] Z. Dutton, M. Budde, C. Slowe, and L. V. Hau. Observation of quantum shock waves created with ultra-compressed slow light pulses in a Bose-Einstein condensate. *Science*, 293(5530):663, Jul 2001.

[30] F. Chevy, K. W. Madison, V. Bretin, and J. Dalibard. Interferometric detection of a single vortex in a dilute Bose-Einstein condensate. *Phys. Rev. A*, 64(3):031601, Aug 2001.

[31] S. Inouye, S. Gupta, T. Rosenband, A. P. Chikkatur, A. Görlitz, T. L. Gustavson, A. E. Leanhardt, D. E. Pritchard, and W. Ketterle. Observation of vortex phase singularities in Bose-Einstein condensates. *Phys. Rev. Lett.*, 87(8):080402, Aug 2001.

[32] P. C. Haljan, I. Coddington, P. Engels, and E. A. Cornell. Driving Bose-Einstein-condensate vorticity with a rotating normal cloud. *Phys. Rev. Lett.*, 87(21):210403, Nov 2001.

[33] C. Raman, J. R. Abo-Shaeer, J. M. Vogels, K. Xu, and W. Ketterle. Vortex nucleation in a stirred Bose-Einstein condensate. *Phys. Rev. Lett.*, 87(21):210402, Nov 2001.

[34] E. Hodby, G. Hechenblaikner, S. A. Hopkins, O. M. Maragò, and C. J. Foot. Vortex nucleation in Bose-Einstein condensates in an oblate, purely magnetic potential. *Phys. Rev. Lett.*, 88(1):010405, Dec 2001.

[35] J. R. Abo-Shaeer, C. Raman, and W. Ketterle. Formation and decay of vortex lattices in Bose-Einstein condensates at finite temperatures. *Phys. Rev. Lett.*, 88(7):070409, Feb 2002.

[36] P. Rosenbusch, D. S. Petrov, S. Sinha, F. Chevy, V. Bretin, Y. Castin, G. Shlyapnikov, and J. Dalibard. Critical rotation of a harmonically trapped Bose gas. *Phys. Rev. Lett.*, 88(25):250403, Jun 2002.

[37] P. Engels, I. Coddington, P. C. Haljan, and E. A. Cornell. Nonequilibrium effects of anisotropic compression applied to vortex lattices in Bose-Einstein condensates. *Phys. Rev. Lett.*, 89(10):100403, Aug 2002.

[38] A. E. Leanhardt, A. Görlitz, A. P. Chikkatur, D. Kielpinski, Y. Shin, D. E. Pritchard, and W. Ketterle. Imprinting vortices in a Bose-Einstein condensate using topological phases. *Phys. Rev. Lett.*, 89(19):190403, Oct 2002.

[39] P. Rosenbusch, V. Bretin, and J. Dalibard. Dynamics of a single vortex line in a Bose-Einstein condensate. *Phys. Rev. Lett.*, 89(20):200403, Oct 2002.

[40] V. Bretin, P. Rosenbusch, F. Chevy, G. V. Shlyapnikov, and J. Dalibard. Quadrupole oscillation of a single-vortex Bose-Einstein condensate: Evidence for Kelvin modes. *Phys. Rev. Lett.*, 90(10):100403, Mar 2003.

[41] V. Bretin, P. Rosenbusch, and J. Dalibard. Dynamics of a single vortex line in a Bose-Einstein condensate. *Journal of Optics B: Quantum and Semiclassical Optics*, 5(2):S23, Apr 2003.

[42] A. E. Leanhardt, Y. Shin, D. Kielpinski, D. E. Pritchard, and W. Ketterle. Coreless vortex formation in a spinor Bose-Einstein condensate. *Phys. Rev. Lett.*, 90(14):140403, Apr 2003.

[43] P. Engels, I. Coddington, P. C. Haljan, V. Schweikhard, and E. A. Cornell. Observation of long-lived vortex aggregates in rapidly rotating Bose-Einstein condensates. *Phys. Rev. Lett.*, 90(17):170405, May 2003.

[44] P. Engels, I. Coddington, P. C. Haljan, and E. A. Cornell. Using anisotropic compression to melt a vortex lattice in a Bose-Einstein condensate. *Physica B: Cond. Mat.*, 329(1):7, May 2003.

[45] E. Hodby, S. A. Hopkins, G. Hechenblaikner, N. L. Smith, and C. J. Foot. Experimental observation of a superfluid gyroscope in a dilute Bose-Einstein condensate. *Phys. Rev. Lett.*, 91(9):090403, Aug 2003.

[46] I. Coddington, P. Engels, V. Schweikhard, and E. A. Cornell. Observation of Tkachenko oscillations in rapidly rotating Bose-Einstein condensates. *Phys. Rev. Lett.*, 91(10):100402, Sep 2003.

[47] P. Engels, I. Coddington, V. Schweikhard, and E. A. Cornell. Vortex lattice dynamics in a dilute gas BEC. *J. Low Temp. Phys*, 134:683, Jan 2004.

[48] V. Schweikhard, I. Coddington, P. Engels, V. P. Mogendorff, and E. A. Cornell. Rapidly rotating Bose-Einstein condensates in and near the lowest Landau level. *Phys. Rev. Lett.*, 92(4):040404, Jan 2004.

[49] V. Bretin, S. Stock, Y. Seurin, and J. Dalibard. Fast rotation of a Bose-Einstein condensate. *Phys. Rev. Lett.*, 92(5):050403, Feb 2004.

[50] S. Stock, V. Bretin, F. Chevy, and J. Dalibard. Shape oscillation of a rotating Bose-Einstein condensate. *Europhys. Lett.*, 65(5):594, Mar 2004.

[51] P. Rosenbusch, V. Bretin, F. Chevy, G. V. Shlyapnikov, and J. Dalibard. Evidence for Kelvin modes in a single vortex Bose-Einstein condensate. *Laser Phys.*, 14(4):545, 2004.

[52] N. L. Smith, W. H. Heathcote, J. M. Krueger, and C. J. Foot. Experimental observation of the tilting mode of an array of vortices in a dilute Bose-Einstein condensate. *Phys. Rev. Lett.*, 93(8):080406, Aug 2004.

[53] Y. Shin, M. Saba, M. Vengalattore, T. A. Pasquini, C. Sanner, A. E. Leanhardt, M. Prentiss, D. E. Pritchard, and W. Ketterle. Dynamical instability of a doubly quantized vortex in a Bose-Einstein condensate. *Phys. Rev. Lett.*, 93(16):160406, Oct 2004.

[54] V. Schweikhard, I. Coddington, P. Engels, S. Tung, and E. A. Cornell. Vortex-lattice dynamics in rotating spinor Bose-Einstein condensates. *Phys. Rev. Lett.*, 93(21):210403, Nov 2004.

[55] I. Coddington, P. C. Haljan, P. Engels, V. Schweikhard, S. Tung, and E. A. Cornell. Experimental studies of equilibrium vortex properties in a Bose-condensed gas. *Phys. Rev. A*, 70(6):063607, Dec 2004.

[56] N. S. Ginsberg, J. Brand, and L. V. Hau. Observation of hybrid soliton vortex-ring structures in Bose-Einstein condensates. *Phys. Rev. Lett.*, 94(4):040403, Jan 2005.

[57] S. Stock, B. Battelier, V. Bretin, Z. Hadzibabic, and J. Dalibard. Bose-Einstein condensates in fast rotation. *Laser Phys. Lett.*, 2(6):275, Jan 2005.

[58] T. P. Simula, P. Engels, I. Coddington, V. Schweikhard, E. A. Cornell, and R. J. Ballagh. Observations on sound propagation in rapidly rotating Bose-Einstein condensates. *Phys. Rev. Lett.*, 94(8):080404, Mar 2005.

[59] M. W. Zwierlein, J. R. Abo-Shaeer, A. Schirotzek, C. H. Schunck, and W. Ketterle. Vortices and superfluidity in a strongly interacting Fermi gas. *Nature*, 435(7045):1047, Jun 2005.

[60] S . Stock, Z. Hadzibabic, B. Battelier, M. Cheneau, and J. Dalibard. Observation of phase defects in quasi-two-dimensional Bose-Einstein condensates. *Phys. Rev. Lett.*, 95(19):190403, Nov 2005.

[61] M. W. Zwierlein, A. Schirotzek, C. H. Schunck, and W. Ketterle. Fermionic superfluidity with imbalanced spin populations. *Science*, 311(5760):492, Jan 2006.

[62] M. Kumakura, T. Hirotani, M. Okano, T. Yabuzaki, and Y. Takahashi. Topological creation of a multiply charged quantized vortex in the Rb Bose-Einstein condensate. *Laser Phys.*, 16(2):371, Feb 2006.

[63] S. R. Muniz, D. S. Naik, and C. Raman. Bragg spectroscopy of vortex lattices in Bose-Einstein condensates. *Phys. Rev. A*, 73(4):041605, Apr 2006.

[64] Z. Hadzibabic, P. Kruger, M. Cheneau, B. Battelier, and J. Dalibard. Berezinskii-Kosterlitz-Thouless crossover in a trapped atomic gas. *Nature*, 441(7097):1118, Jun 2006.

[65] M. Kumakura, T. Hirotani, M. Okano, Y. Takahashi, and T. Yabuzaki. Topological formation of a multiply charged vortex in the Rb Bose-Einstein condensate: Effectiveness of the gravity compensation. *Phys. Rev. A*, 73(6):063605, Jun 2006.

[66] L. E. Sadler, J. M. Higbie, S. R. Leslie, M. Vengalattore, and D. M. Stamper-Kurn. Spontaneous symmetry breaking in a quenched ferromagnetic spinor Bose-Einstein condensate. *Nature*, 443(7109):312, Sep 2006.

[67] M. F. Andersen, C. Ryu, P. Cladé, V. Natarajan, A. Vaziri, K. Helmerson, and W. D. Phillips. Quantized rotation of atoms from photons with orbital angular momentum. *Phys. Rev. Lett.*, 97(17):170406, Oct 2006.

[68] S. Tung, V. Schweikhard, and E. A. Cornell. Observation of vortex pinning in Bose-Einstein condensates. *Phys. Rev. Lett.*, 97(24):240402, Dec 2006.

[69] C. H. Schunck, M. W. Zwierlein, A. Schirotzek, and W. Ketterle. Superfluid expansion of a rotating Fermi gas. *Phys. Rev. Lett.*, 98(5):050404, Feb 2007.

[70] S. R. Muniz, D. S. Naik, M. Bhattacharya, and C. Raman. Dynamics of rotating Bose-Einstein condensates probed by Bragg scattering. *Mathematics and Computers in Simulation*, 74(4-5):397, Mar 2007.

[71] D. R. Scherer, C. N. Weiler, T. W. Neely, and B. P. Anderson. Vortex formation by merging of multiple trapped Bose-Einstein condensates. *Phys. Rev. Lett.*, 98(11):110402, Mar 2007.

[72] K. Helmerson, M. F. Andersen, C. Ryu, P. Cladé, V. Natarajan, A. Vaziri, and W.D. Phillips. Generating persistent currents states of atoms using orbital angular momentum of photons. *Nuclear Physics A*, 790(1-4):705c, Jun 2007.

[73] V. Schweikhard, S. Tung, and E. A. Cornell. Vortex proliferation in the Berezinskii-Kosterlitz-Thouless regime on a two-dimensional lattice of Bose-Einstein condensates. *Phys. Rev. Lett.*, 99(3):030401, Jul 2007.

[74] T. Isoshima, M. Okano, H. Yasuda, K. Kasa, J. A. M. Huhtamäki, M. Kumakura, and Y. Takahashi. Spontaneous splitting of a quadruply charged vortex. *Phys. Rev. Lett.*, 99(20):200403, Nov 2007.

[75] C. Ryu, M. F. Andersen, P. Cladé, V. Natarajan, K. Helmerson, and W. D. Phillips. Observation of persistent flow of a Bose-Einstein condensate in a toroidal trap. *Phys. Rev. Lett.*, 99(26):260401, Dec 2007.

[76] Z. Hadzibabic, P. Kruger, M. Cheneau, S. P. Rath, and J. Dalibard. The trapped two-dimensional Bose gas: from Bose-Einstein condensation to Berezinskii-Kosterlitz-Thouless physics. *New Journal of Physics*, 10(4):045006, Apr 2008.

[77] K. C. Wright, L. S. Leslie, and N. P. Bigelow. Optical control of the internal and external angular momentum of a Bose-Einstein condensate. *Phys. Rev. A*, 77(4):041601, Apr 2008.

[78] D. McKay, M. White, M. Pasienski, and B. DeMarco. Phase-slip-induced dissipation in an atomic Bose-Hubbard system. *Nature*, 453(7191):76, May 2008.

[79] C. N. Weiler, T. W. Neely, D. R. Scherer, A. S. Bradley, M. J. Davis, and B. P. Anderson. Spontaneous vortices in the formation of Bose-Einstein condensates. *Nature*, 455(7215):948, Oct 2008.

[80] K. C. Wright, L. S. Leslie, A. Hansen, and N. P. Bigelow. Sculpting the vortex state of a spinor BEC. *Phys. Rev. Lett.*, 102(3):030405, Jan 2009.

[81] E. A. L. Henn, J. A. Seman, E. R. F. Ramos, M. Caracanhas, P. Castilho, E. P. Olímpio, G. Roati, D. V. Magalhães, K. M. F. Magalhães, and V. S. Bagnato. Observation of vortex formation in an oscillating trapped Bose-Einstein condensate. *Phys. Rev. A*, 79(4):043618, Apr 2009.

[82] E. A. L. Henn, J. A. Seman, G. Roati, K. M. F. Magalhães, and V. S. Bagnato. Emergence of turbulence in an oscillating Bose-Einstein condensate. *Phys. Rev. Lett.*, 103(4):045301, Jul 2009.

[83] Y.-J. Lin, R. L. Compton, K. Jimenez-Garcia, J. V. Porto, and I. B. Spielman. Synthetic magnetic fields for ultracold neutral atoms. *Nature*, 462(7273):628, Dec 2009.

[84] K. Helmerson, M. F. Andersen, P. Cladé, V. Natarajan, W. D. Phillips, A. Ramanathan, C. Ryu, and A. Vaziri. Vortices and persistent currents: Rotating a Bose-Einstein condensate using photons with orbital angular momentum. *Topologica*, 2(1):002, 2009.

[85] E. Henn, J. Seman, G. Roati, K. Magalhães, and V. Bagnato. Generation of vortices and observation of quantum turbulence in an oscillating Bose-Einstein condensate. *J. Low Temp. Phys.*, 158(3):435, Feb 2010.

[86] R. A. Williams, S. Al-Assam, and C. J. Foot. Observation of vortex nucleation in a rotating two-dimensional lattice of Bose-Einstein condensates. *Phys. Rev. Lett.*, 104(5):050404, Feb 2010.

[87] T. W. Neely, E. C. Samson, A. S. Bradley, M. J. Davis, and B. P. Anderson. Observation of vortex dipoles in an oblate Bose-Einstein condensate. *Phys. Rev. Lett.*, 104(16):160401, Apr 2010.

[88] C. Cohen-Tannoudji and W. Phillips. New mechanisms for laser cooling. *Physics Today*, 43(10):33–40, 1990.

[89] C. Foot. Laser cooling and trapping of atoms. *Contemp. Phys.*, 32, 1991.

[90] H. Metcalf and P. Van der Straten. *Laser Cooling and Trapping*. Springer, 1999.

[91] E. L. Raab, M. Prentiss, A. Cable, S. Chu, and D. E. Pritchard. Trapping of neutral sodium atoms with radiation pressure. *Phys. Rev. Lett.*, 59(23):2631–2634, Dec 1987.

[92] W. Petrich, M. H. Anderson, J. R. Ensher, and E. A. Cornell. Behavior of atoms in a compressed magneto-optical trap. *J. Opt. Soc. Am. B*, 11(8):1332–1335, 1994.

[93] J. R. Ensher. *The First Experiments with Bose-Einstein Condensates of* ^{87}*Rb*. Ph.D Thesis, The University of Colorado, 1999.

[94] V. Bagnato and D. Kleppner. Bose-Einstein condensation in low-dimensional traps. *Phys. Rev. A*, 44(11):7439–7441, Dec 1991.

[95] A. Görlitz, J. M. Vogels, A. E. Leanhardt, C. Raman, T. L. Gustavson, J. R. Abo-Shaeer, A. P. Chikkatur, S. Gupta, S. Inouye, T. Rosenband, and W. Ketterle. Realization of Bose-Einstein condensates in lower dimensions. *Phys. Rev. Lett.*, 87(13):130402, Sep 2001.

[96] A. L. Migdall, J. V. Prodan, W. D. Phillips, T. H. Bergeman, and H. J. Metcalf. First observation of magnetically trapped neutral atoms. *Phys. Rev. Lett.*, 54(24):2596–2599, Jun 1985.

[97] A. Tsinober. *An Informal Introduction to Turbulence*. Springer, Amsterdam, Netherlands, 2004.

[98] M. Tsubota. Quantum turbulence. *J. Phys. Soc. Japan*, 77(11), Nov 2008.

[99] U. Frisch. *Turbulence: The Legacy of A. N. Kolmogorov*. Cambridge University Press, New York, NY, 1995.

[100] L. Da Vinci. The Notebooks of Leonardo Da Vinci, Complete. ebook, http://www.gutenberg.org/etext/5000, 2004.

[101] C. M. Rhie and W. L. Chow. Numerical study of the turbulent flow past an airfoil with trailing edge separation. *AIAA Journal*, 21:1525–1532, Nov 1983.

[102] W. F. Vinen. An introduction to quantum turbulence. *J. Low Temp. Phys.*, 145:7–24(18), 2006.

[103] M. Kobayashi and M. Tsubota. Quantum turbulence in a trapped Bose-Einstein condensate. *Phys. Rev. A*, 76(4):045603, Oct 2007.

[104] A. J. Chorin. *Vorticity and Turbulence*. Springer-Verlag, New York, NY, 1994.

[105] A. Kolmogorov. The local structure of turbulence in incompressible viscous fluid for very large Reynolds' numbers. *Akademiia Nauk SSSR Doklady*, 30:301–305, 1941.

[106] A. Tsinober. *Quantized Vortex Dynamics and Superfluid Turbulence*. Springer, Berlin, Germany, 2001.

[107] K. W. Schwarz. Three-dimensional vortex dynamics in superfluid ^{4}He: Line-line and line-boundary interactions. *Phys. Rev. B*, 31(9):5782–5804, 1985.

[108] K. W. Schwarz. Three-dimensional vortex dynamics in superfluid ^{4}He: Homogeneous superfluid turbulence. *Phys. Rev. B*, 38(4):2398–2417, 1988.

[109] W. F. Vinen and J. J. Niemela. Quantum turbulence. *J. Low Temp. Phys.*, 128(5-6):167–231, 2002.

[110] T. Araki, M. Tsubota, and S. K. Nemirovskii. Energy spectrum of superfluid turbulence with no normal-fluid component. *Phys. Rev. Lett.*, 89(14):145301, Sep 2002.

[111] J. Maurer and P. Tabeling. Local investigation of superfluid turbulence. *Europhys. Lett.*, 43(1):29–34, 1998.

[112] S. R. Stalp, J. J. Niemela, W. F. Vinen, and R. J. Donnelly. Dissipation of grid turbulence in Helium II. *Physics of Fluids*, 14(4):1377–1379, 2002.

[113] B. V. Svistunov. Superfluid turbulence in the low-temperature limit. *Phys. Rev. B*, 52(5):3647–3653, Aug 1995.

[114] M. R. Smith, R. J. Donnelly, N. Goldenfeld, and W. F. Vinen. Decay of vorticity in homogeneous turbulence. *Phys. Rev. Lett.*, 71(16):2583–2586, Oct 1993.

[115] J. Jäger, B. Schuderer, and W. Schoepe. Turbulent and laminar drag of superfluid helium on an oscillating microsphere. *Phys. Rev. Lett.*, 74(4):566–569, Jan 1995.

[116] S. N. Fisher, A. J. Hale, A. M. Guénault, and G. R. Pickett. Generation and detection of quantum turbulence in superfluid ^{3}He-B. *Phys. Rev. Lett.*, 86(2):244–247, Jan 2001.

[117] H. A. Nichol, L. Skrbek, P. C. Hendry, and P. V. E. McClintock. Flow of He II due to an oscillating grid in the low-temperature limit. *Phys. Rev. Lett.*, 92(24):244501, Jun 2004.

[118] N. Hashimoto, R. Goto, H. Yano, K. Obara, O. Ishikawa, and T. Hata. Control of turbulence in boundary layers of superfluid ^{4}He by filtering out remanent vortices. *Phys. Rev. B*, 76(2):020504, 2007.

[119] R. Hänninen, M. Tsubota, and W. F. Vinen. Generation of turbulence by oscillating structures in superfluid helium at very low temperatures. *Phys. Rev. B*, 75(6):064502, 2007.

[120] N. G. Parker and C. S. Adams. Emergence and decay of turbulence in stirred atomic Bose-Einstein condensates. *Phys. Rev. Lett.*, 95(14):145301, Sep 2005.

[121] B. V. Svistunov. Highly nonequilibrium Bose condensation in a weakly interacting gas. *J. Mosc. Phys. Soc.*, 1:373, 1991.

[122] N. G. Berloff and C. F. Barenghi. Vortex nucleation by collapsing bubbles in Bose-Einstein condensates. *Phys. Rev. Lett.*, 93(9):090401, Aug 2004.

[123] J. Paret and P. Tabeling. Experimental observation of the two-dimensional inverse energy cascade. *Phys. Rev. Lett.*, 79(21):4162–4165, Nov 1997.

[124] S. I. Voropayev and Y. D. Afanasyev. *Vortex Structures in a Stratified Fluid.* Chapman and Hall, London, 1994.

[125] A.I. Ginzburg and K.N. Fedorov. The evolution of a mushroom formed current in the ocean. *Dokl. Akad. Nauk SSSR*, 274:481, 1984.

[126] Y. Couder and C. Basdevant. Experimental and numerical study of vortex couples in two-dimensional flows. *J. Fluid Mech.*, 173:225, 1986.

[127] W. H. Zurek. Cosmological experiments in superfluid helium? *Nature*, 317:505, 1985.

[128] J. R. Anglin and W. H. Zurek. Vortices in the wake of rapid Bose-Einstein condensation. *Phys. Rev. Lett.*, 83(9):1707–1710, Aug 1999.

[129] P. G. Kevrekidis, R. Carretero-Gonzáles, D. J. Frantzeskakis, and I. G. Kevrekidis. Vortices in Bose-Einstein condensates: some recent developments. *Mod. Phys. Lett. B*, 18:1481, 2004.

[130] T. Frisch, Y. Pomeau, and S. Rica. Transition to dissipation in a model of a superflow. *Phys. Rev. Lett.*, 69(11):1644–1647, Dec 1992.

[131] T. Winiecki, J. F. McCann, and C. S. Adams. Pressure drag in linear and nonlinear quantum fluids. *Phys. Rev. Lett.*, 82(26):5186–5189, Dec 1999.

[132] B. Jackson, J. F. McCann, and C. S. Adams. Vortex formation in dilute inhomogeneous Bose-Einstein condensates. *Phys. Rev. Lett.*, 80(18):3903–3906, 1998.

[133] T. Winiecki, B. Jackson, J. F. McCann, and C. S. Adams. Vortex shedding and drag in dilute Bose-Einstein condensates. *J. Phys. B*, 33(19):4069–4078, 2000.

[134] C. Raman, M. Kohl, R. Onofrio, D. S. Durfee, C. E. Kuklewicz, Z. Hadzibabic, and W. Ketterle. Evidence for a critical velocity in a Bose-Einstein condensed gas. *Phys. Rev. Lett.*, 83(13):2502–2505, Dec 1999.

[135] R. Onofrio, C. Raman, J. M. Vogels, J. R. Abo-Shaeer, A. P. Chikkatur, and W. Ketterle. Observation of superfluid flow in a Bose-Einstein condensed gas. *Phys. Rev. Lett.*, 85(11):2228–2231, Dec 2000.

[136] B. Jackson, J. F. McCann, and C. S. Adams. Vortex line and ring dynamics in trapped Bose-Einstein condensates. *Phys. Rev. A*, 61(1):013604, Jan 2000.

[137] M. Crescimanno, C. G. Koay, R. Peterson, and R. Walsworth. Analytical estimate of the critical velocity for vortex pair creation in trapped Bose condensates. *Phys. Rev. A*, 62(6):063612, 2000.

[138] L. C. Crasovan, V. Vekslerchik, V. M. Perez-Garcia, J. P. Torres, D. Mihalache, and L. Torner. Stable vortex dipoles in nonrotating Bose-Einstein condensates. *Phys. Rev. A*, 68(6):063609, Jan 2003.

[139] M. Möttönen, S. M. M. Virtanen, T. Isoshima, and M. M. Salomaa. Stationary vortex clusters in nonrotating Bose-Einstein condensates. *Phys. Rev. A*, 71(3):033626, Jan 2005.

[140] W. Li, M. Haque, and S. Komineas. Vortex dipole in a trapped two-dimensional Bose-Einstein condensate. *Phys. Rev. A*, 77(5):053610, Jan 2008.

[141] E. Lundh and P. Ao. Hydrodynamic approach to vortex lifetimes in trapped Bose condensates. *Phys. Rev. A*, 61(6):063612, Jan 2000.

[142] A. J. Leggett. Superfluidity. *Rev. Mod. Phys.*, 71(2):S318–S323, 1999.

[143] F. Bloch. Superfluidity in a ring. *Phys. Rev. A*, 7(6):2187–2191, Jun 1973.

[144] D. Mailly, C. Chapelier, and A. Benoit. Experimental observation of persistent currents in GaAs-AlGaAs single loop. *Phys. Rev. Lett.*, 70(13):2020–2023, Mar 1993.

[145] J. D. Reppy and D. Depatie. Persistent currents in superfluid helium. *Phys. Rev. Lett.*, 12(8):187–189, Feb 1964.

[146] J. P. Pekola, J. T. Simola, K. K. Nummila, O. V. Lounasmaa, and R. E. Packard. Persistent-current experiments on superfluid ^{3}He-B and ^{3}He-A. *Phys. Rev. Lett.*, 53(1):70–73, Jul 1984.

[147] D. A. Butts and D. S. Rokhsar. Predicted signatures of rotating Bose-Einstein condensates. *Nature*, 397:327–329, 1999.

[148] M. Tsubota, K. Kasamatsu, and M. Ueda. Vortex lattice formation in a rotating Bose-Einstein condensate. *Phys. Rev. A*, 65(2):023603, Jan 2002.

[149] E. Lundh, C. J. Pethick, and H. Smith. Vortices in Bose-Einstein-condensed atomic clouds. *Phys. Rev. A*, 58(6):4816–4823, Dec 1998.

[150] T. P. Simula, S. M. M. Virtanen, and M. M. Salomaa. Stability of multiquantum vortices in dilute Bose-Einstein condensates. *Phys. Rev. A*, 65(3):033614, Feb 2002.

[151] P. Capuzzi and D. M. Jezek. Stationary arrays of vortices in Bose-Einstein condensates confined by a toroidal trap. *J. Phys. B*, 42(14):145301 (7pp), 2009.

[152] C. F. Barenghi, R. J. Donnelly, and W. F. Vinen. Friction on quantized vortices in Helium II. A review. *J. Low Temp. Phys.*, 52:189–247, August 1983.

[153] R. Carretero-González, B. P. Anderson, P. G. Kevrekidis, D. J. Frantzeskakis, and C. N. Weiler. Dynamics of vortex formation in merging Bose-Einstein condensate fragments. *Phys. Rev. A*, 77(3):033625, March 2008.

[154] P. C. Haljan, I. Coddington, P. Engels, and E. A. Cornell. Driving Bose-Einstein condensate vorticity with a rotating normal cloud. *Phys. Rev. Lett.*, 87(21):210403, Nov 2001.

[155] Y. P. Chen, J. Hitchcock, D. Dries, M. Junker, C. Welford, and R. G. Hulet. Phase coherence and superfluid-insulator transition in a disordered Bose-Einstein condensate. *Phys. Rev. A*, 77(3):033632, 2008.

[156] B. Svistunov. Strongly non-equilibrium Bose-Einstein condensation in a trapped gas. *Phys. Lett. A*, 287(1-2):169–174, 2001.

[157] N. G. Berloff and B. V. Svistunov. Scenario of strongly nonequilibrated Bose-Einstein condensation. *Phys. Rev. A*, 66(1):013603, Jul 2002.

[158] T. W. B. Kibble. Topology of cosmic domains and strings. *J. Phys. A*, 9, 1976.

[159] A. Yates and W. H. Zurek. Vortex formation in two dimensions: When symmetry breaks, how big are the pieces? *Phys. Rev. Lett.*, 80(25):5477–5480, Jun 1998.

[160] W. H. Zurek. Causality in condensates: Gray solitons as relics of BEC formation. *Phys. Rev. Lett.*, 102(10):105702, Mar 2009.

[161] W. H. Zurek. Cosmological experiments in condensed matter systems. *Phys. Rep.*, 276:177–221, November 1996.

[162] M. V. Berry. The adiabatic phase and Pancharatnam's phase for polarized light. *J. Mod. Opt.*, 34:1401–1407, nov 1987.